DESIGN, FABRICATION, AND TESTING OF AN EMR GUN BASED ORBITAL DEBRIS IMPACT TESTING PLATFORM

A Thesis
presented to
the Faculty of California Polytechnic State University,
San Luis Obispo

In Partial Fulfillment
of the Requirements for the Degree
Master of Science in Aerospace Engineering

by
Jeffrey Joseph Maniglia Jr.
June 2013

COMMITTEE MEMBERSHIP

TITLE:	Design, Fabrication, And Testing Of An EMR Gun Based Orbital Debris Impact Testing Platform
AUTHOR:	Jeffrey Joseph Maniglia Jr.
DATE SUBMITTED:	June 2013
COMMITTEE CHAIR:	Kira Abercromby, Professor of Aeronautics, California Polytechnic State University
COMMITTEE MEMBER:	William Maier, Professor of Electrical Engineering, Naval Postgraduate School
COMMITTEE MEMBER:	Eric Mehiel, Professor of Aeronautics, California Polytechnic State University
COMMITTEE MEMBER:	Vladimir Prodanov, Professor of Electrical Engineering, California Polytechnic State University

ABSTRACT

DESIGN, FABRICATION, AND TESTING OF AN EMR GUN BASED ORBITAL DEBRIS IMPACT TESTING PLATFORM

Jeffrey Joseph Maniglia Jr.

This paper describes the changes made from Cal Poly's initial railgun system, the Mk. 1 railgun, to the Mk. 1.1 system, as well as the design, fabrication, and testing of a newer and larger Mk. 2 railgun system. The Mk. 1.1 system is developed as a more efficient alteration of the original Mk. 1 system, but is found to be defective due to hardware deficiencies and failure, as well as unforeseen efficiency losses. A Mk. 2 system is developed and built around donated hardware from the Naval Postgraduate School. The Mk. 2 system strove to implement an efficient, augmented, electromagnetic railgun and projectile system capable of firing an approximate 1g aluminum projectile to speeds exceeding 2 km/s. A novel three part projectile is proposed to mitigate rail and projectile degradation. Projectile and sabot system kinematic equations are derived and the projectile is designed and tested along with Mk. 2 barrel. A numerical electromechanical model is developed to predict the performance of the Mk. 2 system and projectile assembly, and predicts a final velocity for the fabricated system exceeding 3.5 km/s and an efficiency as high as 24%. Testing of the Mk. 2 system showed catastrophic failure of the projectile during initial acceleration, resulting in very short acceleration times and distance, low velocity projectiles, and low efficiencies. During further testing of various projectile configurations, the barrel structure failed due to a large internal arc. Future work for the Mk. 2 system is discussed, a revised external barrel structure suggested, and a solid, more conventional solid chevron projectile design suggested.

Keywords: Electromagnetic, railgun, magnetic, hypersonic, orbital, debris, Cal Poly, rail, gun, augmentation, model, testing

ACKNOWLEDGMENTS

First and foremost, I would like to thank my amazing wife, Alisha, for all of her patience and support during the time of this research. This would not have been possible without her by my side. I would also like to thank Dr. Jeffrey Puschell and Raytheon, the Jet Propulsion Laboratory, Lockheed Martin, and Northrup Grumman for their financial support of this project. I thank my Thesis Advisor, Dr. Kira Abercromby, for coming on this journey and believing in this project for the past three years, and for all her help and guidance. I would also like to thank Dr. Bill Maier and the Naval Postgraduate School for their hardware donations, worth easily over $100k, and for all of their research into railgun technology that made this project possible. I would like to thank Aleksey Pavlov for working alongside me during the Mk. 1.1 testing. I would also like to thank Dr. Bill Maier for his insight and help, and for the design concept of the three part projectile tested in this thesis.

This project was not only an intellectual challenge, but also required circuit design and fabrication, hardware fabrication, system testing, etc. I would like to thank those that helped me greatly with these facets of the project, including Cody Thompson, Nolan Uchizono, Ladd Caine, David Sherman, Dr. Vladimir Prodanov, and Daniel Wait.

Furthermore, I would like to thank Dr. John Chen and the Mechanical Engineering Department at California Polytechnic State University for the repeated use of their Phantom High Speed Camera.

TABLE OF CONTENTS

LIST OF TABLES

LIST OF FIGURES

1 Introduction

With the increased use of our Earth orbits by government, commercial, and even university small-sats, the need for protection and continued research into orbital debris impacts is growing daily. Some of this debris can be tracked; specifically particles larger than 5cm in diameter in LEO, and 1m in GEO, are tracked and recorded by ground based radar systems. Current shielding technology is most effective in stopping particles less than 1cm in diameter. This leaves the range from 1cm to 5cm, in LEO orbits regimes, and 1cm to 1m in GEO orbital regimes completely invisible and the satellites unprotected. In order to simulate these hypervelocity impacts that are becoming more and more common place aboard spacecraft, accelerating a 1cm to 5cm diameter particle to several km/s is required. [1]

Currently there are systems that test hypervelocity impacts. Such systems include NASA's Light Gas Gun, Texas A&M's plasma railgun, and NASA's Inhibited Shaped Charge Launcher. All of these guns are capable of launch velocities on the order of 7-11km/s impact velocity, but lack one important aspect that this thesis is trying to test: the mass of a 1cm to 5cm particle travelling at orbital velocity. These systems all have tested in much smaller particle sizes, and have brought shielding technology to the point that it is today. To increase particle size, more energy needs to be transmitted to a much larger projectile.

Electromagnetic launchers, commonly called railguns, have a long history dating back to as early as 1901 when it was patented by Birkeland as a "Patent Electric Gun". During World War I and World War II there was significant research done on railguns by both the Germans and the Japanese [2]. The Germans built the first functional railgun in 1944, and shortly thereafter commissioned a specification for a battalion from Luftwaffe's Flak Command for railguns with muzzle velocities of 2 km/s, with the projectile containing as much as 500 grams of explosive material. The battalion was never built. [3]

More recently, the United States military, specifically the Navy, have been testing railguns as a ship based long range kinetic energy weapon. The latest released test was done by the General Atomics Blitzer railgun prototype in February 2012, with a muzzle energy approaching 33 MJ, and speeds most likely exceeding 2000 m/s, though these values are estimations as the real values have yet to be released. These systems utilize capacitive energy storage for their high pulse current output and safe storage as compared to other energy storage solutions, such as mechanical and chemical.

This thesis applies the same theory and research done for the large naval railgun weapon systems into a smaller package, continues the work done at Cal Poly on the Mk. 1 railgun [4], and hopes to increase efficiency and performance to a point where hypersonic impact testing can be completed. Hypersonic speeds are defined as speeds exceeding Mach 5, and for this paper analysis is assuming sea-level atmospheric pressure. At sea level, Mach 5 is the equivalent of 1701.45 m/s.

1.1 Railgun General Principle

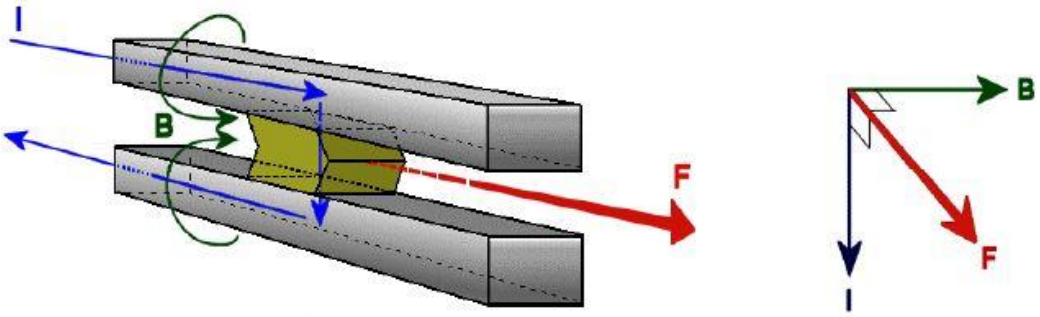

Figure 1 - Visual Representation of Lorentz Force [13]

Railguns operate on a single, well known, law of electromagnetics called the Lorentz Force. The Lorentz Force is determined by the following equation [2]

$$\vec{F} = q\vec{v}_d x\vec{B}$$ **Equation 1**

where $\vec{F}$ is the force, in Newtons, on the current-carrying wire, q is charge in Coulombs, $\vec{v}_d$ is the electron drift velocity in m/s, and $\vec{B}$ is the magnetic field vector in Tesla. Since the following is true,

$$q = I * t = I\left(\frac{l}{v_d}\right)$$ **Equation 2**

where l is the distance between the rails and I is the magnitude of the current, therefore the electron drift velocity drops out of the equation, and we are left with

$$F = lIB$$ **Equation 3**

where F is the magnitude of the Lorentz Force and B is the magnitude of the magnetic field. Equation 3 assumes that the current and magnetic field vectors are at 90° relative to one another, which is common in railgun geometries.

2 Mk. 1.1: The step from injection to press-fit

The Mk. 1.1 system altered the Mk. 1 capacitor bank as well as the Mk. 1 barrel in an attempt to improve the efficiency and final velocity of the Mk. 1 system. To fully understand modifications and implications of the Mk. 1.1 system the Mk. 1 system must be understood.

2.1 Brief Mk. 1 History

The work that precedes this thesis was called the Cal Poly Mk. 1 Railgun [4]. The goal of the Mk. 1 system was to demonstrate the capabilities of a railgun on a small scale, and to work up to a much larger system capable of the speeds needed to test orbital debris impacts. The Mk. 1 railgun was successfully tested to confirmed speeds of 450 m/s using a 1 gram projectile, giving a muzzle energy just over 100 J.

2.1.1 Power Supply

The power supply for the Mk. 1 system consisted of sixteen 10,000 µF Aluminum Electrolytic capacitors charged to 450 V, with a total stored energy of 16 kJ. The system avoided pulse-capable crowbar diodes by utilizing an inductive PFN (Pulse Forming Network, shown in Figure 2.

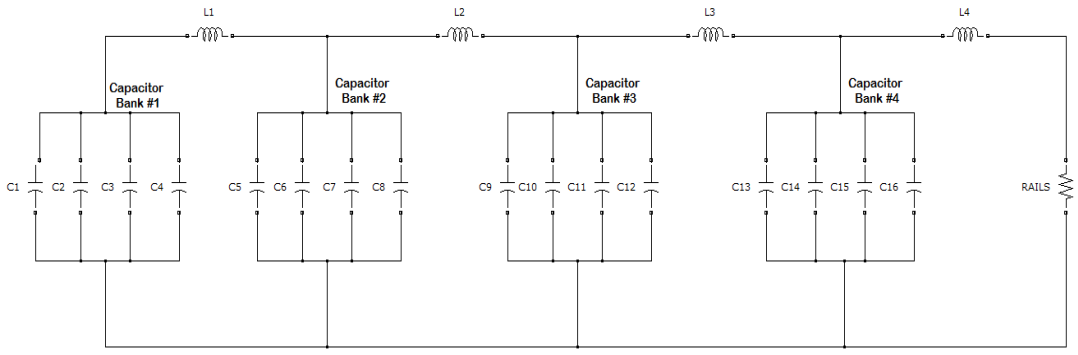

Figure 2 - Mk. 1 Power Supply

The system was not ideal because it did not protect the capacitors from reverse charge, leaving them susceptible to damage. The PFN was designed based on a Rayleigh Line PFN [5] as shown in the equations below:

$$L = R \cdot \frac{T}{N} \quad \textbf{Equation 4}$$

$$C = \frac{T}{(N \cdot R)} \quad \textbf{Equation 5}$$

where L is the inductance values in Henries, R is the load resistance in Ohms, C is each individual capacitor bank capacitance in Farads, and N is the number of capacitor banks in the system. However, with the high capacitance of this system and the longer pulse length relative to the small number of individual capacitor banks, the above equations do not accurately describe the operation of the pulse circuit. This circuit was designed to provide a high frequency, lower power, square wave pulse. Modification of the number of series capacitors and the inductance of the PFN inductors through trial and error via simulation results was required. The resultant inductances for each inductor ended up being 0.60 μH. This inductance left the system with an overall pulse length of about 1.3 milliseconds. The current in each of the capacitor banks is shown in Figure 3, and the overall projectile current is shown in Figure 4.

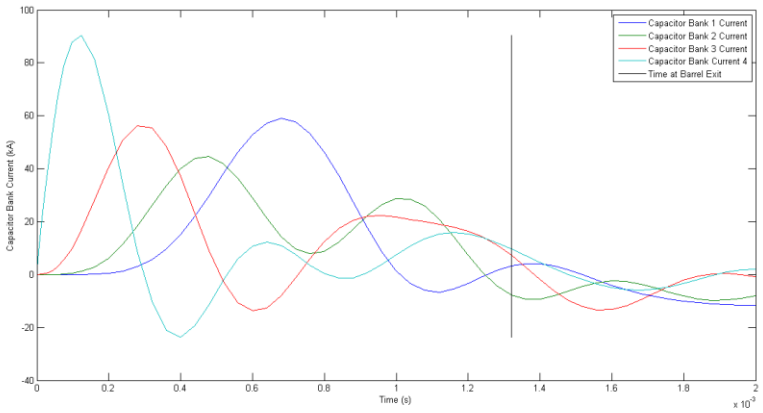

Figure 3 - Mk. 1 Simulated Capacitor Bank Currents

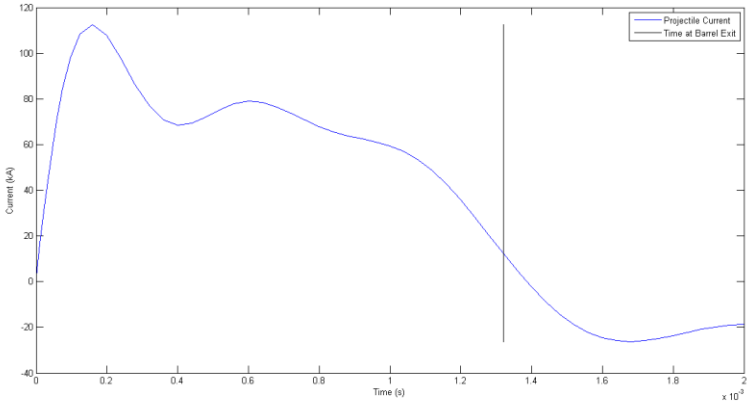

Figure 4 - Mk. 1 Simulated Projectile Current

This was a very oscillatory system, with complex interactions between each of the banks of capacitors. This complexity has an inherently low stability, resulting in a minimal chance of displaying the theoretical results shown in Figure 3 during a system test.

While a PFN type of power supply for a pulsed system is plausible, the electrolytic capacitors used in this PFN can suffer catastrophic failure when large reverse voltages are seen. Therefore failure of a component of the PFN network of capacitors, such as the failure of one of the circuit inductors, during a pulsed discharge can have drastic consequences.

2.1.2 Barrel

The Mk. 1 barrel was designed to be as simple and efficient as possible with no augmentation. The length was designed to transfer as much system energy to the projectile before it left the barrel. The simulations, as shown in the Figure 5, showed that a 36 inch barrel would be capable of capturing most of the pulse from the power supply, while giving the highest velocity possible.

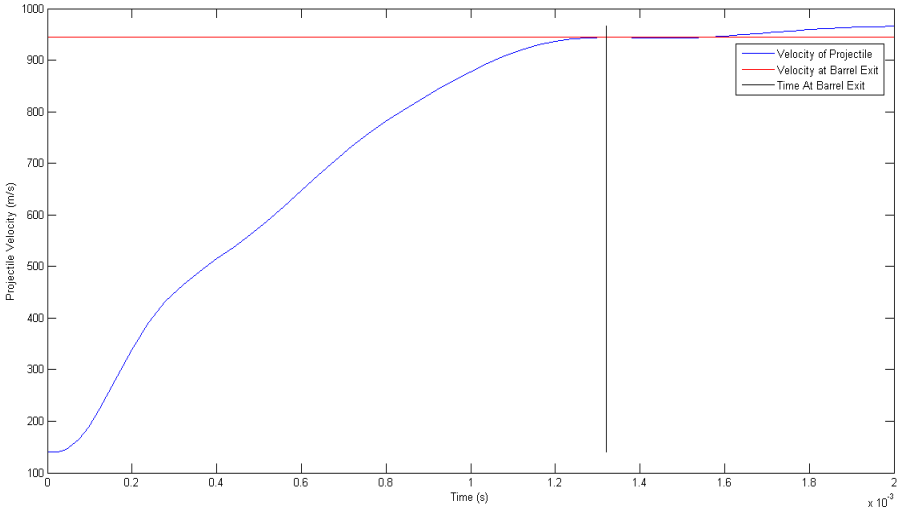

Figure 5 - Simulated Velocity Profile

The materials used in the barrel consisted of copper for the rails, structural fiberglass for the outer clamping structure, garolite for internal rigidity, and Teflon for the non-conducting projectile contact area. The parts of the barrel and barrel assembly are shown in Figure 6.

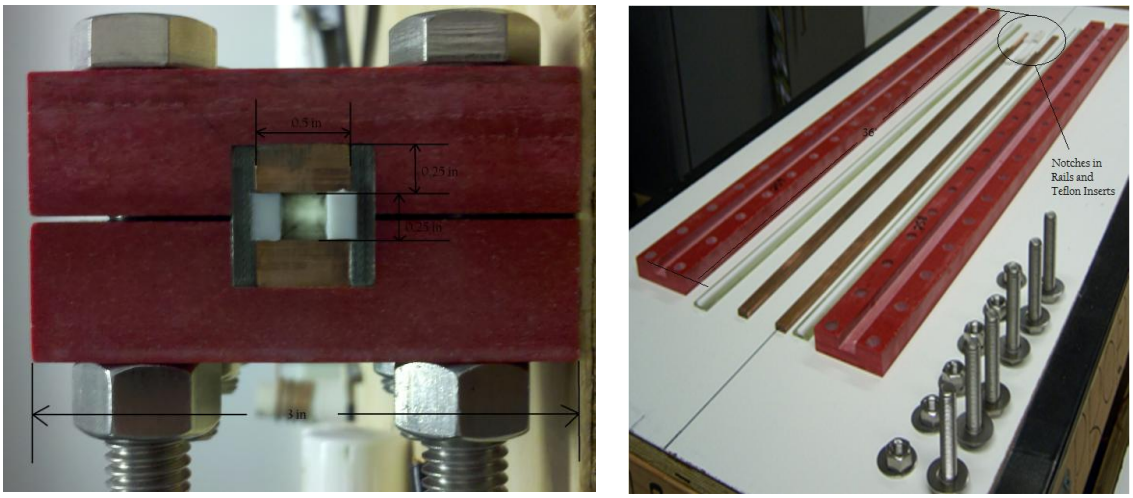

Figure 6 - Mk. 1 Muzzle (left) and Unassembled (right)

The Mk. 1 railgun utilized a 2,000 psi burst of compressed nitrogen to accelerate the projectile along a non-conducting (Teflon) pre-bore before the projectile contacted the copper rails 6 inches down the barrel. The injection system allowed for the magnetic field to mature before the projectile began conducting, ensuring that there was no reverse force on the initial projectile movement. It also allowed for an initial velocity on the projectile so energy was not wasted overcoming the static friction force of a non-moving projectile. Lastly, it allowed for the operation of the full system without any high power switching equipment, reducing cost and complexity a great deal. An image of the injection system block is shown in Figure 7.

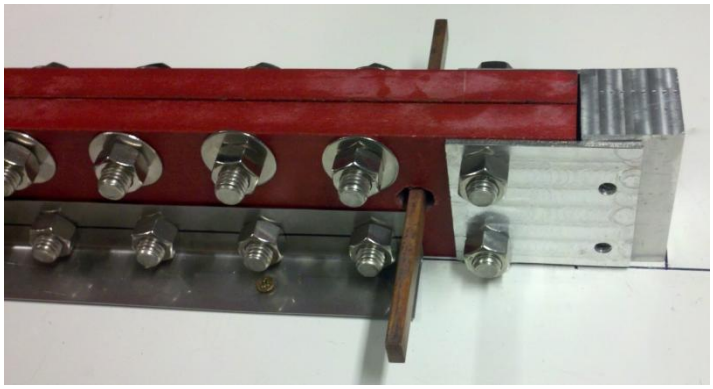

Figure 7 - Mk. 1 Injection Block

2.1.3 Testing Overview

Testing for the Mk. 1 railgun was a success, achieving confirmed speeds consistently at 450 m/s. The main contributor to the low efficiency of the Mk. 1 barrel can be attributed to contact resistance, which manifests in large amounts of arc damage and plasma generation. Figure 9 shows the stream of plasma following the projectile as it pierces a break screen and is beginning to penetrate the test shielding material. Generation of plasma during a shot is a visual sign of drastic efficiency loss caused by the projectile losing contact within the barrel as it accelerates. In turn this causes a large reverse voltage from the stored magnetic field energy in the barrel and pulse forming inductors. This large reverse voltage caused arcing both from the barrel to the projectile and arcing from rail to rail after the projectile had left the barrel. An example of this reverse voltage showing up in one of the tests of the Mk. 1 is shown in Figure 8.

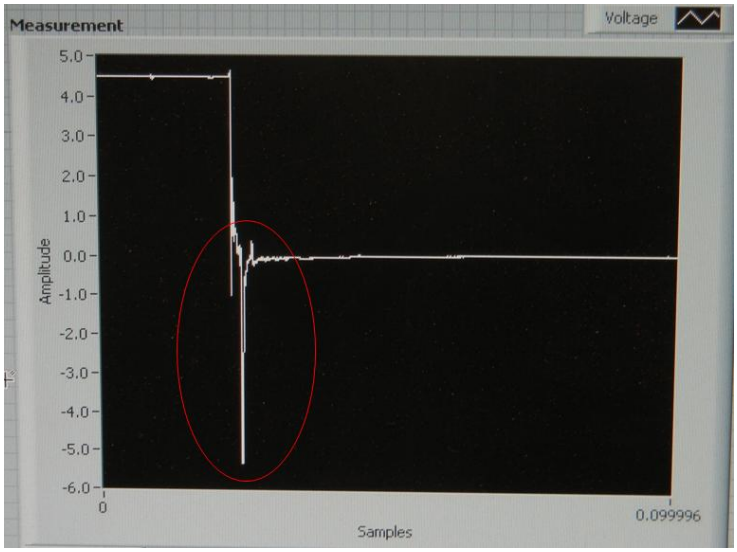

Figure 8 - Mk. 1 Inductive kick during testing

The red ellipse in Figure 8 outlines the section of the waveform where the inductive kick appears as the projectile left the barrel. The measurement is the breech voltage, and is 1/100th of the voltage at the breech, therefore showing a maximum negative voltage of 500 volts when the

projectile leaves the barrel. This is the cause of the large amount of plasma during tests, as shown in Figure 9.

Figure 9 - Mk. 1 Plasma during testing

Not only were these reverse voltages evident at the time of barrel exit, but they also occurred as the projectile moved down the barrel, causing heavy arc damage to the projectile and the rails. This effect potentially increased contact resistance significantly, decreasing maximum current and increasing thermal losses within the barrel. This would have contributed largely to the loss of projectile mass, shown by difference in the pre-firing and post firing projectiles in Figure 10.

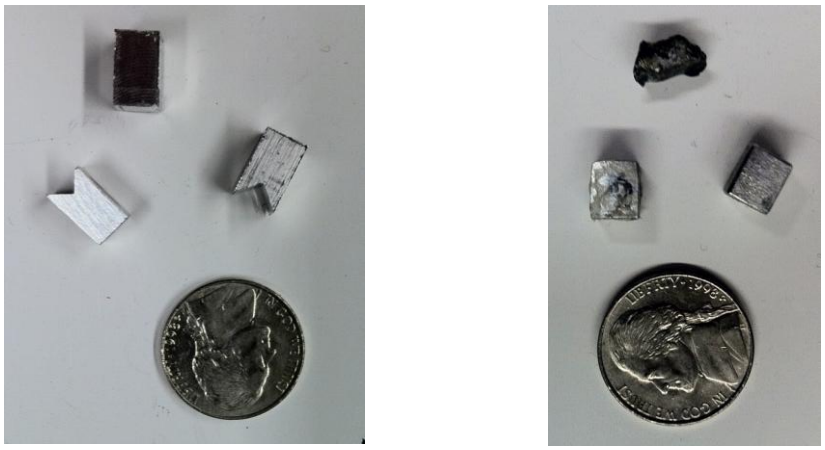

Figure 10 - Mk. 1 Projectiles Before (left) and After (right) firing

The top projectile in after image shows the rampant damage caused by a full voltage firing. The bottom right projectile was a zero charge test, while the projectile on the bottom left was a low voltage test, most likely between twenty and fifty volts. The mass loss of the projectile during a

450V test approached 50%. The Mk. 1.1 system sought to improve these disadvantages of the Mk. 1, increasing the efficiency of the system as well as the final velocity.

2.2 Mk. 1.1 power supply

The Mk. 1.1 utilized the same capacitors as the legacy Mk. 1 system, but re-arranged them into two parallel capacitor banks rather than four. Each bank was switched individually, and utilized its own PFN inductor. These PFN inductors were reused from the Mk. 1 Rayleigh Line PFN. The Mk. 1.1 power supply is set apart from the Mk. 1 by the Ignitron switching and a move to a Crowbar style discharge circuit.

2.2.1 Addition of Ignitron Switching

Ignitrons are large, high voltage, high current spark gap switches that utilize the breakdown of Mercury between the anode and cathode to close a circuit. They are operated by inducing a large voltage between the trigger pin and the cathode, forcing an arc between the two. When this arc has been generated the circuit is completed and can transmit large magnitudes of current.

Four NL7218H-100 ignitrons were donated to Cal Poly by an anonymous benefactor and fixed the design of the switching system for the Mk. 1.1 system around those switches. Each of the ignitrons has a maximum peak current rating of 100kA, with a maximum charge transfer per shot of 30 Coulombs. In order to stay within the operational limits of each ignitron, it was decided to utilize one ignitron for half of the capacitors, resulting in two parallel banks of capacitors.

When the Ignitron switching stand was put together, it was believed that the switches could operate in perfect parallel; one current load split evenly between the two switches. However, since there was an anode to cathode voltage required to maintain the generated arc, and there is an inherent switching delay between the two ignitron triggers, the voltage drop across one ignitron would go to effectively zero when the other ignitron began to conduct. The low voltage drop therefore prevents the second ignitron from triggering, forcing the first ignitron to take the full current pulse; leading to the final configuration shown in Figure 11.

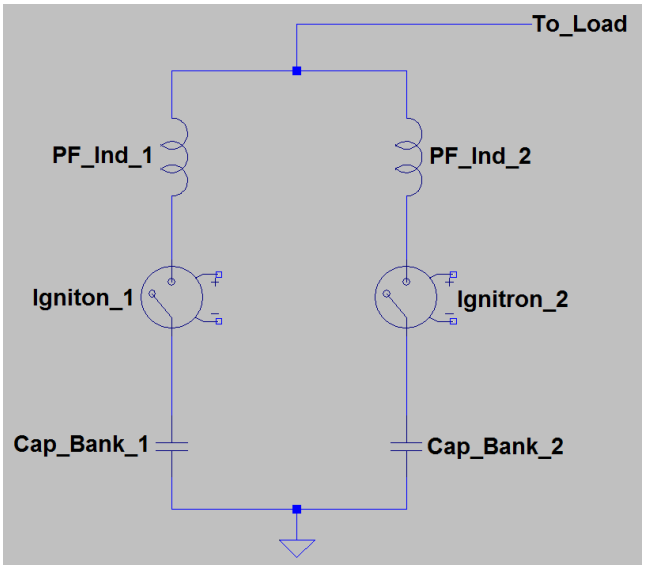

Figure 11 - Ignitron switching circuit schematic

The placement of the pulse forming inductors, PF_Ind_1 and PF_Ind_2, allow the ignitrons to switch offset from one another, while still allowing the slower ignitron to retain an anode to cathode voltage high enough to maintain an arc. This effect is due to the voltage and current relationship of an inductor.

$$V(t) = L\frac{dI}{dt} \qquad \textbf{Equation 6}$$

When the first Ignitron triggers the corresponding pulse forming inductor does not allow the current through it to rise too quickly, inducing a voltage drop across it that is high early on, and eventually lowers as the current rises. The voltage drop across this inductor is equal to the voltage drop across the second ignitron, assuming there is no voltage drop across the first ignitron.

2.2.2 Diode crowbar

The diode crowbar was added into the system to protect the capacitors from dangerous reverse voltages. In a crowbar circuit, a diode is placed in parallel with a capacitor so that if a system

begins to reverse in voltage due to circuit inductance, the diode then forward biases, clamping the capacitors to a voltage equal to the forward bias voltage drop of the diode. This effectively saves the capacitor from the dangerous reverse voltages of a pulsed system, but also requires some very large pulse current diodes, capable of the maximum current seen by the system. Two ABB 5SDD 50N5500 Rectifier Diodes were selected with the following ratings.

Table 1 - ABB Rectifier Diode Ratings [14]

Maximum Blocking Voltage	5000 V
Maximum Surge Current	$73x10^3$ A
Forward Biased Voltage Drop	0.8 V
Forward Biased Resistance	0.107 mΩ
Limiting Load Integral	$27.5x10^6$

These diodes were loaned from the Naval Postgraduate School in Monterey, CA. Two were used in our Mk. 1.1 system, one for each bank of capacitors. These diodes not only protect the capacitors, but they are placed past the ignitrons such that they will take a majority of the pulse instead of the ignitrons, increasing the operational lifetime of the already aged switches. This setup is shown in detail in Figure 12.

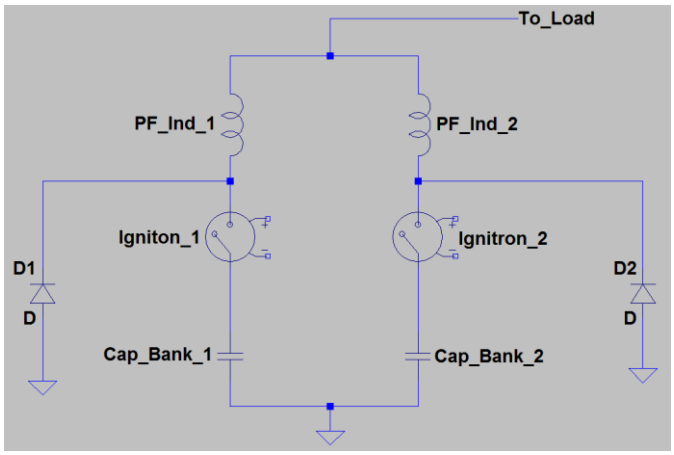

Figure 12 - Crowbar Diode Circuit Schematic

The equations governing the current output of a crowbar circuit are split into two sections, one prior to diode conduction, and one during diode conduction. Prior to diode conduction the circuit operates as an LCR discharge circuit. After diode conduction, the circuit operates as an L/R discharge, with all the energy stored within the magnetic field of the inductor. Diode conduction occurs once the voltage across the capacitors reverses enough to cause the diode to forward bias, typically between 0.5 and 2 volts. One can predict whether an LCR discharge circuit is going to oscillate by whether or not the following equation is true: [6]

$$1 - C\frac{R^2}{4L} > 0 \qquad \textbf{Equation 7}$$

where L is the system inductance in Henries, C is the system capacitance in Farads, and R is the resistance in Ohms. For the Mk. 1.1 system, prior to adding in parasitic inductances and resistances, Equation 7 was not satisfied, and therefore the system acted as an LCR discharge for the entire length of the pulse. This is due largely to the high capacitance of the electrolytic capacitors used for the Mk. 1.1 system as well as the added system resistance from the ignitron

switches. The crowbar diodes in the Mk. 1.1 circuit were left to ensure protection of the capacitors in case of unforeseen voltage transients.

2.3 Data Acquisition and Control system

The support systems for the Mk. 1.1 railgun consisted of power distribution, data acquisition, and control systems. These systems were all custom made for the railgun operations, and were changed frequently. Following is an explanation of the final configuration of the Mk. 1.1 support systems.

2.3.1 Power distribution and switching

The Mk. 1.1 system had several power and switching requirements, listed below:

- Switched and fused 208VAC power to capacitor power supply
- Switched 120VAC power to the Ignitron Triggering Circuit (ITC)
- Switched 120VAC power to the resistor bank relay
- 5V power to the ITC
- 5V power to the break screen TTL circuit

These requirements were satisfied utilizing a simple aluminum control box to switch the 120VAC and 208VAC power, delivering the power to the test cell through a single power cable. In the test cell there is a power distribution box that takes the power from the control room and from the DC lab power box and distributes the power to the ITC box, capacitor power supply, the railgun box containing the break screen circuit logic, and the resistor bank.

2.3.2 Data Acquisition equipment

The Mk. 1.1 system introduced new data acquisition equipment to monitor both current and voltage. The current monitored during tests was monitored using a Model 1423 Pearson Current Probe. The probe is capable of measuring current pulses with peak currents up to 500kA and

maximum energies of 75 Coulombs in a single shot. Voltage measurements on the Mk. 1.1 were taken in varying places during different tests.

2.3.3 Microprocessor control

The firing sequence, velocity (break screen) measurement, and data acquisition triggering were controlled by a central microprocessor, an Arduino Uno. A copy of the Arduino code can be found in 7.2.1.

2.4 Testing of the Mk. 1.1

The testing of the Mk. 1.1 was overall, a hardware failure. Testing was done in several stages, first testing the ignitron and ITC switching and secondly testing the actual firing of the gun. Current and voltage measurements were taken across the dummy load during several of these tests, examples of these tests can be found in section 7.3. This data found one important metric, and that was the voltage drop across the ignitrons was very large, contributing to most of the system losses. Also, the cabling setup, with 4 AWG cables running from:

- The capacitor bank to the ignitrons
- Ignitrons to the inductors
- Inductors to the load
- Load to diodes
- Diodes to ignitrons and inductors
- Diodes to capacitor bank

contributed a large amount of parasitic inductance to the system. This parasitic inductance, coupled with increased losses from cabling, the ignitrons, and additional connections, reduced the Mk. 1.1 peak current output to no greater than 30-40kA.

Once the operation of the system stabilized and the ignitrons were firing consistently, projectile tests were conducted. The projectiles were identical to the Mk. 1 projectiles, and were selected to be .002” to .003” larger than the bore of the Mk. 1.1 barrel. That allowed them to be interference fit and therefore theoretically fired with good, consistent bore contact. The severely reduced current output of the Mk. 1.1 capacitor bank led to a drastically lower projectile force. This force was not large enough to overcome the static friction forces in the barrel during either of the two functional projectile shots. These test results can be found in Section 7.3. Capacitor bank dummy load testing continued after the failed projectile tests in an effort to find a suitable solution. These tests ended with the explosive failure of one of the 16 electrolytic capacitors of the Mk. 1.1 capacitor bank. Testing was ceased as no suitable solution was found, either real or theoretical, because continued testing could have led to further damage of hardware.

3 Mk. 2 System

The Mk. 2 railgun system is designed to achieve projectile speeds over 2 km/s. It utilizes one capacitor bank on loan from the Naval Postgraduate School in Monterey, CA, a four turn augmented barrel, and an experimental three-part projectile. The main design goals are as follows:

1. Achieve impacts of 1 gram projectiles at speeds greater than or equal to 2km/s
2. Minimize cost per shot
3. Consistent projectile cross section and mass on impact.

Minimizing the cost per shot could have spanned systems with simple and cheap replacement parts that were swapped out often, to an extremely complex and robust system that needs little to no repair. Because of the requirement to maximize muzzle velocity while being limited to only one bank of capacitors, it was necessary to increase the efficiency of the impacting projectile to at least 3% in order to reach a projectile kinetic energy of 2kJ. More in depth explanations of the more detailed design decisions will be explained in the following sections.

3.1 Mk. 2 Model Development

The model utilized to predict the performance of the barrel consisted of magnetic field finite element (FEMM) simulations and a Matlab based Runge-Kutta ordinary differential equation solver called ODE45. The FEMM simulations modeled the magnetic field strength, inductance, and the resistance of the barrel over time. The Matlab solver uses the results from the finite element analysis and data from tests and research to simulate the electrical and mechanical response of the system over time.

3.1.1 FEMM Meta-Model

The FEMM software allows for the simulation of frequency-based, two dimensional magnetic field problems. In order to utilize this software for simulating a pulse of current through the barrel

over time, a relationship between time and frequency had to be defined. By taking the equation for skin effect in the time domain [7]

$$\delta(t) = 2\sqrt{\frac{t}{\pi * \sigma * \mu}} \qquad \textbf{Equation 8}$$

where t is time, δ is the skin depth in meters, σ is the material conductivity in Siemens/m, and μ is the material absolute permeability, and equating it to the frequency-dependent skin depth equation,

$$\delta(t) = \sqrt{\frac{1}{\pi * f * \sigma * \mu}} \qquad \textbf{Equation 9}$$

where f is frequency, cancelling terms and solving for time gives,

$$t = \frac{1}{4f} \qquad \textbf{Equation 10}$$

which is a theoretical relationship between frequency and time. This allows the use of a frequency domain solver, such as FEMM, for time domain problems.

From there Figure 13 and Figure 14 were generated based on the geometry of the gun loaded in FEMM, and curves fit to the data.

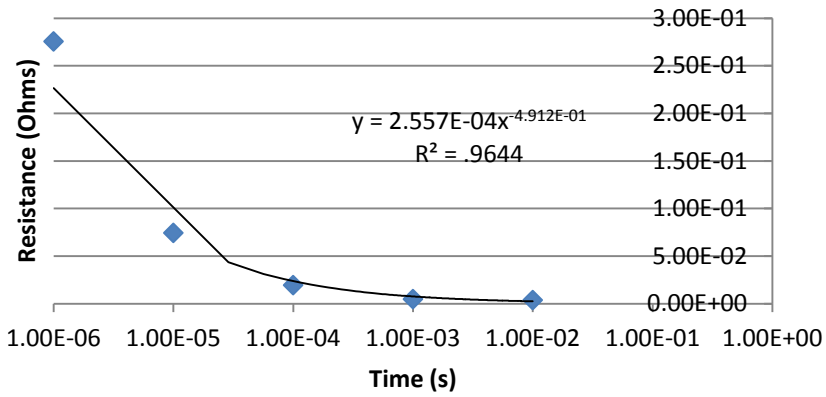

Figure 13 - Calculated resistance of gun over time

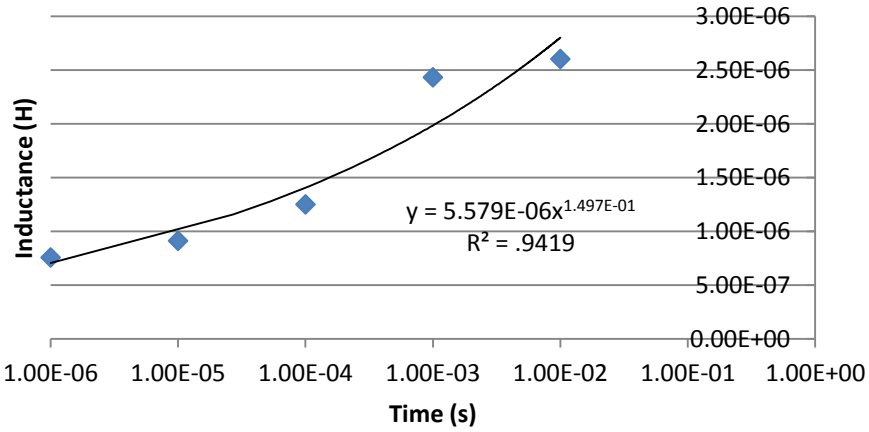

Figure 14 - Calculated inductance of gun over time

Figure 13 and Figure 14 show the estimated values and their fitted equations for the barrel's resistance and inductance. The R^2 values for the trend lines show good correlation of the data to the trend line. R^2 values are a representation of the amount of variability in the data is explained by the fit curve when compared to the variability explained by a constant value. Therefore, an R^2 value of 0.90 explains 90% of the variability present in the data. Furthermore, the resistance includes a stainless steel shunt bolt resistance adjusted for skin depth throughout the length of the pulse.

The meta model of the magnetic field within the barrel attempted to model the average field per unit current parallel to the rail contact as it changed with perpendicular distance from the rail to the center of the projectile over time. In order to do this, the magnetic field was averaged in the 'Y' direction, shown in Figure 15, by taking the field strength at the top of the projectile and averaging it with the field at the middle of the projectile. The purple regions represent areas of high, > 10T, field strength, whereas blue regions represent areas of low, < 1T, field strength.

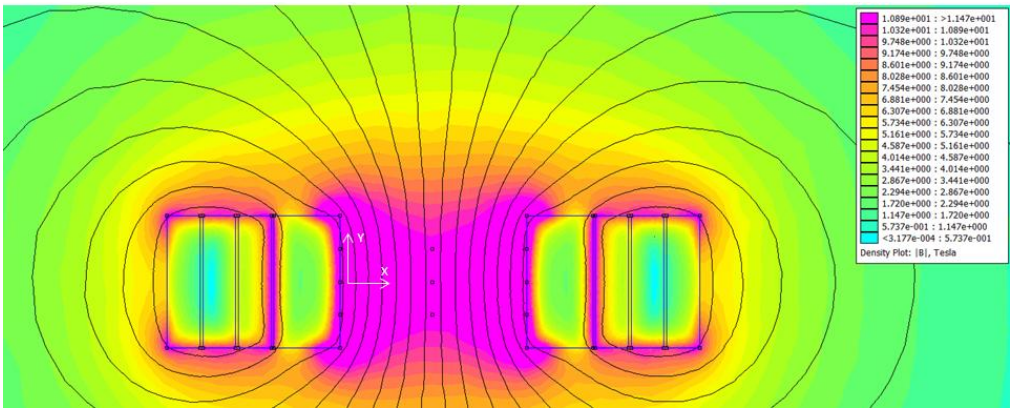

Figure 15 - Augmented magnetic field simulation

This gave several contours for change in field strength over the X-direction at different points in time. Power trend lines for these curves were generated, with high correlation, and the coefficients for the trend lines were plotted over time. Trend lines for these plots were generated and a final equation for magnetic field strength as it varies with position in the X direction and time was generated and follows:

$$\frac{dB}{dI}(X,t) = 5.472E-5 * e^{-3.512*10^{1}*t} * X^{-1.29*10^{-1}} \qquad \textbf{Equation 11}$$

where $\frac{dB}{dI}$ is the magnetic field strength per unit current in teslas/amp, and X is the distance from the rail contact surface in meters.

3.1.2 Model State Space

The ODE45 model utilized to solve the system of ordinary differential equations utilizes the derivative solutions of the state space variables to integrate the solutions to the system over a specified time span. The state space and solution variables are as shown in Table 2 below.

Table 2 - Mk. 2 Simulation State Space Variables

State Space	Derivative Space
Charge, q	Rate of change of charge, or current, $\frac{dq}{dt}$
Current, $\frac{dq}{dt}$	Rate of change of current, $\frac{d^2q}{dt^2}$
Average armature magnetic field, B_a	Rate of change of armature magnetic field, dB_a
Average projectile magnetic field, B_p	Rate of change of projectile magnetic field, dB_p
Position, x	Velocity, $\frac{dx}{dt}$
Velocity, $\frac{dx}{dt}$	Acceleration, $\frac{d^2x}{dt^2}$
Armature average temperature, T_{aa}	Rate of change of average armature temperature, $\frac{dT_{aa}}{dt}$
Armature maximum localized temperature, T_{am}	Rate of change of maximum armature temperature, $\frac{dT_{am}}{dt}$
Projectile average temperature, T_{pa}	Rate of change of average projectile temperature, $\frac{dT_{pa}}{dt}$
Projectile maximum localized temperature, T_{pm}	Rate of change of maximum projectile temperature, $\frac{dT_{pm}}{dt}$
Muzzle voltage, V_{muz}	Rate of change of muzzle voltage, $\frac{dV_{muz}}{dt}$

The solutions to the Derivative Space, as mentioned before, were integrated by the Matlab ODE45 solver for the final solution. The solutions to the derivative space are covered in the following sections.

3.1.3 Electrical Circuit Model

The following equations are all derived from standard electrical formulations, mainly Kirchhoff's Law. A diagram of the pulsed circuit, as modeled mathematically, is shown below in Figure 16.

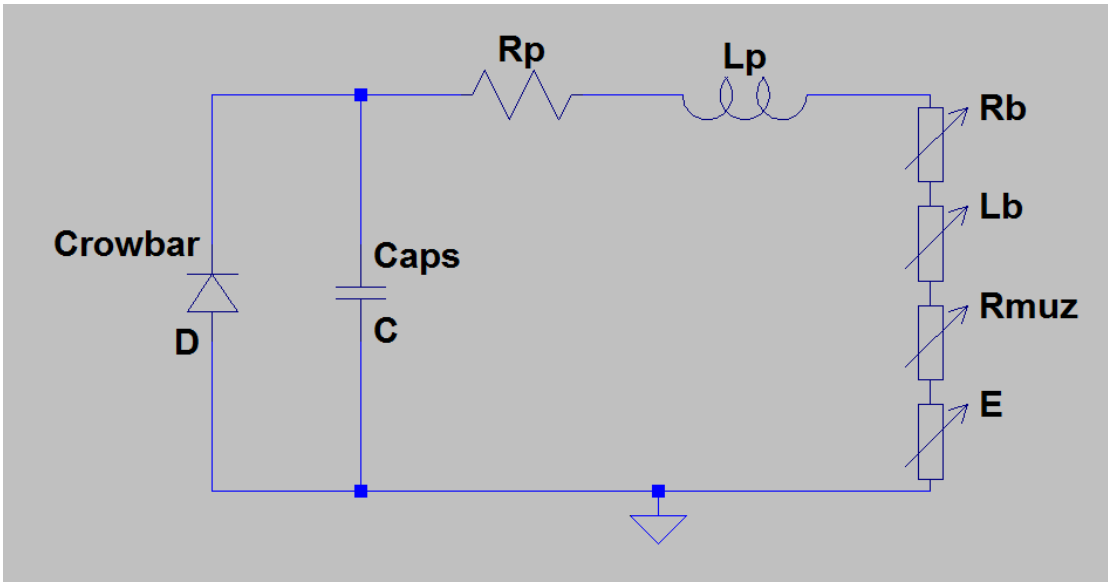

Figure 16 - Full 'as modeled' pulse circuit

Rp and Lp are the parasitic resistance and inductance as measured by testing the capacitor bank. The specific values will be covered later in Section 3.2.1. $Rmuz$ is the resistance of the muzzle of the gun, which includes the projectile, contact, and shunt resistor resistances. E is the back-EMF of the gun, to be referred to as ε for the remainder of this paper. Rb and Lb are the barrel resistance and inductance as they change with time and projectile motion. They take into account both standard skin depth and skin depth induced by projectile velocity, which is taken as an effective 'time' within the circuit, as follows [7]

$$t_{eff} = \frac{l}{2 * \frac{dx}{dt}} \qquad \textbf{Equation 12}$$

where t_{eff} is the effective time in seconds, and l is the length of an armature contact leg with the rails. This compensates for the addition of new rail material as the projectile accelerates down the rails.

The electric circuit model solves for the rate of change of the current through the load during two phases of the pulsed discharge: the capacitive discharge, and the inductive discharge. A circuit schematic of the capacitive discharge portion is shown in Figure 17.

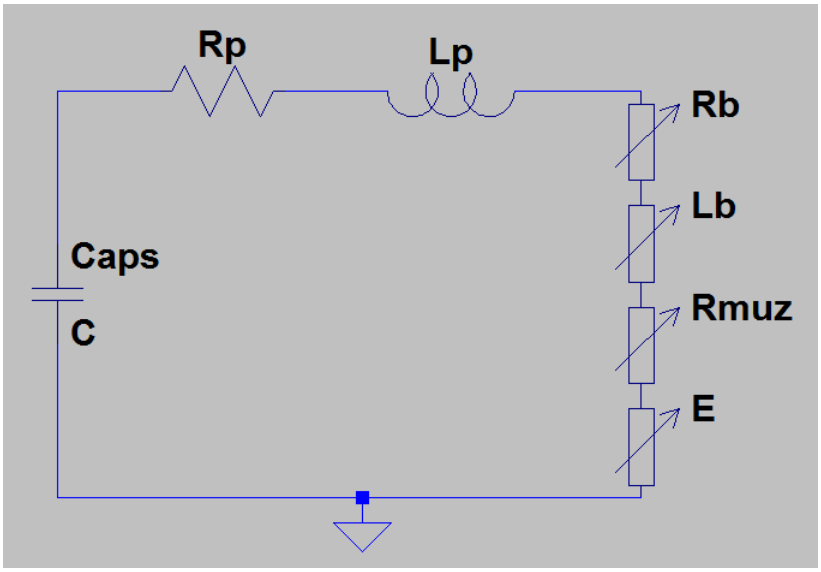

Figure 17 - Capacitive Discharge equivalent circuit

To solve for the rate of change of current for this circuit the voltage drops across the system impedances are equated to the voltage on the capacitors, as follows,

$$V_c = V_{R_p} + V_{L_p} + V_{R_b} + V_{L_b} + V_{R_{muz}} + \varepsilon \qquad \textbf{Equation 13}$$

where V_c is the voltage across the capacitor, ε is the back electromagnetic flux due to projectile motion [8], $V_{R_{muz}}$ is the voltage drop across the muzzle of the gun, V_{R_p} and V_{L_p} are the voltage drops across the capacitor bank parasitic resistance and inductance respectively, and V_{R_b} and V_{L_b} are the voltage drops across the railgun barrel resistance and inductance, respectively. Expressions for the voltage drop across the parasitic impedances are as follows.

$$V_{R_p} = R_p * \frac{dq}{dt} \qquad \textbf{Equation 14}$$

$$V_{L_p} = L_p * \frac{d^2q}{dt^2}$$ **Equation 15**

The voltage drops across the barrel's main impedances, R_b andL_b, are given by

$$V_{R_b} = \frac{dR_b}{dx} * x * \frac{dq}{dt}$$ **Equation 16**

$$V_{L_b} = \frac{dL_b}{dx} * x * \frac{d^2q}{dt^2} + \frac{dL_b}{dx} * \frac{dx}{dt} * \frac{dq}{dt}$$ **Equation 17**

due to the time and position varying properties of the impedance due to projectile movement. $\frac{dR_b}{dx}$ and $\frac{dL_b}{dx}$ are estimated using FEMM results and experimental readings. The muzzle voltage drop is gathered from the combined parallel resistance of the shunt resistor and the projectile resistance, as shown in Figure 18.

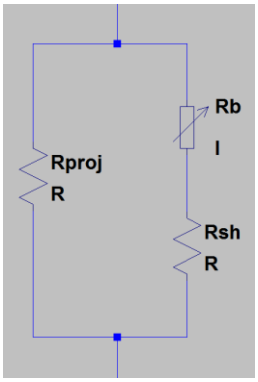

Figure 18 - Muzzle resistance circuit diagram

The voltage drop across this parallel circuit is given by

$$R_{muz} = \left(\frac{1}{R_{proj}} + \frac{1}{\frac{dR_b}{dx} * (P_f - x) + R_{sh}} \right)^{-1}$$ **Equation 18**

$$V_{R_{muz}} = R_{muz} * \frac{dq}{dt}$$ **Equation 19**

where R_{proj} is the resistance of the projectile including contact resistance, R_{sh} is the resistance of the shunt resistor, and P_f is the conduction length of the barrel. The rate of change of the muzzle voltage was modeled by the following equation.

$$\frac{dV_{R_{muz}}}{dt} = R_{muz} * \frac{d^2q}{dt^2}$$ **Equation 20**

The back-EMF, or ε, is a voltage drop induced within the barrel that accounts for the energy being converted from electrical to kinetic energy and frictional heating within the projectile and armatures. Without this term, the projectile acceleration would have no affect on the system energy as a whole. This back-EMF term is given by [8],

$$\varepsilon = \frac{dB_{avg}}{dt} * x * w + B_{avg} * \frac{dx}{dt} * w \qquad \textbf{Equation 21}$$

where B_{avg} is the average of the armature and projectile magnetic field strengths as a function of time, and w is the distance between the rail surfaces that contact the projectile in meters. Since $\frac{dB_{avg}}{dt}$ is directly dependent upon $\frac{d^2q}{dt^2}$ and vice versa, a newton's iteration was implemented for each time step to solve the system. The rate of change of the magnetic field was given by Equation 11 and averaged over the rail width. The rate of change of the magnetic field was able to utilize the overall magnetic field strength meta model due to,

$$\frac{dB_{avg}}{dI} * \frac{dI}{dt} = \frac{dB_{avg}}{dt} \qquad \textbf{Equation 22}$$

where $\frac{dI}{dt}$ is equivalent to$\frac{d^2q}{dt^2}$.

Therefore, by combining Equation 13 with Equation 14 through Equation 22, collecting terms, and solving for$\frac{d^2q}{dt^2}$, we are left with the following expression.

$$\frac{d^2q}{dt^2} = \left(\frac{1}{L_p + \frac{dL_b}{dx} * x}\right)\left[\frac{q}{C} - \frac{dq}{dt}\left(R_p + \frac{dL_b}{dx} * \frac{dx}{dt} + \frac{dR_b}{dx} * x + Rmuz\right) - \varepsilon\right] \qquad \textbf{Equation 23}$$

The inductive discharge portion of the pulse occurs after the capacitor has depleted its energy into the circuit inductance as magnetic field energy, and the resistance as thermal energy. The remaining energy within the inductors is then released and circulates through the crowbar diode, bypassing the capacitors, and accelerates the projectile further. This is the main portion of the

pulse, where the projectile extracts the majority of the energy from the system. The circuit diagram for this portion of the pulse is shown in Figure 19.

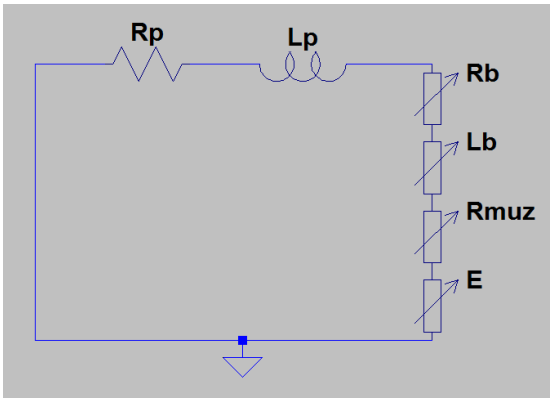

Figure 19 - Inductive discharge model

The voltage summation equation for the inductive discharge is as follows,

$$0 = V_{R_p} + V_{L_p} + V_{R_b} + V_{L_b} + V_{R_{muz}} + \varepsilon \qquad \textbf{Equation 24}$$

with an initial current equal to the peak current from the capacitive discharge simulation. Combining Equation 24 with Equation 14 through Equation 22 yields the expression:

$$\frac{d^2q}{dt^2} = -\left(\frac{1}{L_p + \frac{dL_b}{dx} * x}\right)\left[\frac{dq}{dt}\left(R_p + \frac{dL_b}{dx} * \frac{dx}{dt} + \frac{dR_b}{dx} * x + Rmuz\right) + \varepsilon\right] \qquad \textbf{Equation 25}$$

3.1.4 Thermal Model

The thermal model attempts to estimate the extent of the melting of the projectile and armatures during acceleration due to:

- Localized Joule heating due to contact resistance
- Average Joule heating due to material resistance
- Localized frictional heating

Rate of change of armature and projectile maximum temperatures are solved for by adding the localized heating and average heating solutions together, while the average temperatures were solved for by only the average joule heating due to material conductivity.

Nearing and Huerta, in Skin and Heating Effects of Railgun Current [9], present localized temperature of a point on the rails solved over time as:

$$T(x,y,t) = \frac{1}{\rho\sigma c}\int_{t_0}^{t} dt' * J^2(x,y,t) \qquad \textbf{Equation 26}$$

where $T(x,y,t)$ is temperature in Celsius/Kelvin in both position and time, ρ is the density of the material, σ is the material conductivity, and c is the specific heat per mass of the material. Taking the time derivative of this expression over time, yields

$$\frac{dT(x,y,t)}{dt} = \frac{1}{\rho\sigma c}J^2(x,y,t) \qquad \textbf{Equation 27}$$

which gives an expression for the joule heating within the armature and projectile due to material properties. In order to utilize this expression for the average and maximum joule heating, the current density is taken as an average or maximum from a FEMM current flow analysis, as shown in Figure 20.

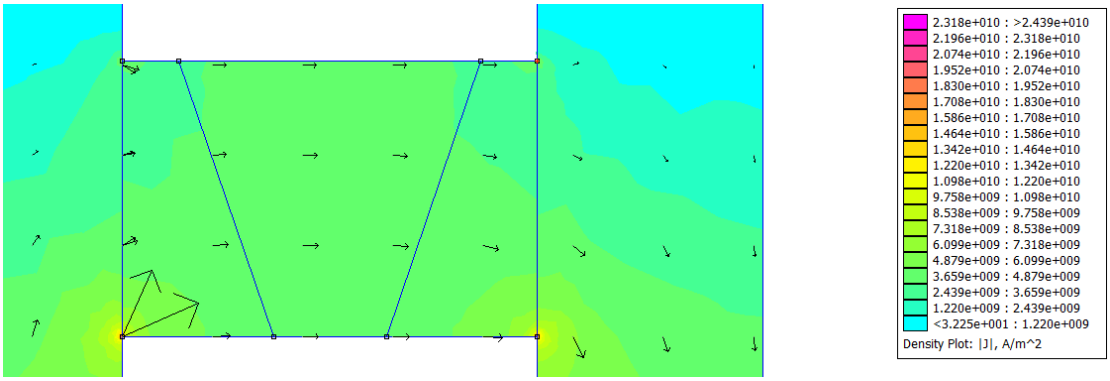

Figure 20 - FEMM current flow analysis

In order to define the contact resistance heating effects at the interfaces between the armature and rails and the projectile and armature, assumptions based on literature [7] had to be made. Assuming that there is an average of a 5 volt drop due to the contact resistance of a .25" x .25" contacting area, with a rail current of 100kA, a value for the contact resistance can be derived from the equation for contact voltage,

$$V_c = J * r_c \quad \textbf{Equation 28}$$

where V_c is the contact voltage, J is the current density, and r_c is the contact resistance, in Ωm^2. Using this equation, a value for r_c was found to be about $2.02e-9\ \Omega m^2$. This value is used in all analysis.

Using this value for the contact resistance between all contacting surfaces of the sabots, rails, and the projectile, the heating term due to contact resistance is defined as

$$\frac{dT}{dt} = J^2 * \frac{r_c}{(2\rho c \delta_c)} \quad \textbf{Equation 29}$$

where δ_c is the depth of contact in meters. This is the depth into the surface of the metal that the heat generated from the contact resistance is assumed to affect.

The final term for projectile heating to take into account is the heat generated due to projectile movement. This term, derived from the general equation for work, is given by

$$\frac{dT}{dt} = \frac{F_f V_p}{2\rho c A_c \delta_c} \quad \textbf{Equation 30}$$

where A_c is the full contact area between the sabot and rail surface, F_f is the force of friction between sabot and rail surface, and V_p is the velocity of the armature assembly. Combining Equation 27 through Equation 30 gives the full term for rate of change of temperature for the armature during projectile assembly acceleration:

$$\frac{dT}{dt} = \frac{1}{\rho c}\left[\frac{F_f V_p}{2A_c\delta_c} + J^2\left(\frac{r_c}{2\delta_c} + \frac{1}{\sigma}\right)\right] \quad \textbf{Equation 31}$$

The rate of change of temperate for the projectile assembly acceleration does not include the term for friction losses, and is therefore given by:

$$\frac{dT}{dt} = \frac{J^2}{\rho c}\left[\frac{r_c}{2\delta_c} + \frac{1}{\sigma}\right] \quad \textbf{Equation 32}$$

3.2 Mk. 2 Capacitor Bank

The Mk. 2 capacitor bank, on loan to California Polytechnic State University in San Luis Obispo, CA from the Naval Postgraduate School (NPS) in Monterey, CA, consists of:

- Two parallel 830µF General Atomics pulse capacitors
- One Primex ST-300A Spark Gap Switch
- One TG-75 Trigger Generator
- Sixteen ABB 5SDD 50N5500 Avalanche diodes
    - Ten used as crowbar diodes
    - Six used as output diodes
- Eight 100kΩ 225W Ohmite high power resistors
- Various resistive and resistive-capacitive snubber circuits

A schematic of the NPS capacitor bank can be found in Appendix Section 7.1. To charge these capacitors a 10kV, 10kW high voltage power supply that was fabricated and tested by NPS faculty is utilized. A schematic of this power supply can be found in 7.1.

3.2.1 Mk. 2 Cap Bank Testing

Capacitor bank testing was conducted in order to measure the properties of the capacitor bank during high current discharges, such as parasitic inductance and resistance. This was done by connecting the output of the capacitor bank to a large dummy load consisting of 4" square

graphite plates in a vice, allowing for controlled tuning of the dummy load resistance. With a known resistance of the load, current measurement through the load, and an additional voltage measurement across the load, the resistance of the load can be verified, the parasitic resistance of the capacitor bank could be calculated, and the parasitic inductance of the capacitor bank could also be calculated. From the rise time of the current pulse, from trigger to peak current, the system current can be described as a half-sinusoid with the following equation, and therefore the inductance in the system can be represented by [2]

$$L = \frac{1}{C}\left(\frac{2t_{rise}}{\pi}\right)^2$$ **Equation 33**

where C is the system capacitance in Farads and t_{rise} is the current rise time. This equation allows for a very good approximation of the system inductance of the circuit during operation. From there the system resistance can be calculated using the e^{-1} fall time, calculated from the current fall after the time of peak current, where diode conduction begins. The equation for the system current during the inductive discharge is given by

$$I = I_0 e^{-\frac{R}{L}t}$$ **Equation 34**

where I is the current after the fall from peak, I_0 is the peak current, and R is the system resistance. Measuring the fall time is done by subtracting the time of peak current from the time when the current is equal to

$$I = I_0 e^{-1}$$ **Equation 35**

in which

$$\frac{R}{L} t_{fall} = 1$$ **Equation 36**

reveals an expression for the system resistance. Rearranging gives

$$R = \frac{L}{t_{fall}} \qquad \textbf{Equation 37}$$

where L is solved for using Equation 33, and t_{fall} can be found through analysis of the load current waveform data.

Testing was therefore conducted on the Mk. 2 capacitor bank in order to ascertain its parasitic inductance and resistance. This was done by attaching a low resistance, high power, 'dummy' load to the output of the capacitor bank instead of the normal railgun load. The load current waveform for one of these 1000V tests is shown below.

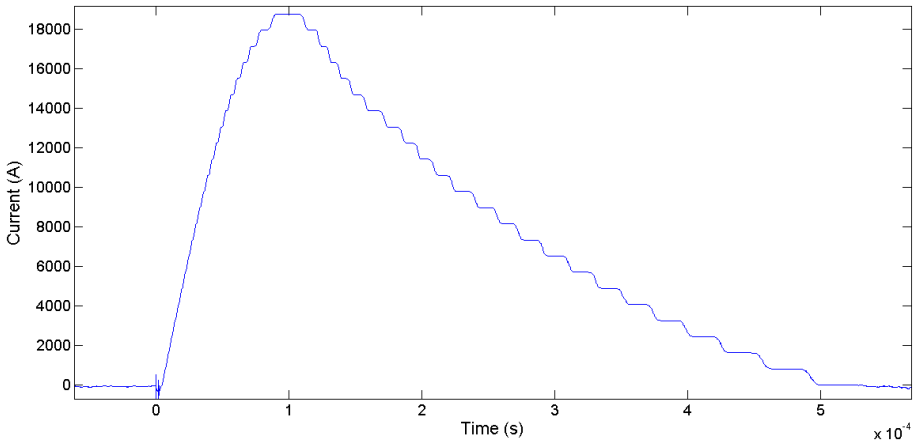

Figure 21 - 1000V Dummy Load Current Waveform

Analysis of this waveform gives the rise and fall times necessary to solve for the parasitic resistance and inductance of the system according to Equation 33 and Equation 37, along with other important information. The rise time is defined as the time from initial current flow to time of peak current, while the fall time is given as the time it takes for the current to fall from peak to the value determined by Equation 35, where I_0 is the peak current. The system properties are given as follows in Table 3.

Table 3 - Capacitor Bank system properties

Rise time	91 us
Fall time	200 us
System Resistance	10.2 mΩ
System Inductance	2.04 μH
Parasitic Resistance	1.5 mΩ
Switch Resistance	1.5 mΩ
Parasitic Inductance	2.04 μH

The system resistance is made up of three series resistances:

- Dummy load resistance
- Switch resistance
- Bus bar and diode resistances

During the testing, current and voltage was measured on the dummy load resistor. This information was used to calculate the average resistance of the dummy load over the entirety of the pulse. Since the measured resistance of the load varies so drastically, by about 1 mΩ, the bus bar and diode resistances were overwhelmed by the switch resistance and unnoticeable during the post test analysis.

3.3 Mk. 2 Barrel Design

3.3.1 Augmentation

The augmentation scheme for the Mk. 2 railgun barrel had two goals:

1. Eliminate the need for pulse forming inductance external to the capacitor bank and barrel.
    a. Ensures that crowbar and output diode ratings are not exceeded

b. Maximizes energy in the barrel's magnetic field, increasing the barrel's efficiency

2. Decrease damage to conducting rails and projectile by decreasing required current during a firing.

The design process was an iterative one, with new configurations being modeled in FEMM, and the system as a whole being modeled in a Matlab model.

The final augmentation scheme included 4 rails per side, a total of 3 pairs of augmenting rails in the following configuration. A visual representation of the augmentation scheme is shown in Figure 22.

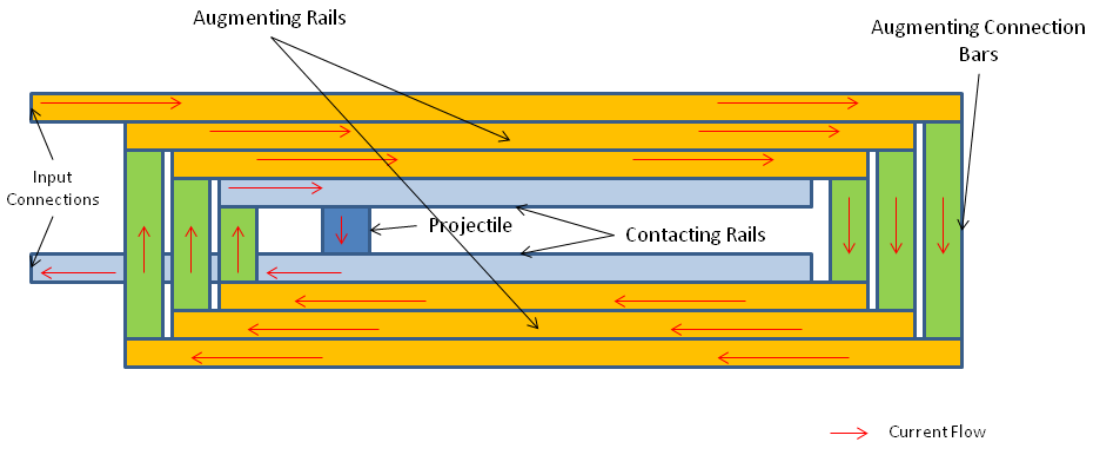

Figure 22 - Augmentation scheme and current flow

This augmentation allowed for strong and focused magnetic fields in the projectile plane, and increased the inductance of the barrel to allow the capacitor bank to fire directly into the railgun barrel, eliminating the need for an external inductance to limit peak current and rise times within safe limits. The number of augmenting rails was determined by the goal of eliminating that external inductance to maximize system efficiency. Therefore the majority of the energy stored in

the capacitors is stored in the barrel's magnetic field where it can be utilized to efficiently accelerate the projectile.

The length of the barrel was determined by pulse lengths generated during the simulated projectile acceleration, but was ultimately limited by the ability to manufacture. In order to keep the manufacturing done on the Cal Poly campus the length was limited to 48 inches in any direction. The amount of energy left in the system was therefore minimized, allowing for maximum energy transfer to the projectile.

In order to maximize the generated field, the augmenting rails needed to be as thin as was reasonable, with the space between rails as low as possible. For these two goals the thickness of the augmenting rails was selected to be 0.125", allowing for part availability and ease of manufacturing, and leads to a rail that is reliably rigid enough to be handled and worked with. The space between rails was minimized by utilizing layers of Kapton Polyimide high temperature tape. Each layer was .0035" thick, and a total of three layers were applied between the rails to allow for redundancy in case of the puncture of one layer. The Kapton tape is capable of withstanding temperatures up to 500ºF and voltages up to 7kV. Therefore three layers give proper voltage standoff while allowing for one layer to be punctured in any one location.

3.3.2 Structural Considerations

The structural dynamics of the Mk. 2 barrel are not simple, and are difficult to estimate using static methods but provide a rough estimate of the system. The static equations utilized as an initial method of calculating the maximum stresses in the outside structure of the barrel were the Euler Bernoulli beam equations, assuming a beam the length of the distance between the bolts, and a depth of 1 meter. Figure 23 shows a pictorial representation of the Euler-Bernoulli equation setup used to do rough calculations for the stresses in the structure.

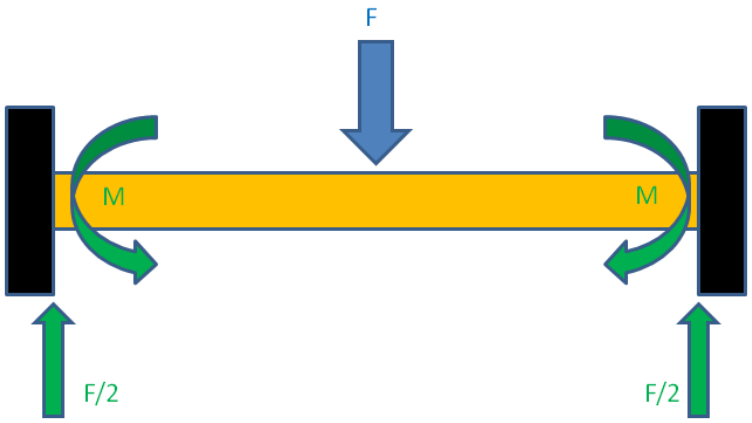

Figure 23 - Structural Beam Euler-Bernoulli Assumption

The equation for stress in the structure due to a point load at the center is given by [10]

$$\sigma = M * \frac{t_c}{2 * J} \qquad \textbf{Equation 38}$$

where σ is the maximum stress in the beam in Pascals, M is the maximum moment in the beam in Newton-meters, t_c is the thickness of the beam in meters, and J is the bending moment of inertia, in quartic meters, of the beam. The maximum moment in the beam is given by [10]

$$M = F * \frac{d_b}{8} \qquad \textbf{Equation 39}$$

where F is the force (Newtons) per meter exerted on the clamp structure by the railgun, and d_b is the distance between bolts on either side of the barrel in meters. With a 9000V pulse the expected peak current could be as high as 120kA, resulting in a force of about 675 kN/m on the barrel. Initially, the ultimate tensile strength of the FRP acquired from McMaster-Carr was believed to be [11] 3310 MPa, which was capable of taking this maximum pulse with a factor of safety of greater than 6. Later it is shown that the FRP material used for the outer clamps of the barrel was not that strong, and that incorrectly assumed tensile strength led to failure of the barrel structure.

3.4 Mk. 2 Projectile Design

3.4.1 Basic Principle

One of the largest problems with the effectiveness of railguns is the damage that the projectile and rail do to one another during a firing. The common railgun projectile is a solid piece of conducting material, usually aluminum or molybdenum, and this projectile is interference fit, meaning the projectile is larger than the bore by a small fraction of the projectile width, with thousands of pounds of force to ensure that contact is retained as the projectile loses material. This practice creates a large friction force that must be overcome at initial projectile movement, which can lead to failure of the shot, drastic melting of the projectile and rails, and large losses in efficiency as so much work must be done to overcome this frictional force. These exact problems are what largely led to the failure of the Mk. 1.1 system during projectile tests.

To overcome the problem of losing projectile contact due to melting or trading contact for a difficult interference fit, a novel projectile first designed by Dr. Bill Maier while he was a professor at the Naval Postgraduate School was researched, kinematic equations derived, and was finally fabricated and tested. This projectile, instead of being one solid structure, is made of 3 parts, two sabots and one main projectile that are allowed to slide relative to another on an angled wedge surface. This allows the engineer to design the frictional and normal force between the rail and projectile assembly based on the input current, rather than position down the rails.

For an initial prototype of the projectile assembly, aluminum was used for both the sabots and the main projectile. A part drawing of the projectile is in Appendix Section 7.5.

3.4.2 Derivation of Kinematic Equations

The kinematic equations for this projectile assembly assume:

- Current travels along the back wall of the sabots and main projectile

- The angle of current travel through the sabots is dictated by the dy and dx (geometric constants of the sabots)
- Magnetic torques on projectile and sabots are negligible
- Forces generated by current flow can be assumed normal to direction of current, and originate from the half way point of the total flow of travel
- Gravitational effects are neglected, being assumed negligible

The full assembly free body diagram is shown in Figure 24 below.

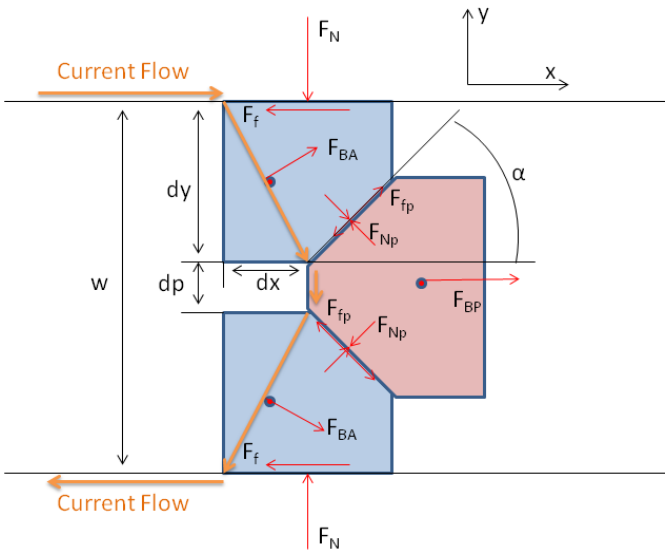

Figure 24 - Projectile Assembly Free Body Diagram

F_{BA} and F_{BP} are the forces generated on the sabots and projectile, respectively, due to the current flowing through the magnetic field of the barrel. The forces are given by

$$F_{BA} = B_A dx I_p \hat{\imath} + B_A dy I_p \hat{\jmath} \qquad \textbf{Equation 40}$$

$$F_{BP} = B_P dp I_p \qquad \textbf{Equation 41}$$

where F_{BA} and F_{BP} are the forces generated on one of the sabots and the projectile respectively, due to the average magnetic field strength in the armature and projectile. The average magnetic

field is given by B_A and B_P for the sabots and the projectile, respectively. Furthermore, dx, dy, and dp are geometric dimensions of the sabots and projectile, as shown in Figure 24. Lastly, I_p is the magnitude of the current flowing through the projectile assembly. From here the sum of forces in the x direction can be solved to find the overall force on the projectile assembly, and finally the acceleration of the projectile can be calculated as follows,

$$\sum F_{x,assembly} = F_T = 2F_A + F_P = a_T(2m_A + m_P) \quad \textbf{Equation 42}$$

where F_T is the total force on the projectile assembly, F_A and F_P are the sum of x-direction forces in the sabots and projectile respectively, a_T is the total projectile assembly acceleration, and m_A and m_P are the sabot and projectile masses, respectively. F_A, the sum of forces in the y-direction within the sabot, and F_P are given by

$$\sum F_{x,sabot} = F_A = a_T m_A = B_A dy I_P - F_{NP}(\sin(\alpha) + \mu_{AP}\cos(\alpha)) - \mu_{AR}F_N \quad \textbf{Equation 43}$$

$$\sum F_{y,sabot} = 0 = F_{NP}(\cos(\alpha) - \mu_{AP}\sin(\alpha)) - F_N + B_A dx I_P \quad \textbf{Equation 44}$$

$$\sum F_{x,projectile} = F_P = a_T m_P = B_P dp I_P + 2F_{NP}(\sin(\alpha) + \mu_{AP}\cos(\alpha)) - F_D \quad \textbf{Equation 45}$$

where F_D is the drag force on the projectile given by a subsonic approximation of

$$F_D = \frac{1}{2}\rho A_p C_D V_P^2 \quad \textbf{Equation 46}$$

where ρ is the density of air, A_p is the area of the projectile in the velocity direction, and C_D is the coefficient of drag.

By rearranging Equation 43 and Equation 44 and solving for variables F_N and F_{NP}, the following expressions can be extracted

$$F_N = \frac{m_P B_A dy I_P - m_A (B_P dp I_P - F_D)}{\left[\frac{1}{B_A dx I_P + \frac{C_R}{m_T}}\right] + m_P \mu_{AR}} \quad \textbf{Equation 47}$$

$$F_{NP} = \frac{m_P (B_A dy I_P - \mu_{AR} F_N) - m_A (B_P dp I_P - F_D)}{C_2 (2m_A + m_P)} \quad \textbf{Equation 48}$$

where C_2 is one of two "Projectile Interface Coefficients", and C_R is the "Projectile Interface Ratio" given by

$$C_1 = \cos(\alpha) - \mu_{AP} \sin(\alpha) \quad \textbf{Equation 49}$$

$$C_2 = \sin(\alpha) - \mu_{AP} \cos(\alpha) \quad \textbf{Equation 50}$$

$$C_R = \frac{C_1}{C_2} = \frac{\cos(\alpha) - \mu_{AP} \sin(\alpha)}{\sin(\alpha) - \mu_{AP} \cos(\alpha)} \quad \textbf{Equation 51}$$

Finally, the projectile assembly acceleration is given by a rearrangement of Equation 43.

$$a_T = \frac{1}{m_A} [B_A dy I_P - F_{NP} (\sin(\alpha) + \mu_{AP} \cos(\alpha)) - \mu_{AR} F_N] \quad \textbf{Equation 52}$$

3.5 Simulated Barrel Performance

The system parameters for a shot at maximum voltage give the following variables:

Table 4 – Simulation Parameters

Capacitor Charge	9000 V
Capacitance	1660 µF
Bank Resistance	1.5 mΩ
Bank Inductance	2.04 µH
Shunt Resistance	20 mΩ
Projectile Assembly Mass	2.4g

The simulation shows extremely hopeful results, with a final velocity exceeding 3500 m/s (seen in Figure 25), and a total projectile assembly efficiency of 23.94%. Taking into account only the main projectile kinetic energy, the projectile efficiency is 9.98%. This is assumed to be a large over-estimation, but even so, should meet the design goal of 2000 m/s. Figure 25, Figure 26, and Figure 27 show the performance of the gun as predicted by the model.

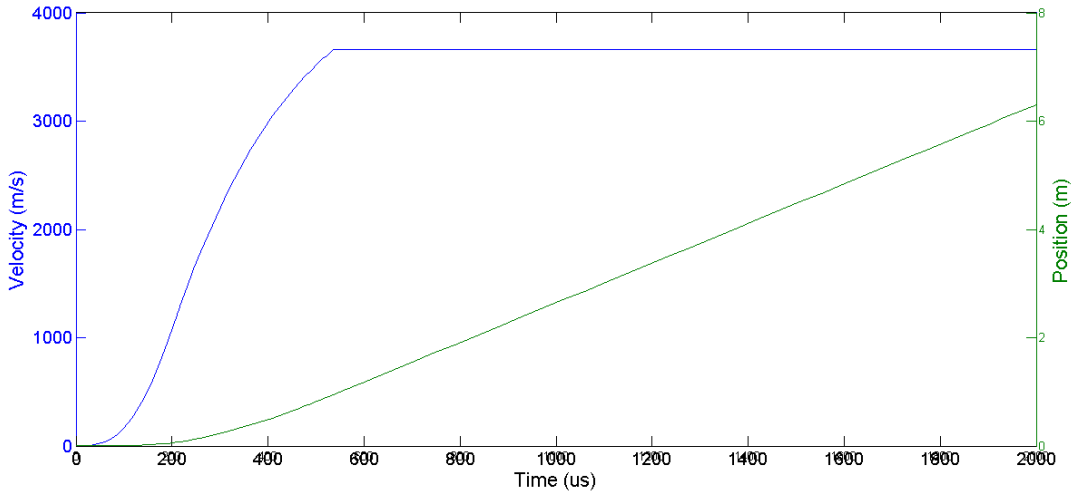

Figure 25 - Velocity and Position Simulation Results

The velocity of the projectile flattens at just over $500us$, when the projectile leaves the barrel. This shows the utilization of a majority of the energy stored in the capacitors when compared to the current plot in Figure 26.

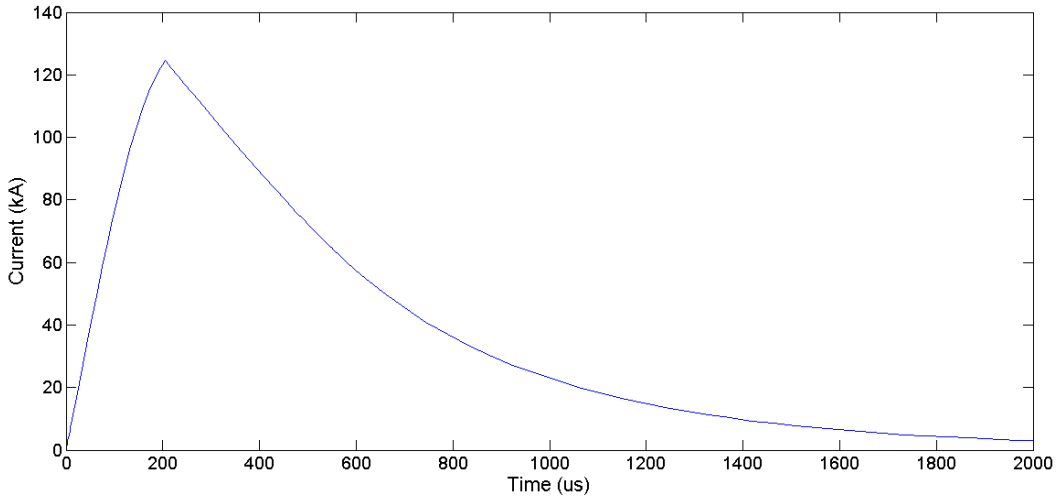

Figure 26 - Current Waveform Simulation Results

Energy stored in the inductance of the circuit is directly related to the square of the instantaneous current. Since the current is about one half of the peak current when the projectile leaves the barrel, the remaining energy is about 25% of what was originally stored in the inductance of the system. The magnetic field strength is almost three times the field generated by the Mk. 1 system at the same current. Paired with the larger bore width as compared to the quarter inch barrel width of Mk. 1 barrel, this makes for a high efficiency barrel, approaching 24% of the energy transferred from the capacitive storage to overall kinetic energy. The average magnetic field strength of the sabot and projectile is shown in Figure 27.

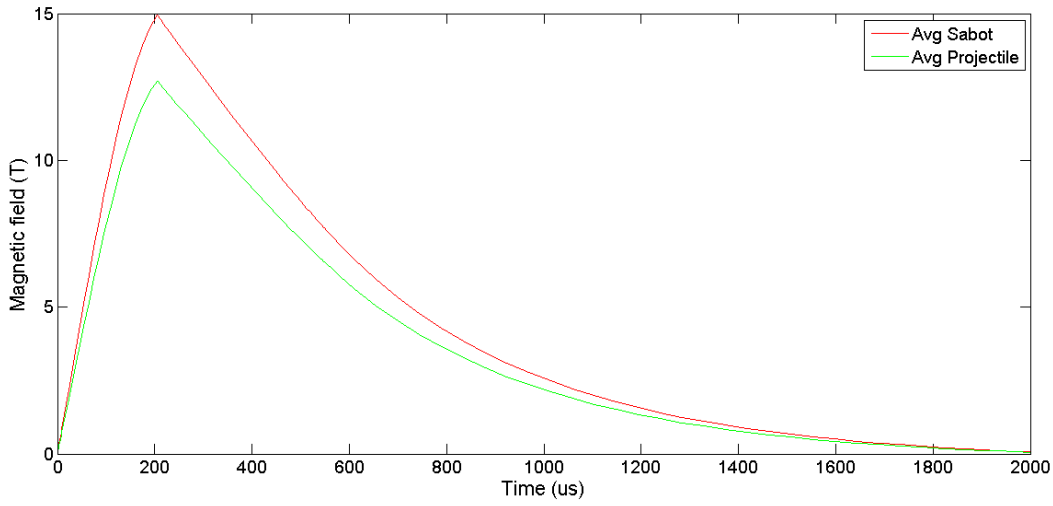

Figure 27 - Barrel Magnetic Field Simulation Results

The average sabot magnetic field is higher than the average projectile magnetic field due to the geometry of the magnetic field within the barrel. The magnetic field is strongest at the rail surface, and falls to a minimum at the center of the barrel. The average field of the sabot is taken from the field spanning from the rail surface to the length dy, given by sabot geometry. The average projectile field strength is taken from the average field over length dp of the projectile geometry.

Average and maximum sabot and projectile temperatures are simulated as well. The results show that there should be a generous amount of melting of the sabots, whereas the projectile should remain intact. The results are shown below in .

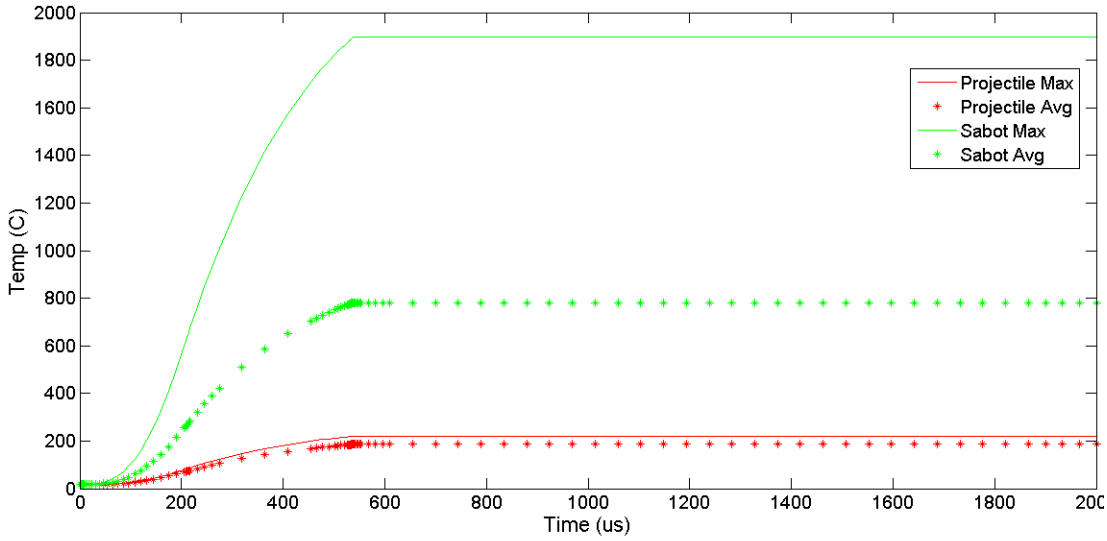

Figure 28 - Temperatures of Sabots and Projectile over Time

3.6 Mk. 2 Testing and Results

Testing of the Mk. 2 barrel was completed in three phases. Phase 1 consisted of measuring the barrel's properties using an LRC meter, with the shunt resistor completing the circuit. Phase 2 consisted of testing of the barrel's structural, magnetic, and functional integrity with no projectiles being fired. Phase 3 consisted of firing projectiles, measuring barrel current, muzzle voltage, and acquiring velocity from the high speed camera video and break screen measurements.

3.6.1 Phase 1 Testing - LRC Measurements

In order to update the model with a more accurate representation of the barrel inductance and resistance, the parameters were measured using an LRC meter and four wire Kelvin resistance measurement. The results of the measurements, as compared to the calculated values, are shown in Figure 29 and Figure 30.

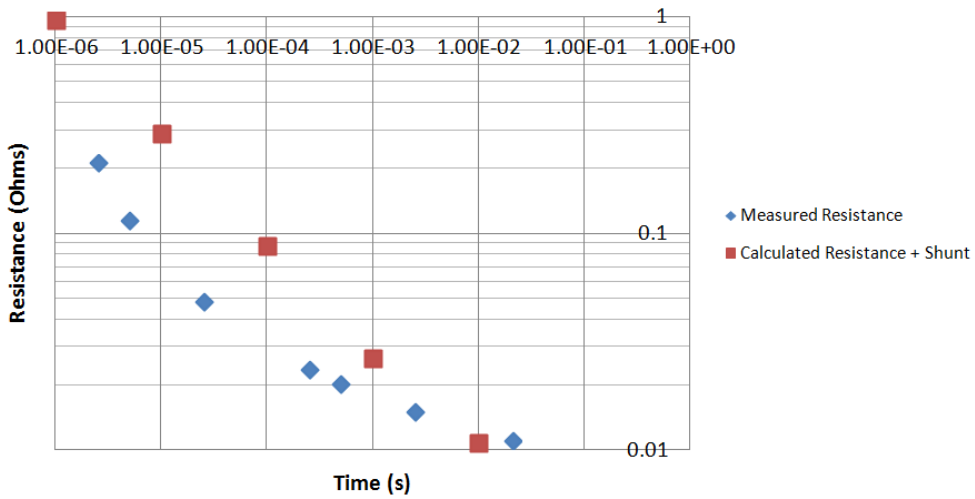

Figure 29 - Mk. 2 Calculated vs. Measured Resistance

The calculated and measured resistances are fairly similar, with the measured resistance being lower than the calculated values overall. This is most likely due to the structural 'wings' on the sides of the rails. This excess material was not taken into account in the FEMM models, and would decrease the resistance if the current partially flowed into the wings when available. These decreases in current density will decrease the magnetic field generated, and therefore the efficiency of the gun as a whole.

Figure 30 shows the relationship between the measured and calculated inductance of the Mk. 2 gun. Interestingly, at effectively high frequency, which corresponds to shorter time since pulse start, the measured and calculated values almost perfectly agree. However as the pulse time lengthens, corresponding with a decrease in effective frequency, the measured inductance increases by almost an order of magnitude. This is another effect of the structural wings that extend from the sides of the rails. At lower frequency the current density through these wings increases, decreasing the average current density in the center of the rails, causing the measured values to deviate very far from the calculated model, as the model did not include these wings.

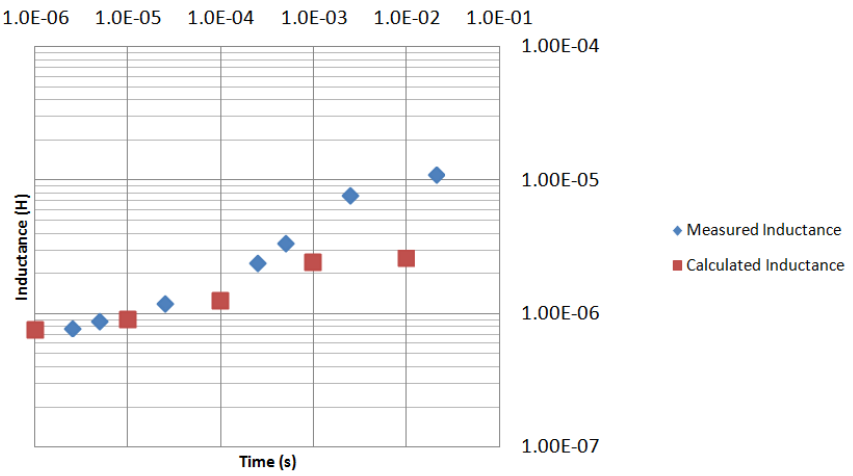

Figure 30 - Mk. 2 Measured vs. Calculated Inductance

Overall, the static tests with the shunt resistor completing the circuit showed that the barrel will operate as expected, but will however have some additional efficiency loss due to the unaccounted for structural wings.

3.6.2 Phase 2 - 'Dry Fire' Testing

'Dry Fire' testing was completed to test the properties of the railgun, with the shunt resistor completing the barrel circuit instead of an unpredictable projectile. This allows inspection of the Mk. 2 barrel characteristics in a pulse scenario, where the structural integrity of the gun can also be tested safely and taken into account. Initial testing failed, causing arcs between augmenting rails due to poor Kapton coverage and damage to Kapton insulators during assembly. Figure 31 shows the current waveform during a 3000V dry fire test where the insulation had failed. The current peaks at over 60kA, a larger current than the designed barrel current at voltages of only 3000V.

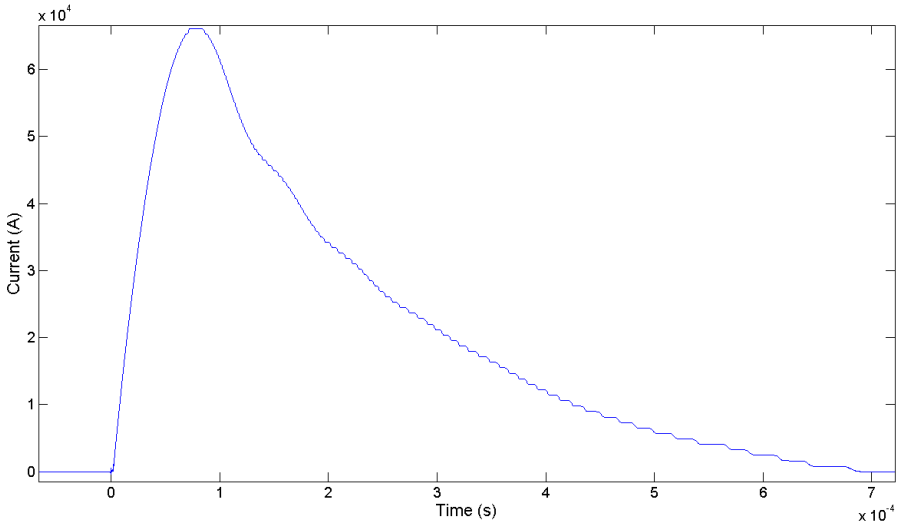

Figure 31 - Current waveform, Arcing failure

After disassembling the barrel, it was clear that the arcs occurred at points of either poor Kapton coverage, or where the Kapton insulators had been compromised. Figure 32 shows an example of this Kapton damage.

Figure 32 - Mk. 2 Internal arcing damage

Repair of the Kapton and changes to the taping layout succeeded in preventing internal and external arcing in the system during subsequent testing. The successful dry fire test, after the re-taping, resulted in a very quiet, 30kA peak current waveform as shown in Figure 33.

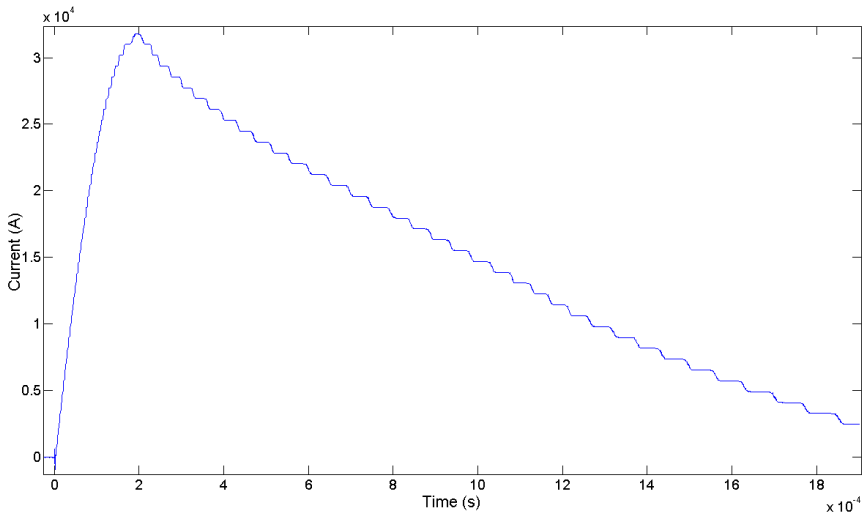

Figure 33 - Current waveform, no internal arcing

The lower peak current and greatly increased pulse length shows that the larger impedance of the gun is maintained and the energy stored in the capacitors is going toward generating the large magnetic field within the barrel. The previous internal arcing dissipated this magnetic field as it gave the current another, much shorter, path to reference, effectively 'skipping' the barrel entirely.

Table 5 shows the electrical characteristics of the circuit and the Mk. 2 barrel as derived from the firing data shown in Figure 33 using the equations laid out in Section 3.2.1. The gun resistance and inductance are derived from the overall circuit resistance and inductance after subtracting the values for the capacitor bank and switching losses found in Section 3.2.1.

Table 5 - Mk. 2 Pulsed Electrical Characteristics

Rise Time	190 µs
e^{-1}Fall Time	976 µs
Circuit Resistance (Average)	8.9 mΩ
Circuit Inductance (Average)	8.7 µH
Barrel Resistance (Average)	7.5 mΩ
Barrel Inductance (Average)	7.2 µH
Barrel Magnetic Field Max Energy	3.63 kJ
Barrel Magnetic Field Efficiency	48.58%

The magnetic field energy can be calculated using following derivation. First, the equation for voltage drop across an inductor is given by

$$V = L\frac{di}{dt} \quad \textbf{Equation 53}$$

with i being current, and L being inductance of the element of interest (in this case the railgun barrel), and t being time. Continuing, the power dissipated through this element is given by

$$P = Vi \quad \textbf{Equation 54}$$

with P being power dissipated, in this case power converting capacitive energy into magnetic field energy, in Watts. Substituting the voltage drop across an inductive element, Equation 53, the final term for power dissipated by the pure inductive element of the railgun barrel can be derived as follows:

$$P = Li\frac{di}{dt} \quad \textbf{Equation 55}$$

The power feeding the barrel's internal magnetic field over time is shown in Figure 34.

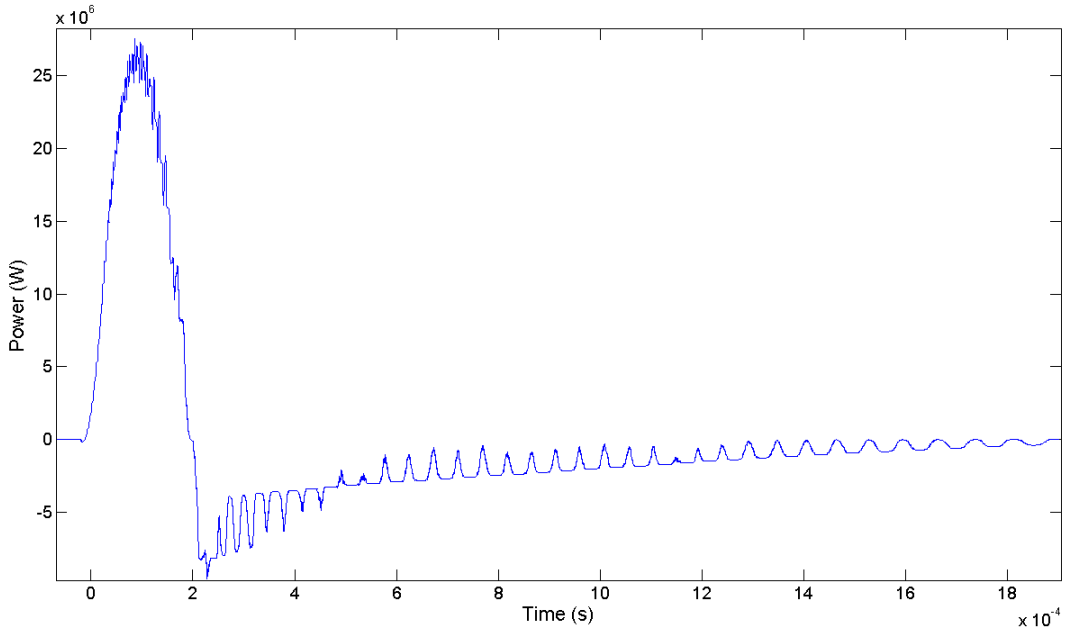

Figure 34 - Inductive power storage over time

The point where the power switches from positive to negative is where the current is circulating through the crowbar diodes, dissipating the energy stored in the circuit inductance. This can be shown by integrating Equation 55 over time, yielding the equation,

$$E = \int_0^t Li\frac{di}{dt} \qquad \textbf{Equation 56}$$

where E is the energy stored in the magnetic field of the barrel, in Joules.

As shown in Figure 35, the magnetic field energy storage follows the same curve as the barrel current. Therefore inductive energy storage is at a maximum when the capacitive energy storage is at a minimum and the crowbar circuit begins to conduct. During these tests, with no projectile being fired, all of the energy stored in the capacitors, then subsequently stored in magnetic fields in the barrel and system, is dissipated as heat by means of the resistive elements of the system. During projectile tests it is expected that about 25-50% of the energy stored in the magnetic field of the barrel will be converted to kinetic energy in the projectile by means of the Lorentz Force.

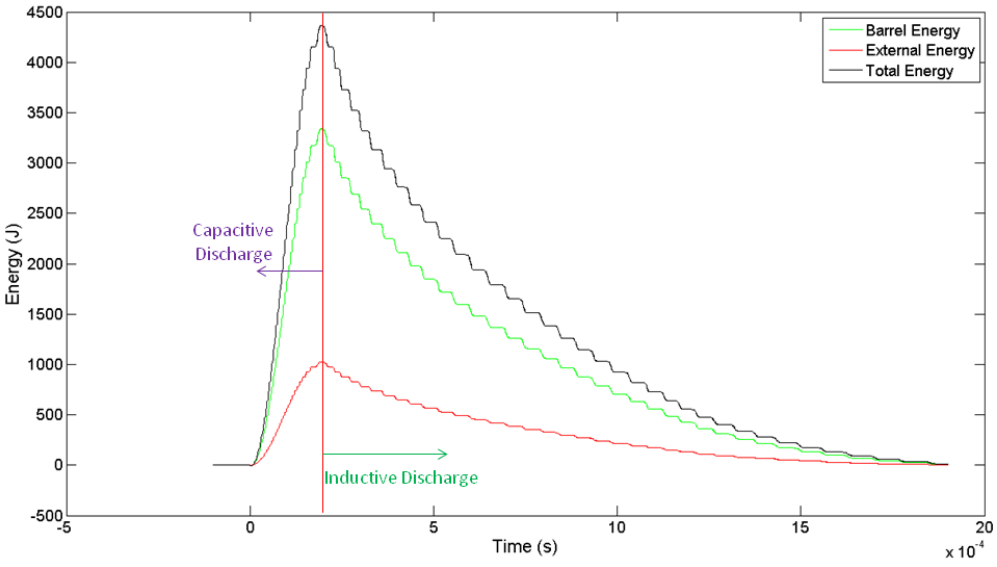

Figure 35 - Barrel magnetic field energy over time

3.6.3 Phase 3 - Projectile Testing

Initial projectile testing resulted in major projectile failure. The sabots did not move due to static friction, and the main projectile was accelerated forward by the Lorentz Force, as it was not held back by the static friction seen by the sabots. As the projectile attempted to accelerate, the only thing holding it to the sabots was the nylon screw. This screw was easily sheared by the large forces near the peak current of the pulse, and the projectile was sent flying down the barrel alone, coming out at speeds from 40-200 m/s. In an attempt to prevent the screw from shearing, the nylon screw was replaced by a steel screw. During this test the steel screw was pulled from the projectile, ripping the aluminum threads out with it. While the screw was being ripped from the projectile, the sabots did gain some acceleration and came out behind the projectile, but at a severely reduced velocity.

Figure 36 shows the geometry of the proposed projectile failure. The rotation of the sabots due to forces between the set screw and the sabots during initial acceleration dig into the rails and induce

a very large force on the small screw, either shearing the screw or ripping it from the projectile as was the case with a steel screw replacement.

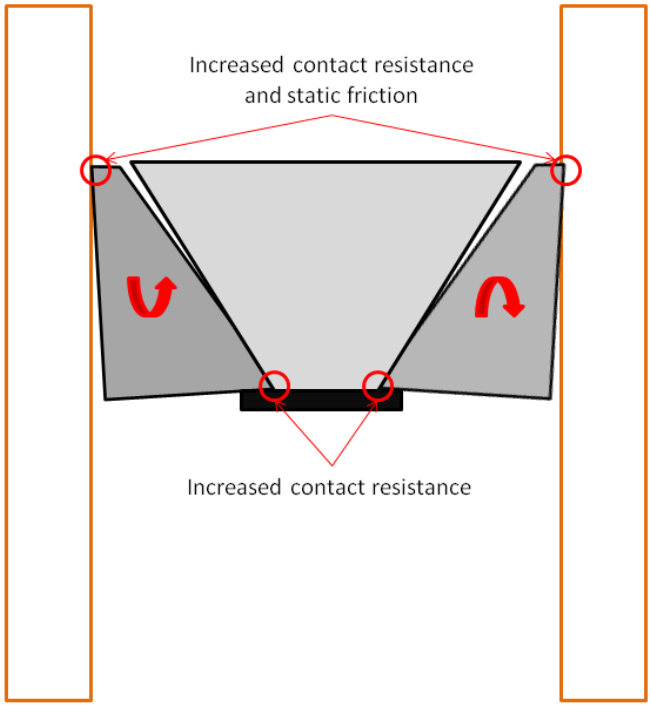

Figure 36 - Projectile Failure Image

Figure 37 shows the current waveform for the first projectile test shot. The current waveform shows the fast dissipation of energy stored in the circuit inductance as it converted the energy to projectile kinetic energy and melting of the projectile.

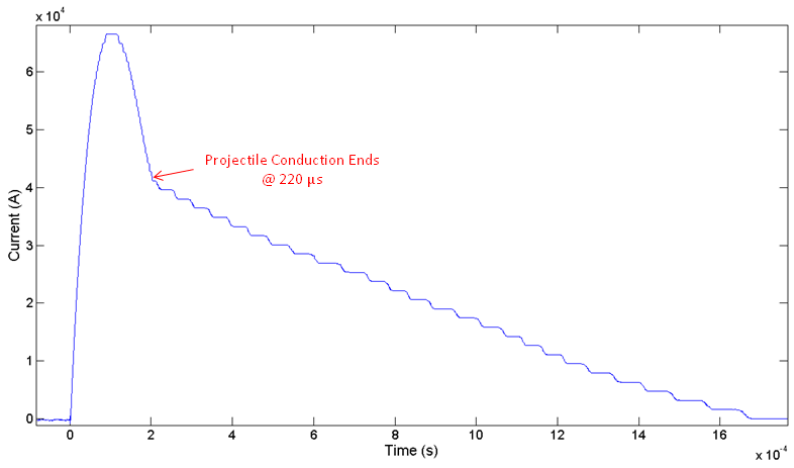

Figure 37 - Current Waveform for shot #1

Due to the very low resistance of the shunt bolt compared to the heightened sabot/rail contact resistance the projectile conduction portion of the circuit has a much larger current drop. This means that energy was being utilized somewhere else, either in accelerating the projectile or in melting the projectile and rails. The increased contact resistance increased heating and melting between the rails and the sabot, and this was manifested in aluminum deposits on the rails, and an average sabot mass loss of 0.04g and average projectile mass loss of 0.07g.

Table 6 shows the circuit characteristics and performance results obtained from the first projectile test.

Table 6 - Shot #1 Results

Test Voltage	3000V
Rise time	88.5 µs
Fall time	126 µs
Maximum Current	66.5 kA
Estimated System Inductance	1.91 µH
Estimated Barrel Inductance	0.444 µH
Projectile Velocity	41.7 m/s
Projectile KE	2.3 J
Overall Efficiency	0.031 %

3.6.3.1 Modified Projectile Testing and Structural Failure Analysis

In an attempt to solve the initial binding and instability of the projectile both a

projectile attachment and surface additives were tested. The projectile attachment was a simple aluminum arc with a hole at the center to allow for the set screw. The final assembly of the projectile is shown in Figure 38.

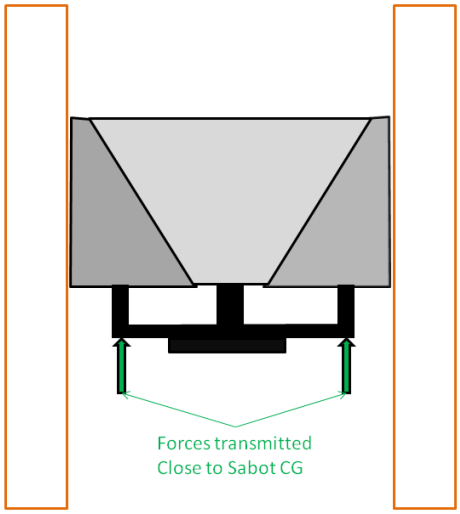

Figure 38 - Modified Projectile Assembly

The goal of this projectile attachment was to transmit the force exerted on the sabots from the set screw on the CGs of the sabots, reducing the moments generated and preventing initial rotation of the sabots. This does not affect any of the kinematic equations described earlier, except for adding weight to the screw and projectile assembly, thereby decreasing overall acceleration of the projectile. These effects are relatively negligible.

The first projectile test with this new configuration was done at 5kV, with a 6" portion of spray-on graphite lubricant at the breech, to decrease the friction coefficient between the sabots and the rail surface, aiding in projectile movement. This had minor success, but still failed to prevent the set screw from being ripped out of the projectile. Also, current flowed through the aluminum attachment, bypassing the projectile and crushing the attachment due to the large electromagnetic forces within the barrel. Images of the failed projectile for this test are shown in Figure 39.

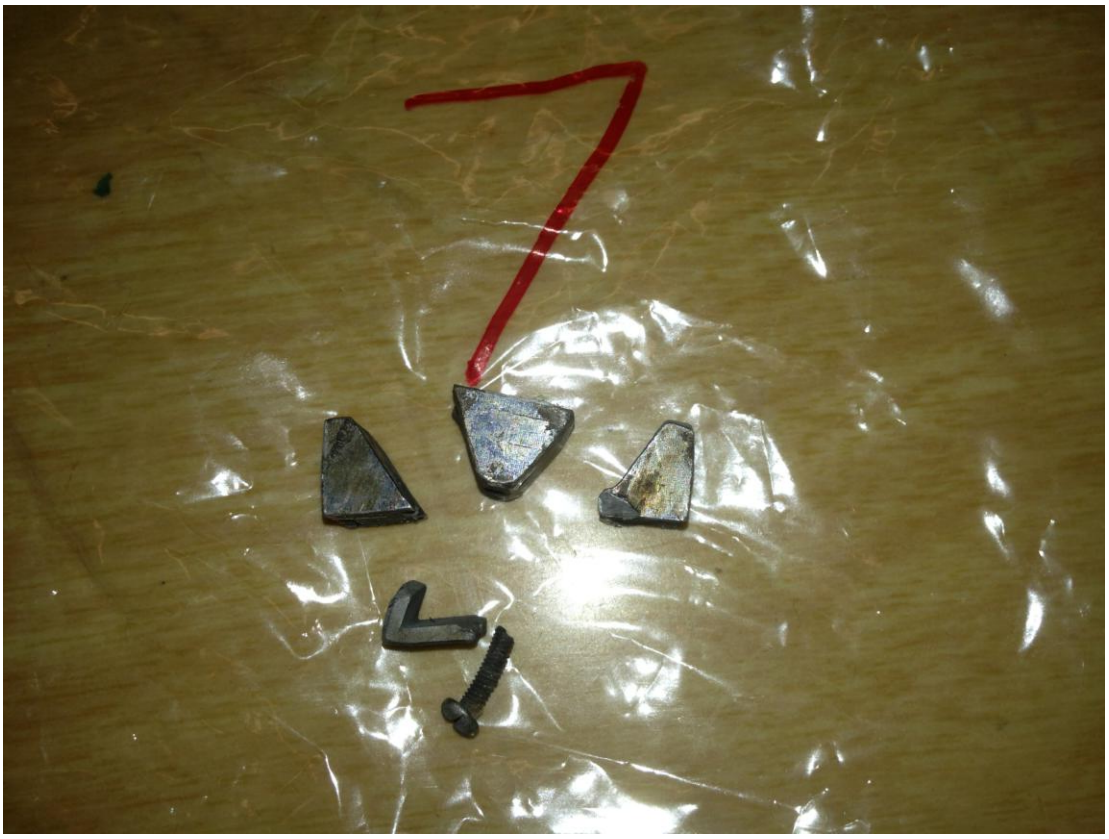

Figure 39 - Projectile test recovered projectile

The second and final projectile test with the new attachment utilized silver paste and insulation on the projectile attachment. However this test ended in the rupture of the fiberglass outer barrel structure due to large amounts of internal arc failure. This was unexpected, as the design factor of safety for a 9000V shot was over six. The test voltage was 5000V and consisted of a final main projectile velocity of about 150 m/s, with one sabot remaining in the barrel and the other leaving the barrel and not making it to the target.

The internal arcing damage after this shot showed that the insulation protecting rails 1 through 4 was compromised, causing the current to jump straight to the contacting rail toward the muzzle end of the gun, and reverse direction, going straight back to the projectile. This phenomenon is shown in Figure 40.

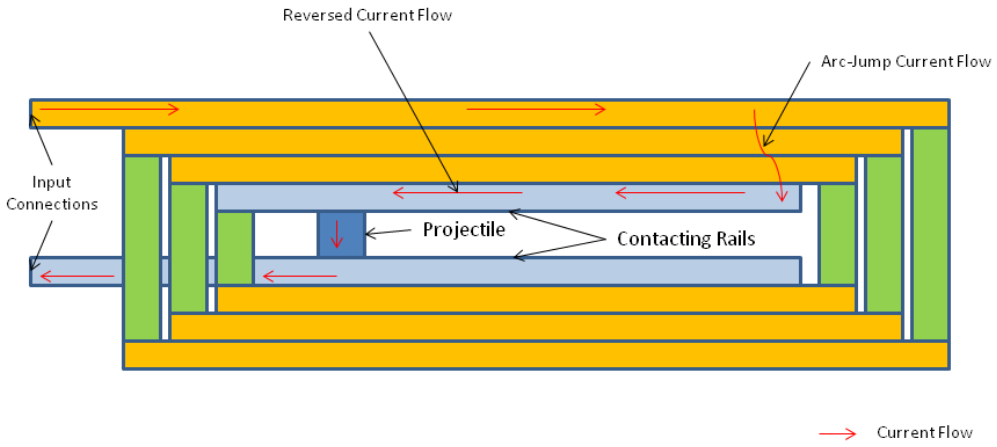

Figure 40 - Arc failure current flow illustration

As the current jumped over rails 2 and 3, it lowered the impedance of the barrel and therefore the entire circuit, allowing the peak current to jump from an expected 60kA to a large 120kA. This spike in current, and the proximity of the reverse current to the input rail, could have caused forces up to 900kN/m. This force, according to initial calculations, should have been easily handled by the fiberglass structure. After examining the root cause of the failure in depth, it was found that the tensile strength that was used during the design process was not a valid assumption, and that McMaster-Carr actually reports a tensile strength for this FRP material in the range of 68 MPa to 413 MPa [12]. This large range gives a Factor of Safety from less than 0.25, to approaching but less than 1.0, which explains why this particular failure occurred. An image of the failure seen within the fiberglass is shown in Figure 41.

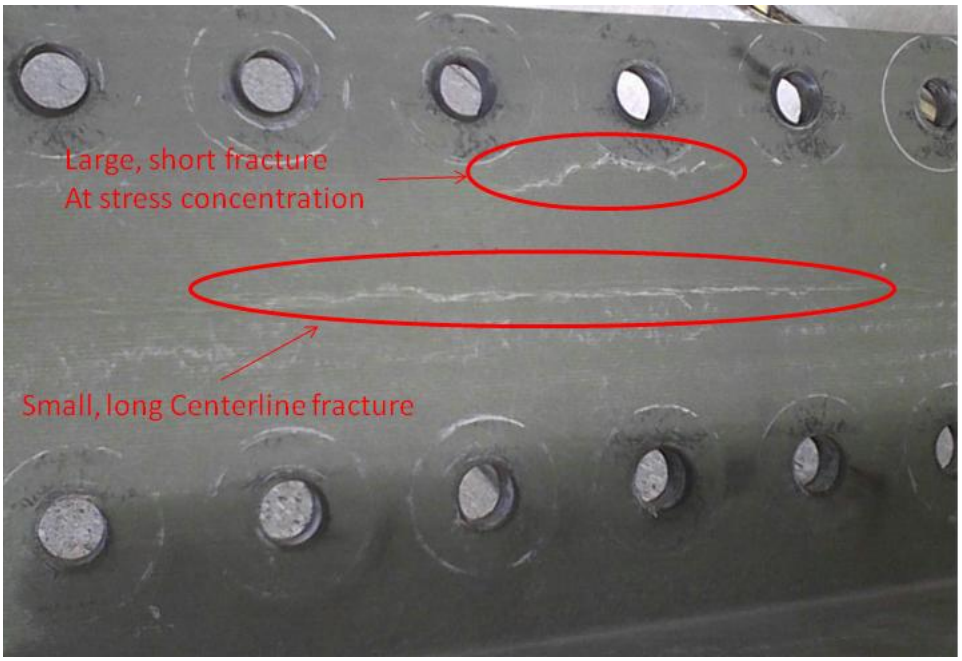

Figure 41 - Barrel structure point of failure

In order to confirm this potential root cause, the previous tests had to be reexamined to ascertain why they did not cause the failure. To further investigate this, an FEA model based in SolidWorks was built for the barrel structure at several different loading conditions, all which simulate the real-time railgun pulse of a maximum peak force reached at about 100us, and a current falloff pulled directly from testing data that lasts until just over 1ms. In this way the structure's reaction to this dynamic loading situation was analyzed, with the results shown in Table 7.

Table 7 - FEA Results for McMaster FRP Structure

Peak Current	Peak Force per meter	Factor of Safety
60 kA	174 kN	1.2
90 kA	391 kN	0.55
120 kA	694 kN	0.23
120 kA with Internal Arcing	900 kN	0.21

Since every test had been conducted at 5kV or lower voltages, peak currents exceeding 60kA had not been seen. When the barrel arced at 5kV across rails 1-4 with a peak current of 120kA, the fiberglass was pushed beyond its limits and fractured. The factors of safety shown in Table 7 are representative of the minimum material ratings, and larger factors of safety could have been the actual reality. The fracture of the structure is in good agreement with this simulation data, though the simulation assumes a linear elastic isotropic material.

3.6.3.2 Possible structure solutions

The augmentation scheme of this gun allows for very large, and efficient, projectile accelerations but comes at a cost. The forces between the opposing rail sides are larger than that of its non-augmented counterparts. In order to overcome these forces with a plain rectangular cross-section, the thickness of the FRP material would need to approach or exceed three inches. Therefore, an attempt to increase the bending moment of inertia of the clamps was made in simulation. The simulations covered an I-Beam variation and a T-Beam variation. Each beam has outer dimensions of 6 by 6 inches, and a web thickness of 3/8 of an inch. These cross-sections allow for a drastic increase in the moment of inertia, while retaining the same thickness. This allows for the same Grade-9 bolts to be utilized, saving money.

The maximum stresses in the I-Beam, when simulated with the maximum 120kA load during arc failure, showed large deflections in the top portion of the beam, and stresses exceeding the 68MPa minimum possible yield stress in the material. The results of this simulation are shown in Figure 42.

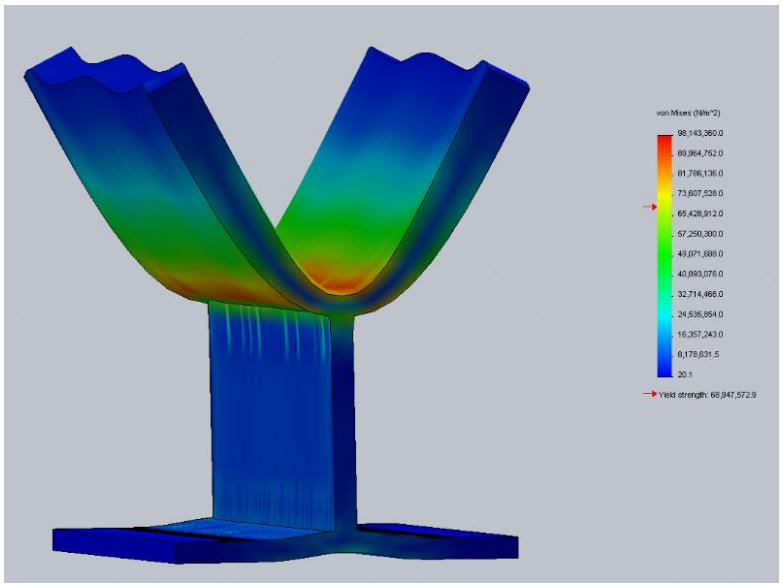

Figure 42 - Maximum I Beam Stress

The T-Beam had much better results, in fact far better than expected, as shown in Figure 43. With the same loading profile as the I-Beam, the T-Beam reduced the stresses seen in the structure drastically, and ended up with a factor of safety greater than 400.

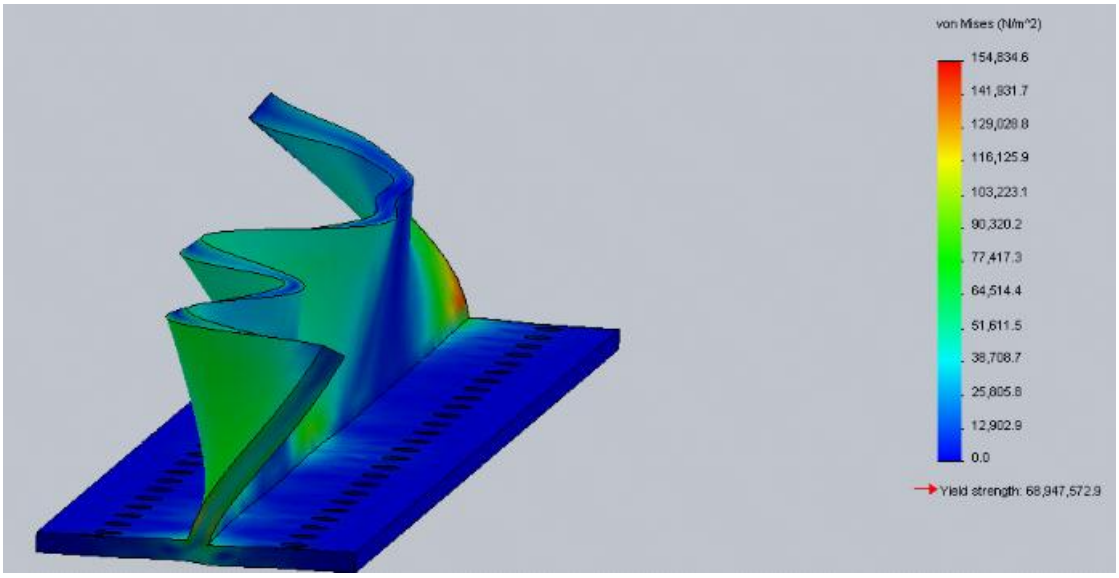

Figure 43 - Maximum T Beam Stress

Even though the T-Beam deflects in a very odd manner at the top of the cross-section, the maximum point of deflection is less than .0003", with the maximum deflection in the area contacting the rails being less than .00002". Here the maximum stress in the structure is 154kPa, far less than the maximum allowable stress of 68MPa.

While these simulations show promise, they are merely initial simulation results. A more in depth analysis into the validity of these simulations must still be done to verify that a T-section beam will in fact withstand the large forces generated within the Mk. 2 barrel during a full voltage test. Furthermore, these simulations do not take into account composite theory, even though FRP is a composite material. These only assume a linear elastic isotropic material, similar to a metal.

4 Conclusion

In summary, lessons were learned through the failed testing of the Mk. 1.1 system that showed flaws in the data acquisition system and control systems, as well as proved the difficulties of press fit projectiles in small bore railguns. These lessons were incorporated into the Mk. 2 railgun and projectile assembly design, giving effective and reliable data acquisition, as well as leading to the 3 part projectile design.

A model was developed in Matlab to predict the performance of the Mk. 2 railgun system, including the barrel current, projectile assembly velocity and position, barrel magnetic field, and thermal changes in the projectile. The model equations are derived and integrated over time using Matlab's ODE45 function. The results of this model show velocities exceeding 3 km/s and efficiencies of about 24%, which is a large increase compared to the Mk. 1 efficiency of 0.6%.

Static and pulse dummy load testing of the Mk. 2 barrel showed good correlation with the model predictions. The resistance and inductance of the barrel over various frequencies are close to the modeled values, but begin to taper away from the model at lower frequencies due to the structural wings of the actual rails, which were not modeled. This proves that the barrel does act as predicted, and generates magnetic fields very similar to what the model states. Therefore the forces on the projectile, and the projectile velocity should be similar to the model predictions when full projectile testing is successful, thereby exceeding the design goals and delivering a system capable of generating impacts to simulate orbital debris impacts in the GEO range.

The initial projectile testing of the Mk. 2 system showed projectile failures during initial acceleration. These failures were caused by non-ideal rotations of the sabots, causing rail gouging and severe increases in static friction forces and contact resistances. This, in turn, sheared the screw holding the sabots to the main projectile, ending projectile conduction and firing the projectile out of the barrel at speeds less than 270 m/s. Several different configurations were

tested, including changing from a nylon to a steel screw, adding a projectile attachment to mitigate sabot rotation, and adding rail surface additives such as graphite and silver paste to reduce friction during initial acceleration.

During the final test conducted there was an internal arc spanning from rail 1 to rail 4, causing an increase in current from the expected 60kA to a peak of 120kA. This increased current, coupled with the plasma pressure generated within the barrel assembly, fractured the outer structure of the barrel. An analysis of the failure showed that the clamp material was not as strong as previously thought. Further research into possible solutions to the failure show a T-section made of similar material would be suitable for future research.

5 Future Work

First and foremost, the barrel structure needs to be rebuilt to within stand the forces created by the augmented gun. The results showed favor of the T-section beam, which would allow for the replacement of only the fiberglass structure at relatively low cost. After further analysis of the validity of the T-section's ability to withstand the barrel forces has been completed, the acquisition or fabrication of the T-Beam could be done, and integrated onto the gun for further testing.

The insulation between augmenting rails within the gun showed sporadic failure during testing. This can be improved by adding additional layers of Kapton and/or Mylar film to strengthen the insulation, and prevent arc failures in the future. Careful consideration should be taken to the growing thickness of this layer and it’s affect on the required lengths of the Augmenting Bars, shown in Appendix Section 7.5. If these layers get too thick for easy assembly, or there is too much bending in the rails, then new Augmenting Bars should be made to account for this increase in thickness.

Once the structure and insulation is rebuilt, a solid projectile test should be completed to get the system firing at high velocities for impact testing, as the solid projectiles are a proven and tested railgun projectile technology. While the 3-part projectile shows the potential of a controlled interface between the rails and projectile, the projectile has failed during initial testing. A projectile similar to the projectile used by Army Research Lab funding at a Virginia university [7], modified to fit in the 0.7 by .277 inch barrel would show promise and be of similar weight to their 3-part projectile counterparts. An example projectile of this design is shown in Appendix Section 7.6.

Testing should continue on the 3-part projectile. Though the aluminum attachment failed initially, an insulated attachment with graphite lubrication could be a possible solution. The screw size

within the projectile could be made larger, so that it and the threads could possibly withstand the forces during the initial acceleration. Furthermore, different materials for the sabots could be analyzed and tested; for example, copper, silver, or graphite. A more in-depth analysis of the forces on the projectile, sabots, and set screw during initial acceleration should be done, and could point a finger at why these failures are occurring.

Another, though more novel, solution to the failures of the 3 part projectile would be to provide the projectile assembly with an initial velocity, for instance from an air injection modification to the Mk. 2. This would require a major modification to the barrel, but could increase efficiency and final velocity. It would also require precise timing of the ST-300A switch, but should be relatively simple to implement with the Arduino already used to program the timing of the firing sequence and the break screens.

After additional, and successful, testing is completed on either the 3 part projectiles or the solid projectiles the model described in this thesis should be verified, and modified to match experimental results. A functioning model that can accurately predict the final velocity of test firings is a very useful tool for future research.

A useful tool for the continual research into the efficiency and effectiveness of different gun barrel topologies could be smaller railguns, with smaller power supplies. The Mk. 2 system worked well, but the capacitor bank, switching, and railgun barrel are prone to damage and are expensive to replace. To keep costs down while testing many different barrel and capacitor bank/switching configurations it could be useful in the future to scale down both the barrel and the capacitor bank, allowing for more accessible research.

The thermal model presented does not take into account the thermal expansion of the projectile or sabot material as it was heated by ohmic and frictional heating. This could have played a part in the failure of the projectile, and should be researched in the future.

6 Works Cited

[1] National Aeronautics and Space Administration, *The Threat of Orbital Debris and Protecting NASA Space Assets from Satellite Collisions,* 2009.

[2] M. R. Lockwood, “Design and Construction of an Expandable Series Trans-Augmented Electromagnetic Railgun,” Naval Postgraduate School, Monterey, CA, 1999.

[3] I. V. Hogg, The Guns: 1939/45, Macdonald, 1969.

[4] J. Maniglia, G. Zohar, J. Smiroldo and A. Westfall, "Design, Fabication, and Testing of an Electromagnetic Railgun for the Repeated Testing and Simulation of Orbital Debris Impacts," California Polytechnic State University, San Luis Obispo, CA, 2011.

[5] R. M. Ness, “Rayleigh line PFN,” find March 2011. [Online]. Available: http://www.nessengr.com/techdata/pfn/pfn.html#Rayleigh. [Accessed find find find].

[6] B. Maier, Selected Topics In Railgun Technology, Monterey, CA: Naval Postgraduate School, 2009.

[7] S. Barker, B. Roberts, S. Driskill, B. Schavitz, A. Mehr and P. Lanigan, “A Power Supply Oriented Small-Caliber EML Design Methodology,” Aberdeen Proving Ground, Maryland, 2005.

[8] T. Hands, D. Marshal, I. Griffiths and G. Douglas, “A2_6 Computation railgun dynamics & back EMF,” *Journal of Physics Special Topics,* December 2011.

[9] J. Nearing and M. A. Huerta, “Skin and Heating Effects of Railgun Current,” *IEEETransactions on Magnetics,* vol. 25, no. 1, pp. 381-386, January 1989.

[10] J. M. Gere and S. P. Timoshenko, Mechanics of Materials, PWS Publishing Company, 1997.

[11] May 2013. [Online]. Available: http://matweb.com/search/DataSheet.aspx?MatGUID=462fd1da8ad245b2ad40093889016448&ckck=1.

[12] May 2013. [Online]. Available: http://www.mcmaster.com/#8549kac/=mr2is7.

[13] A. S. Feliciano, "The Design And Optimization Of A Power Supply For A One-meter Electromagnetic Railgun," Naval Postgraduate School, Monterey, CA, 2001.

[14] ABB Switzerland Ltd Semiconductors, August 2011. [Online]. Available: http://www05.abb.com/global/scot/scot256.nsf/veritydisplay/3415d18ecb157ce0c1256f3c0041e51c/$file/5sdd%2050n5500_5sya1169-00aug%2011.pdf.

7 Appendix

7.1 Mk. 2 Capacitor Bank Schematics

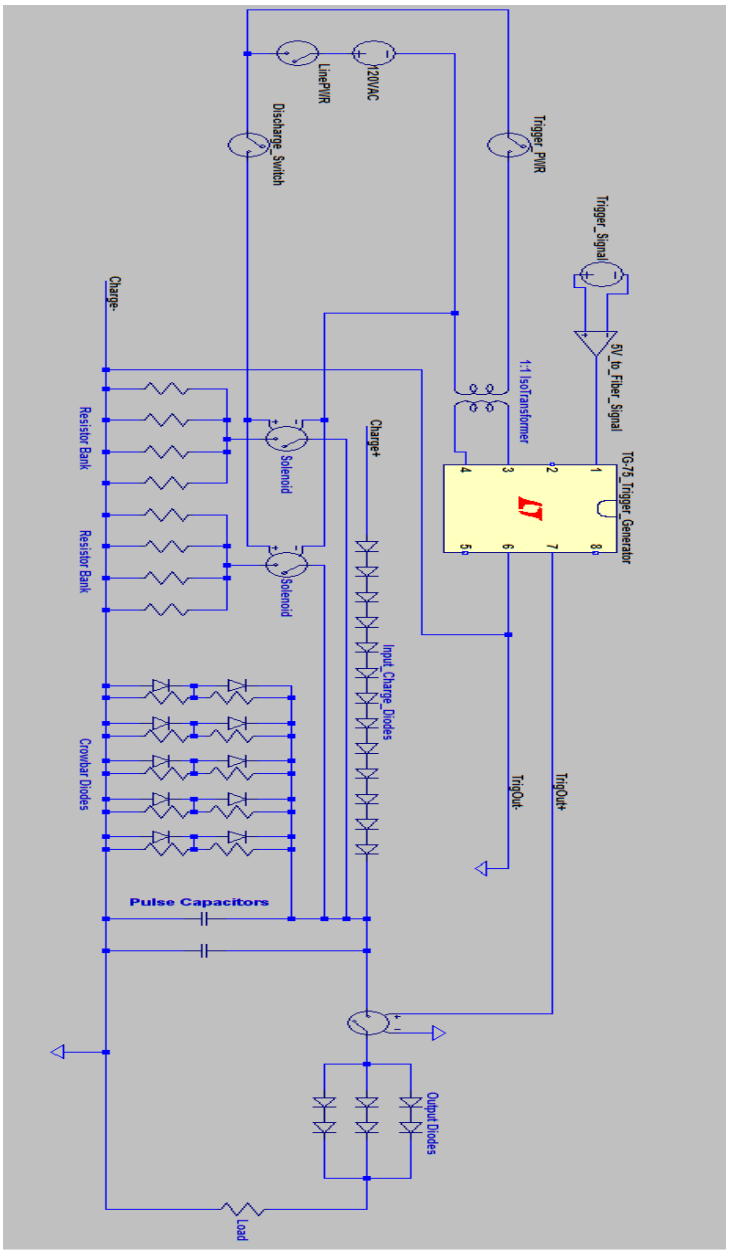

Figure 44 - Mk. 2 Capacitor Bank Schematic

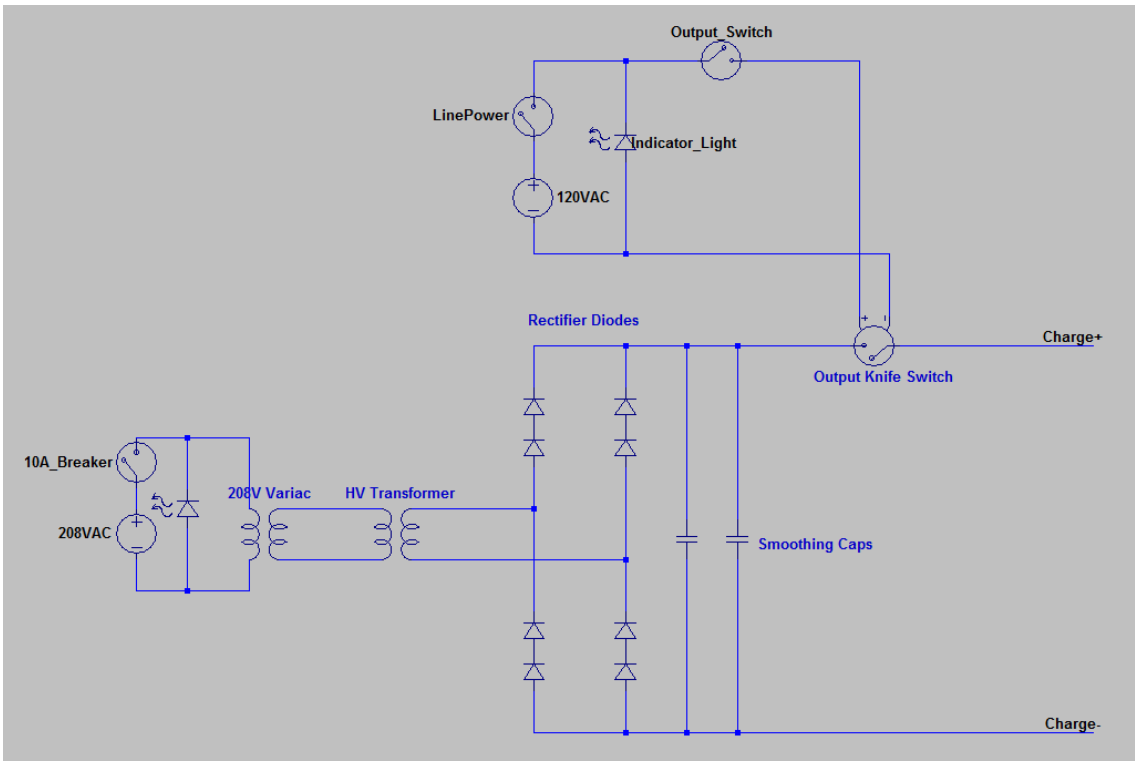

Figure 45 - Mk. 2 10kV Power Supply Schematic

7.2 Mk. 2 Testing Procedures

Mk. 2 Capacitor Bank Operational Procedure

Before the following setup and execution of test, be sure that all hardware is assembled and to set up any data acquisition equipment required. In the event of off-nominal behavior, skip to the Discharging Capacitors section and complete all the steps through Post-Testing before rectifying the problem. If there is no off-nominal activity, proceed through each of the sections in order. When a step or steps need to be initialized that will be done on the post-testing documentation.

Pre-Setup Checklist

1. Clear test cell of non-required personnel, any flammable materials, and put up Danger/Caution tape around exposed output conductors.
2. Ensure that load is securely connected to capacitor bank output.
3. Ensure HV cables are disconnected
4. Ensure power cable to capacitor bank is disconnected
5. Ensure earth ground connection to capacitor bank is disconnected

Initial setup and test of Resistor Bank

1. Ensure that all switches are in the ‘off’ position, and that the Charge/Discharge switch is in the ‘Discharge’ position
2. Plug in power cable between the capacitor bank and the test cell Molex connector
3. Plug in power cable between the Control rack and the Control Room Molex connector
4. Plug Control rack power strip into wall and turn on the power strip via the switch on the power strip
5. Test the operation of the resistor fans by switching the ‘Line PWR’ switch to the ‘On’ position. This will turn the fans on, whether the resistors are connected to the bank or not.
6. Test the operation of the resistor solenoids by flipping the Charge/Discharge switch to the ‘Charge’ position. They should audibly click upward, disconnecting the capacitors from the resistor bank. Flipping the switch back down to the ‘Discharge’ position should audibly click the solenoids back down, connecting the capacitors to the resistor bank.
7. Turn off the Line PWR

Continued setup and Pressure System

1. If operating < 3000V (change with testing) skip this section as switch pressurization is non-required.
2. Ensure that all valves on the Control rack are closed
3. Connect PVC tube IN to the IN port on the cap bank, and on the OUT port on the Control rack
4. Connect PVC tube OUT to the OUT port on the cap bank, and on the VENT port on the Control rack
5. Connect the compressed air tank regulator to the IN port on the Control rack.
6. Open valve on compressed air tank, pressurizing the regulator

7. Open valve on regulator, pressurizing the Control rack IN valve. Ensure that the regulated pressure is near the desired switch pressure determined by switching operational voltage (Generate this curve), being careful to NEVER exceed 30psi.
8. Now open the valve that pressurizes the switch. Final pressure is determined by switch operational voltage. (Generate this curve)

Continued setup and HV Power Supply

1. Make sure that Variac on the HV Power Supply is turned to 0 volts
2. Ensure that there are no shorting cables across the smoothing capacitors, or any other obstructions within the supply
3. INITIALS REQUIRED: Noting the + and – cables and inserting them properly, plug HV cables into capacitor bank. Switching these cables will permanently damage the capacitors by reverse voltage.
4. Ensure fiber optic cable plugged into BNC to fiber box
5. INITIALS REQUIRED: Leave the room and ensure it is clear, no one should enter the room until testing has been completed
6. Plug in the 120VAC power for the HV Supply
7. Test the HV knife switch by powering on line voltage, and switch the ‘On’ switch on and off, visually assessing the movement of the knife switch
8. Ensure that the output switch is in the ‘off’ position
9. Plug in the 3 phase power for the HV supply
10. At this point, the capacitors are capable of charging once the breaker is set to the ‘on’ position

Stop and check data acquisition, camera, and any other equipment being utilized during the test to ensure that it is ready for test

Charging the Capacitors

1. First, on the Control Rack, turn Line Power 'On' and flip the Charge/Discharge switch to 'Charge'
2. On the HV Power Supply, switch line power to 'On' and switch the output switch to 'On'
3. To charge the capacitors, turn on the breaker and slowly ramp up the voltage using the Variac. If the breaker blows, turn the Variac back down to zero, and then flip the breaker back to the ‘on’ position. Then ramp the voltage up on the capacitors more slowly
4. Turn the Variac down to zero when the capacitors have reached their final charge voltage. The maximum voltage that the capacitors should ever see is 9000V. This voltage will be shown on both the power supply as well as on the capacitor bank.
5. When voltage has been confirmed:
    a. Switch the output switch to 'Off' on the HV Power Supply
    b. Flip off the breaker
    c. Turn off the HV Power Supply line power

Firing the Capacitors

1. On the Control Rack, flip the Trigger 1 Power switch to the 'On' position.
2. Wait about 20 seconds
3. On the Control Box flip the arm switch, arming the firing button
4. Countdown from 5, pressing the red fire button at end of countdown. The ST-300A switch will fire, releasing the energy stored in the capacitors into the load.

Post Testing: Vent Switch, Discharge Capacitors, and Safe the System

1. Flip the Control Rack charge/discharge switch to the 'Discharge' position.
2. On the HV Power Supply unplug both the 3 phase and the 120VAC
3. If system was previously pressurized continue to Step 4, if not skip to Step 9
4. On the Control Rack, use the vent switch to vent the air from the switch Flip the 'Vent' valve switch open. This allows the 15psi compressed air to go through the switch and back out, vented into the control room.
5. While the vent valve is open, turn off the supply to the regulator on the air tank
6. Turn the regulator down to zero pressure
7. Turn off the main valve to the switch
8. Turn off the Vent and Set Pressure valves
9. Before entering room:
    a. Put on Lineman HV gloves
    b. Confirm the charge voltage on the capacitor bank is ~ 0 volts (visually)
    c. Confirm the REF voltage meter is < 400V. If it is not, DO NOT ENTER ROOM
        i. Wait until REF voltage is < 400V
10. While in the room:
    a. Using the dump stick, short the capacitors to bring their voltage to 0. There may be some slight arcing during this operation, this is both SAFE and NORMAL and no damage to the capacitors will be done.
    b. Attach grounding cable to a 120VAC power plug in test cell to ground system for service and storage
    c. Disconnect HV cables from capacitor bank panel and place in 5 gal storage bucket
    d. MAKE SURE that BOTH voltage meters are reading 0 VOLTS
        i. If the REF voltage meter is reading a voltage >200V, tap the dump stick to the frame, that will force the negative terminal of the capacitors to earth GND. DO NO ATTEMPT AT HIGH VOLTAGE (>500 volts)
11. Exit room and remove HV gloves, the test cell is now safe
12. On the Control Rack, switch the Line Power switch to 'Off'. Unplug rack from the wall.
13. Unplug all cables running to the capacitor bank and store them properly
14. Disconnect load (railgun or otherwise) if applicable, or prepare for another test by starting from the top.
    a. If this is the final test, store the test equipment and put everything away. The systems are now in their storage states.

15. Storing the capacitors requires that the grounding strap is connected to earth ground in the test cell. This has already been completed in the above steps, but SHOULD NOT be disconnected for system storage.

Railgun Post Testing Datasheet

Main Operator: _____ Procedural/Safety Personnel: _____

Date: _____ Test #:_____ Charge Voltage: _____

Switch Pressure (gauge, Torr):_____

Procedural Initials:

HV Cable Polarity: Main: _____ Safety: _____

Room Cleared for Test: Main: _____ Safety: _____

Post Test Data:

File name for High Speed Video: _____

File name for Oscilloscope Data: _____

Break screen Results: _____ Measured Break screen Separation: _____

Velocity Measurement (Screens): _____ Velocity Measured (High Speed): _____

Channel information for Oscilloscope Data:

Channel A: _____ Multiplier: _____

Channel B: _____ Multiplier: _____

Channel C: _____ Multiplier: _____

Channel D: _____ Multiplier: _____

List any test anomalies here, for the capacitor bank and support systems:

List any test anomalies here, for the railgun barrel specifically (arcing, projectile issues, etc.)

7.2.1 Arduino (Microprocessor) Codes

```
int button = 7;
int state = 0;
unsigned int loop1 = 0;
void setup()
{
  Serial.begin(9600);
  pinMode(button, INPUT);
  pinMode(12, OUTPUT);
  pinMode(11, OUTPUT);
}
void loop()
{
  Serial.println("Cal Poly EMRG Mk.2 Fire Control (No Screens)...Waiting for button press...");
  PORTB = B000000;
  loop1 = 0;
  while(loop1 == 0)
  {
    if(digitalRead(button) == HIGH)
    {
      Serial.println("Button Pressed...");
      PORTB = B011000;
      loop1 = 1;
    }
  }
  Serial.println("Test Complete, Button pressed. Arduino resets in 10 seconds.");
  delay(1000);
  Serial.println("Resetting");
}
```

Figure 46 - Arduino Code for no break screen firing of capacitors

```
int button = 7;
int state = 0;
int SCR1 = 3;
int SCR2 = 8;
unsigned int EV1 = 0;
unsigned int EV2 = 0;
unsigned int count = 0;
unsigned int loop1 = 0;
unsigned int loop2 = 0;
unsigned int loop3 = 0;

void setup()
{
  Serial.begin(9600);
  pinMode(button, INPUT);
  pinMode(12, OUTPUT);
  pinMode(11, OUTPUT);
  pinMode(SCR1, INPUT);
  pinMode(SCR2, INPUT);
}

void loop()
{
  Serial.println("Cal Poly EMRG Mk.2 Fire Control...Waiting for button press...");
  PORTB = B000000;
  EV1 = 0;
  EV2 = 0;
  loop1 = 0;
  loop2 = 0;
  loop3 = 0;
  while(loop1 == 0)
  {
    if(digitalRead(button) == HIGH)
    {
      Serial.println("Button Pressed...");
      loop1 = 1;
      PORTB = B011000;
    }
  }
  while(loop2 == 0)
  {
    if(digitalRead(SCR1) == LOW)
    {
      EV1 = micros();
      loop2 = 1;
    }
  }
  while(loop3 == 0)
  {
    if(digitalRead(SCR2) == LOW)
    {
      EV2 = micros();
      loop3 = 1;
    }
  }
  count = EV2 - EV1;
  Serial.println("Breakscreens successful! Arduino resets in 10 seconds.");
  Serial.println("Breakscreen Clock Count = ");
  Serial.println(count);
  delay(1000);
  Serial.println("Resetting");
}
```

Figure 47 - Arduino Code for full firing with breakscreens

7.3 Mk. 1.1 Test Data

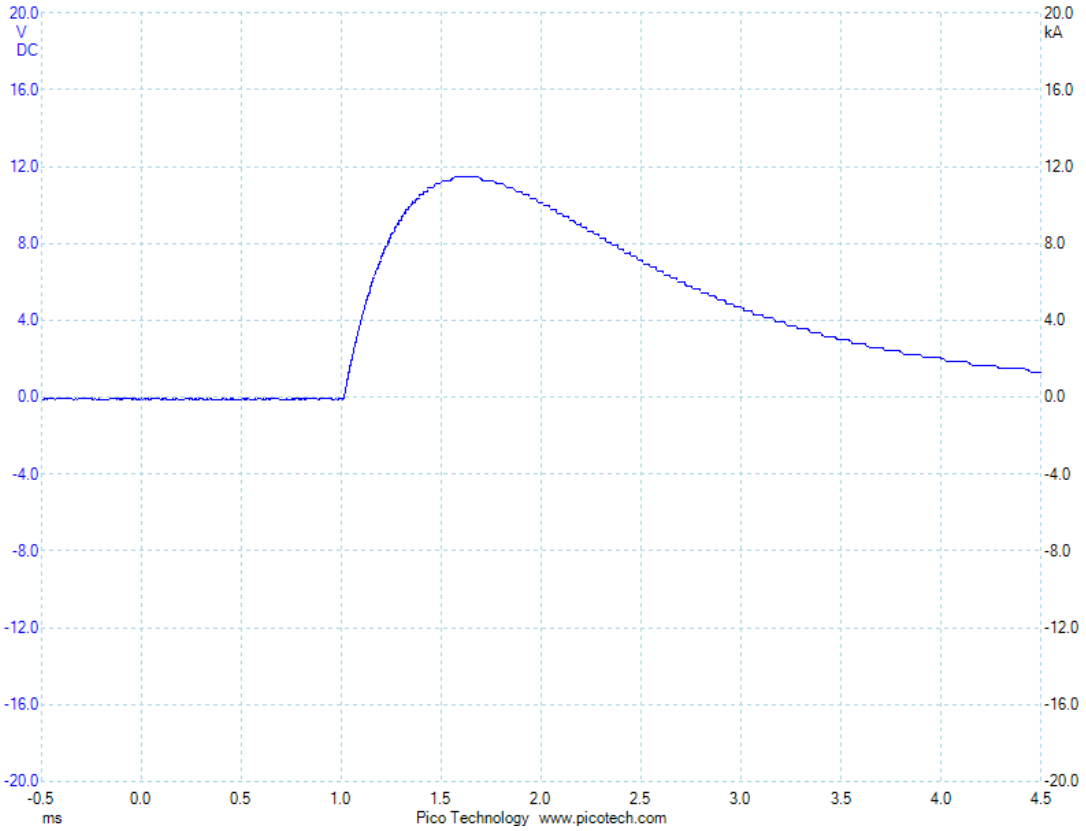

Figure 48 - Single Ignitron firing at 300V. Mk. 1.1 test

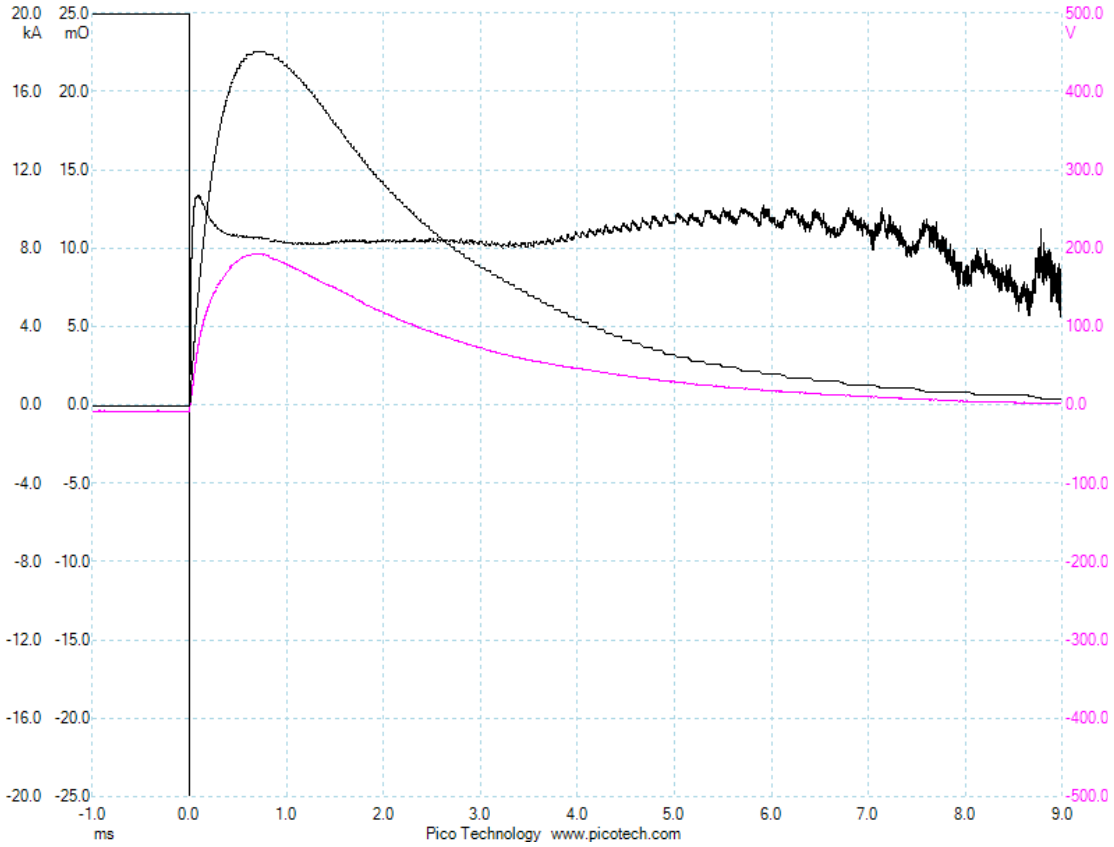

Figure 49 - Double Ignitron test at 360V Mk. 1.1

7.4 Mk. 2 Assembly

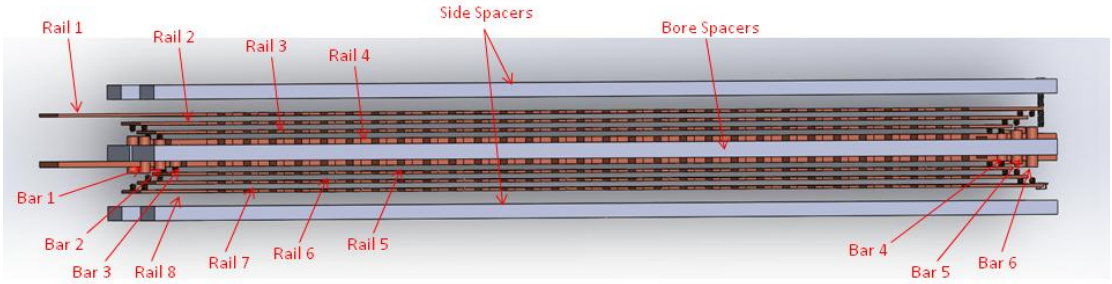

Figure 50 - Mk. 2 Internal Barrel Exploded

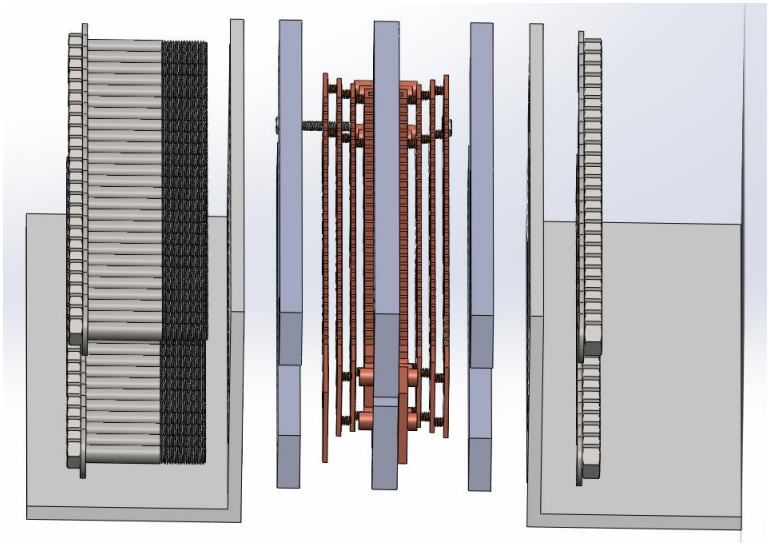

Figure 51 - Mk. 2 Entire Barrel Assembly Exploded

7.5 Mk. 2 Part Drawings

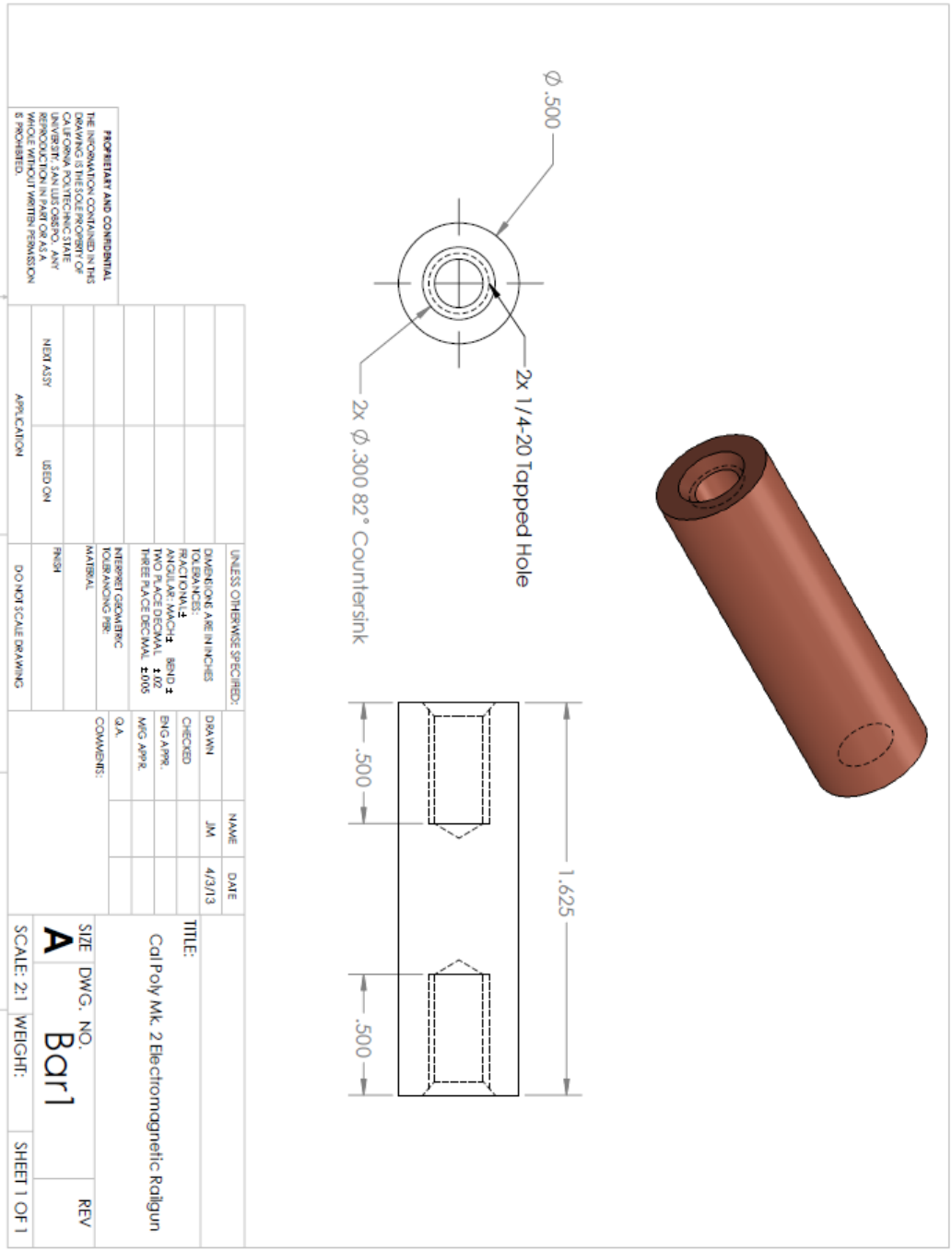

Figure 52 - Bar 1 Part Drawing

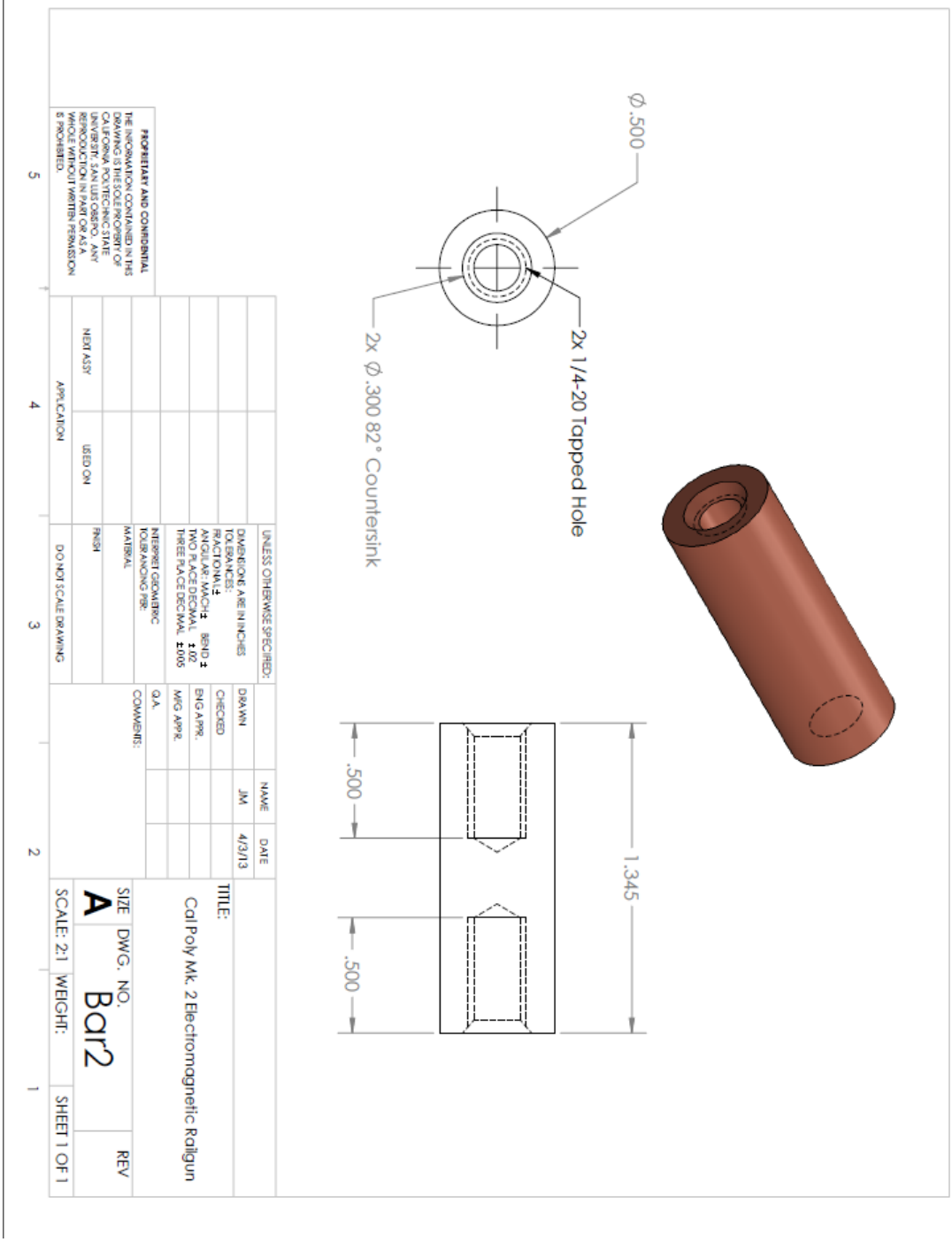

Figure 53 - Bar 2 Part Drawing

Figure 54 - Bar 3 Part Drawing

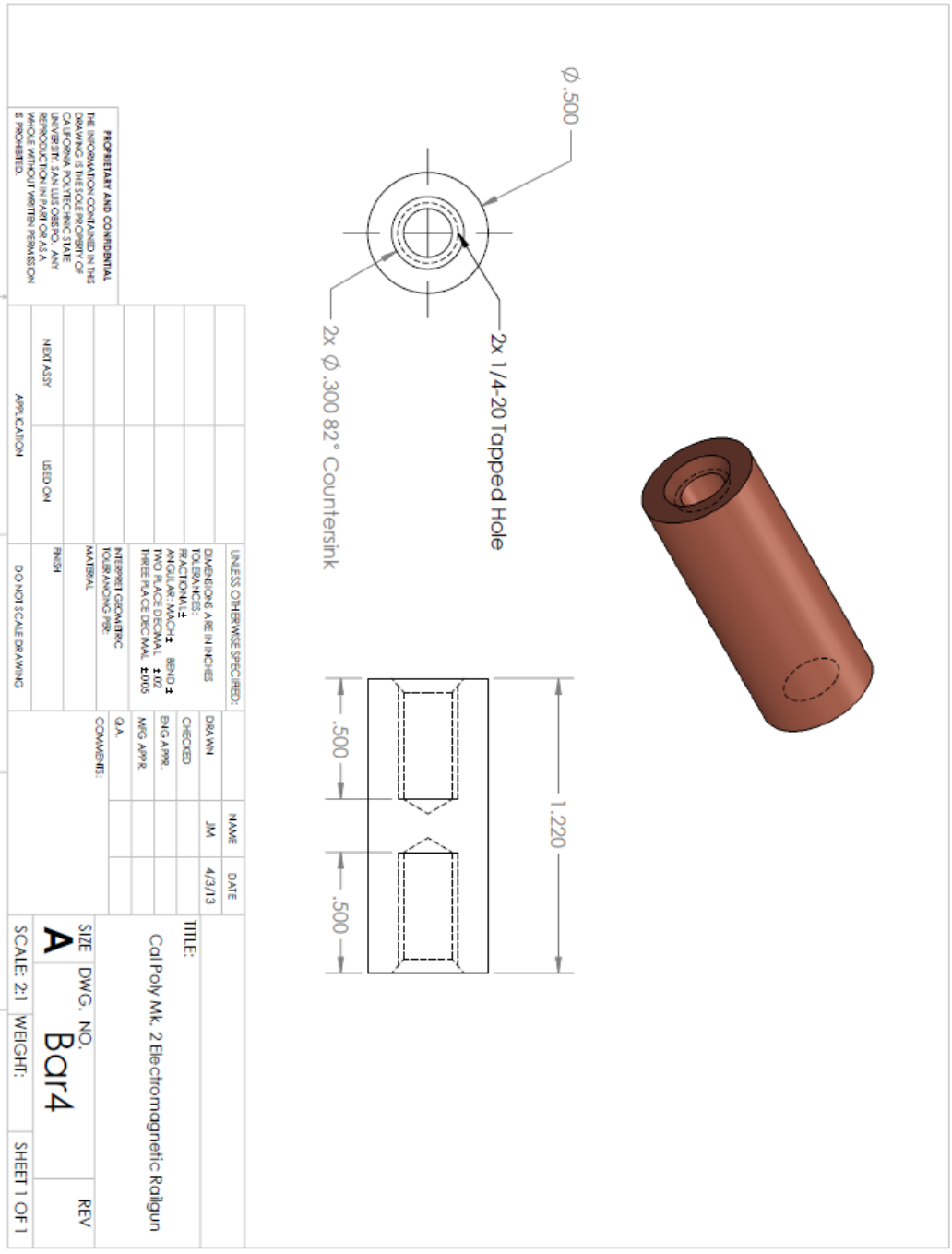

Figure 55 - Bar 4 Part Drawing

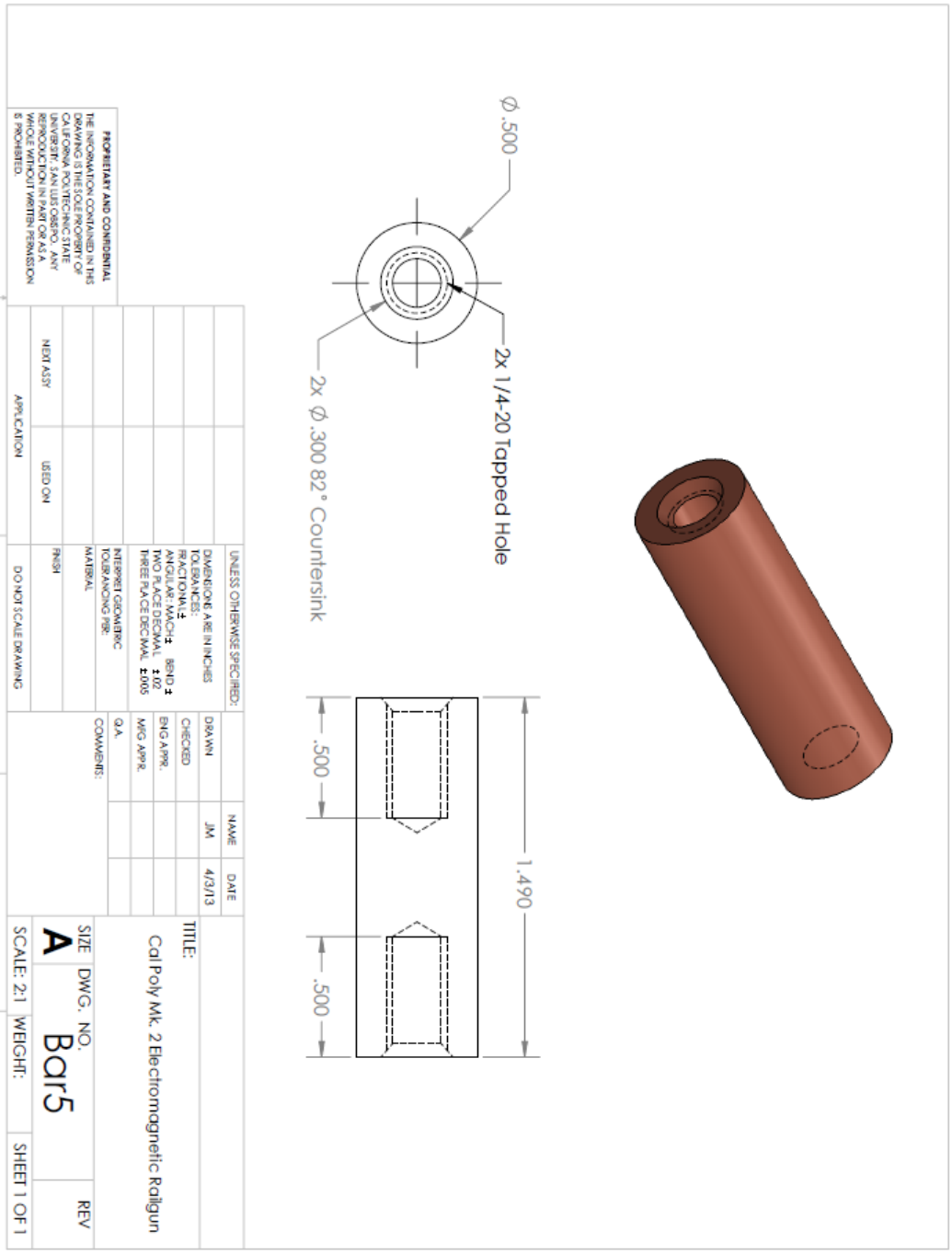

Figure 56 - Bar 5 Part Drawing

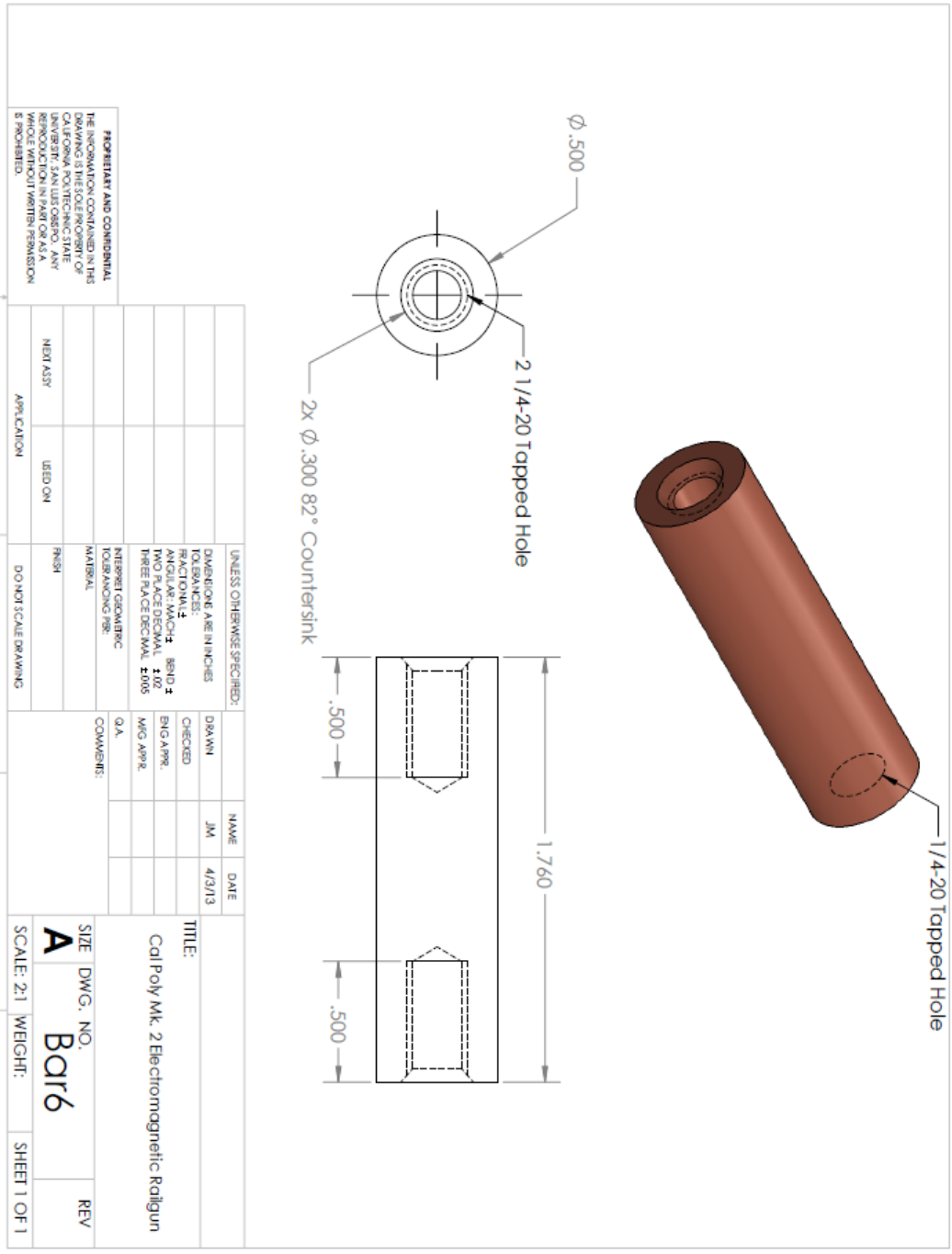

Figure 57 - Bar 6 Part Drawing

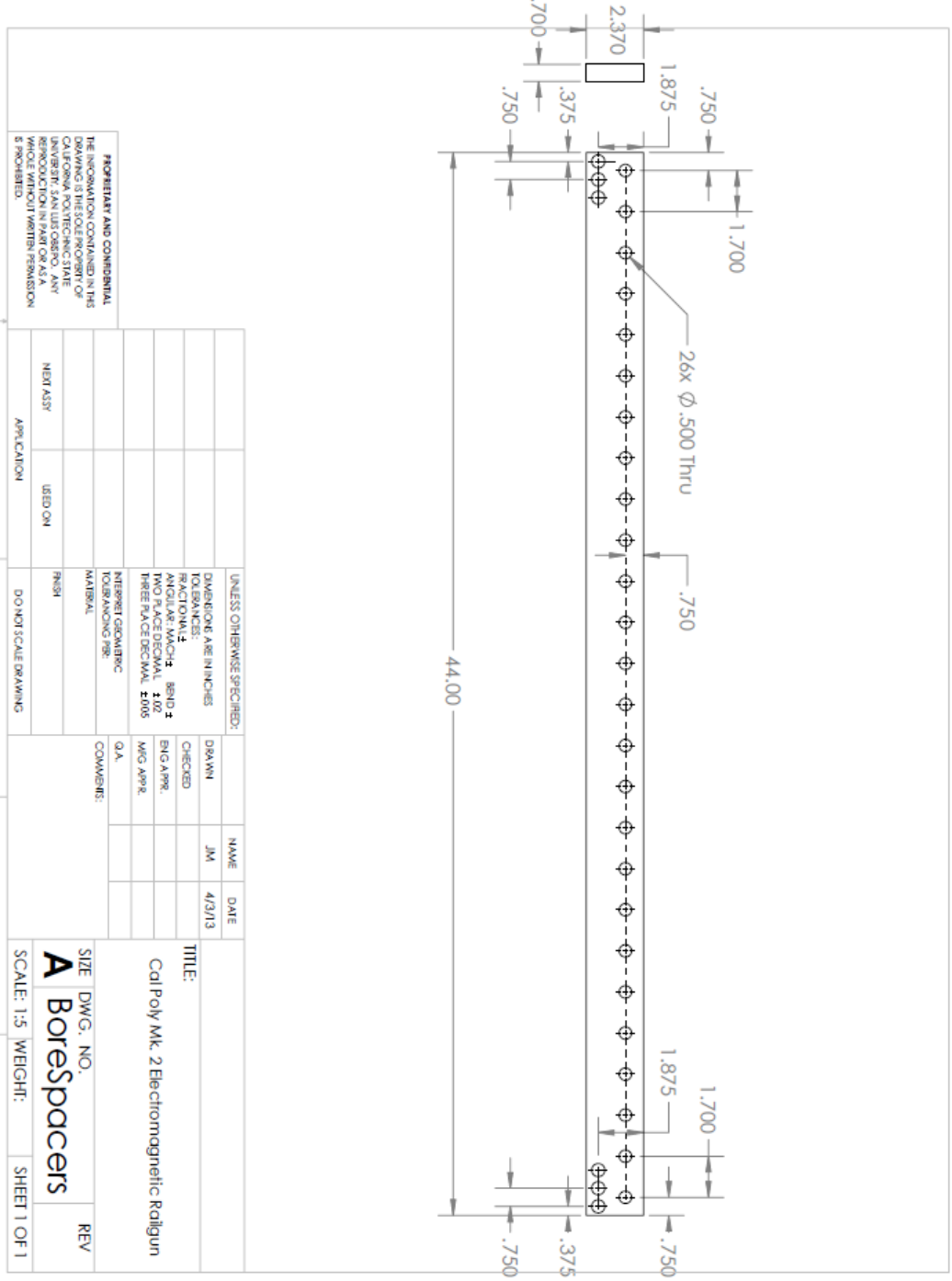

Figure 58 - Bore Spacers Part Drawing

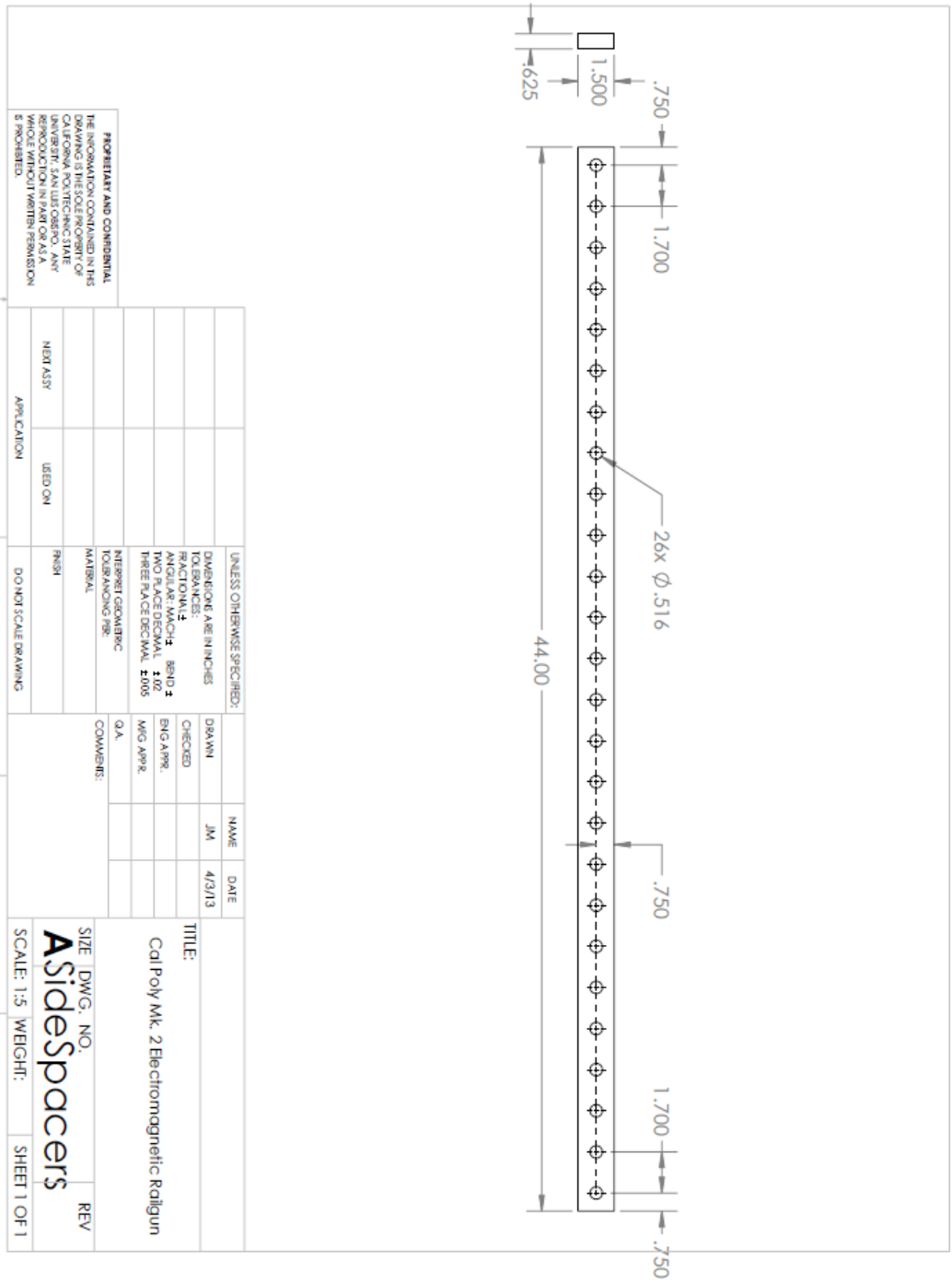

Figure 59 - Side Spacers Part Drawing

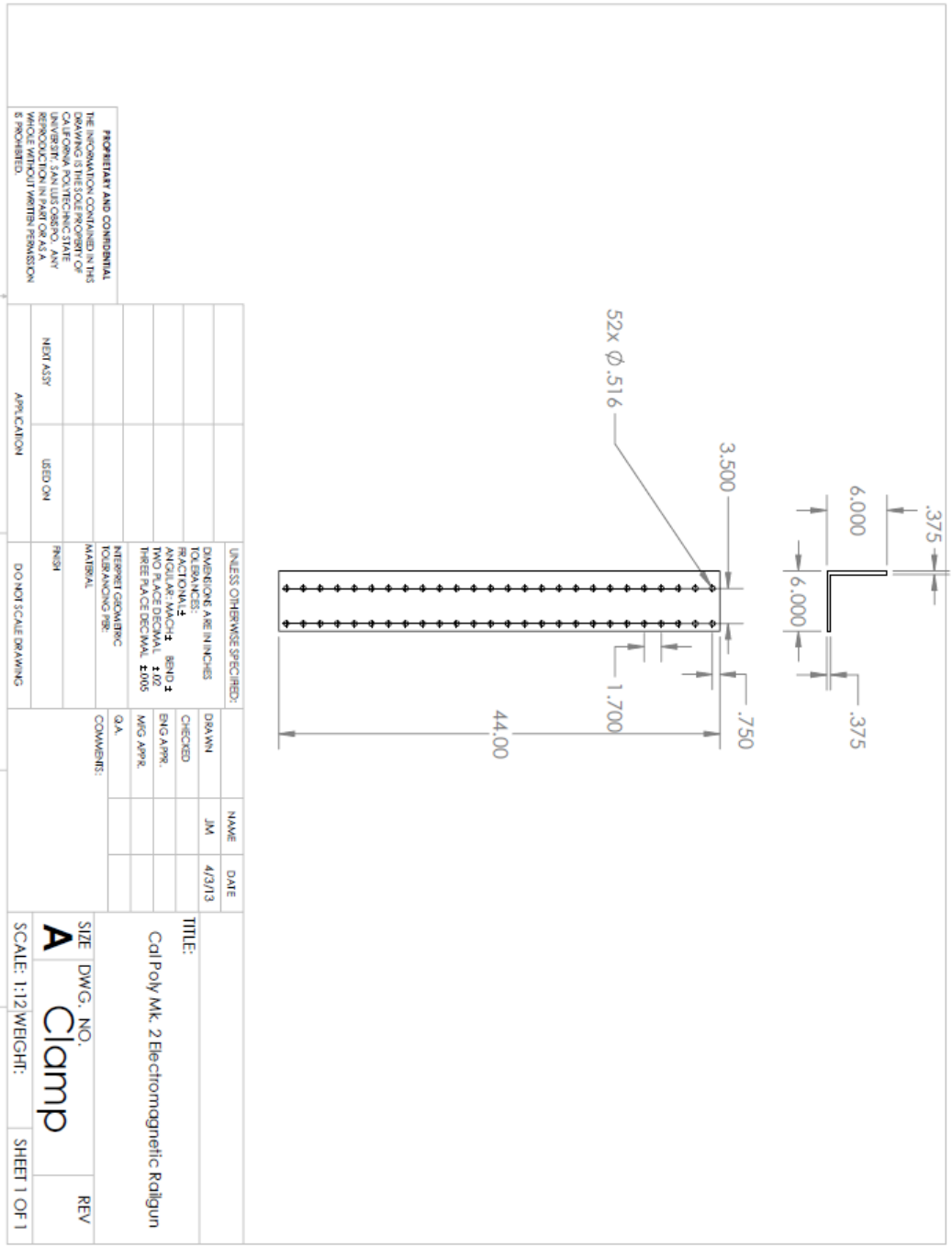

Figure 60 - Clamp Part Drawing

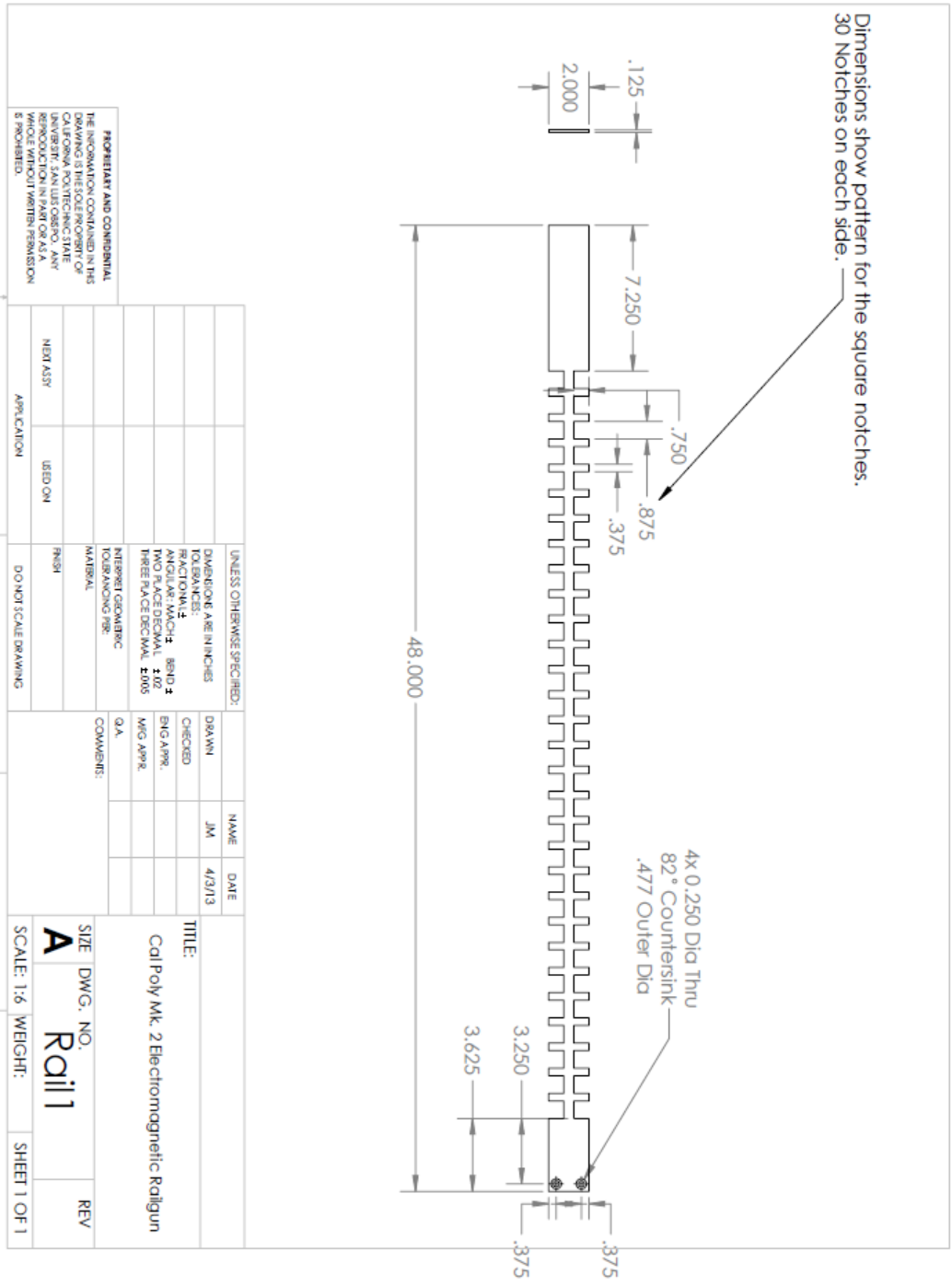

Figure 61 - Rail 1 Part Drawing

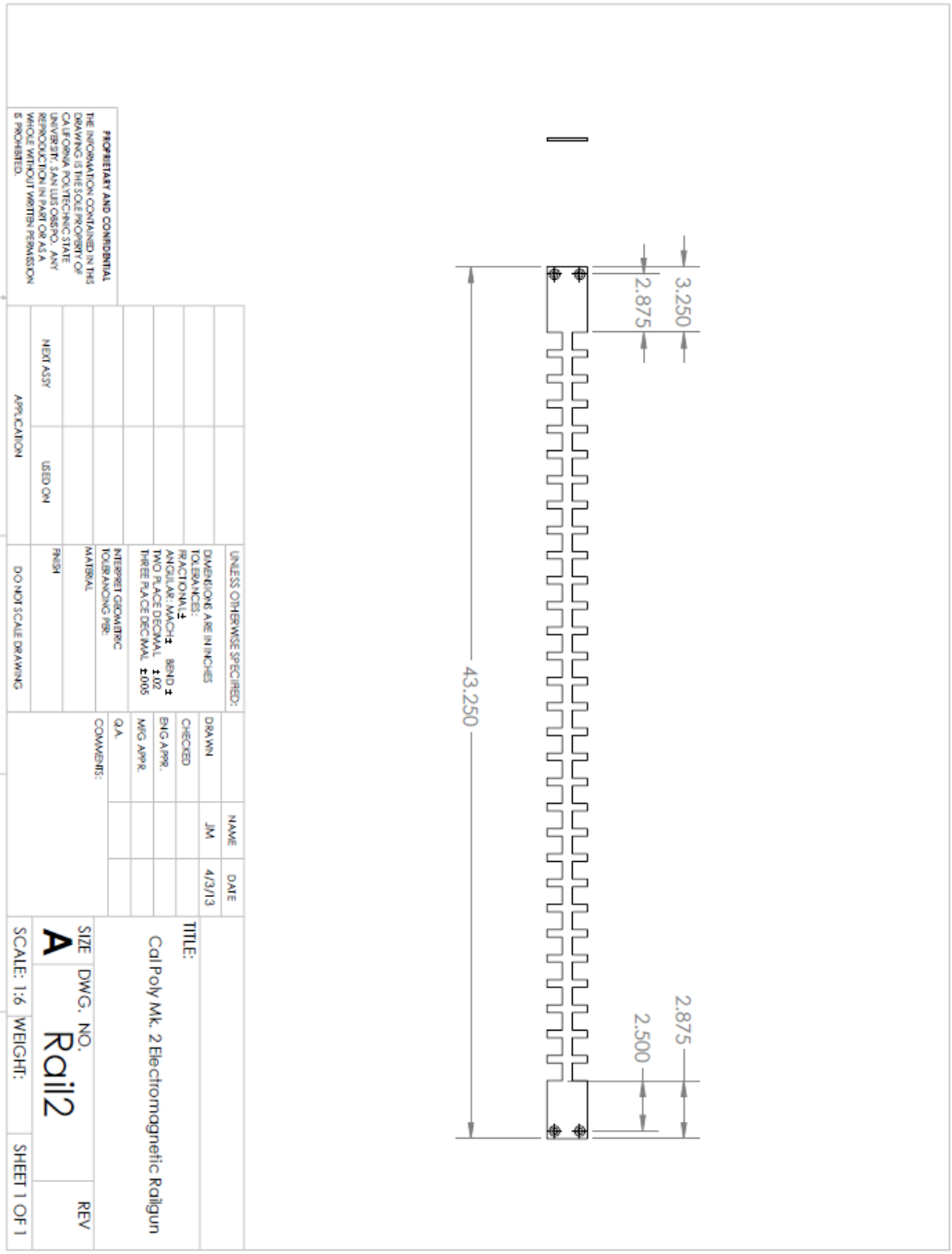

Figure 62 - Rail 2 Part Drawing

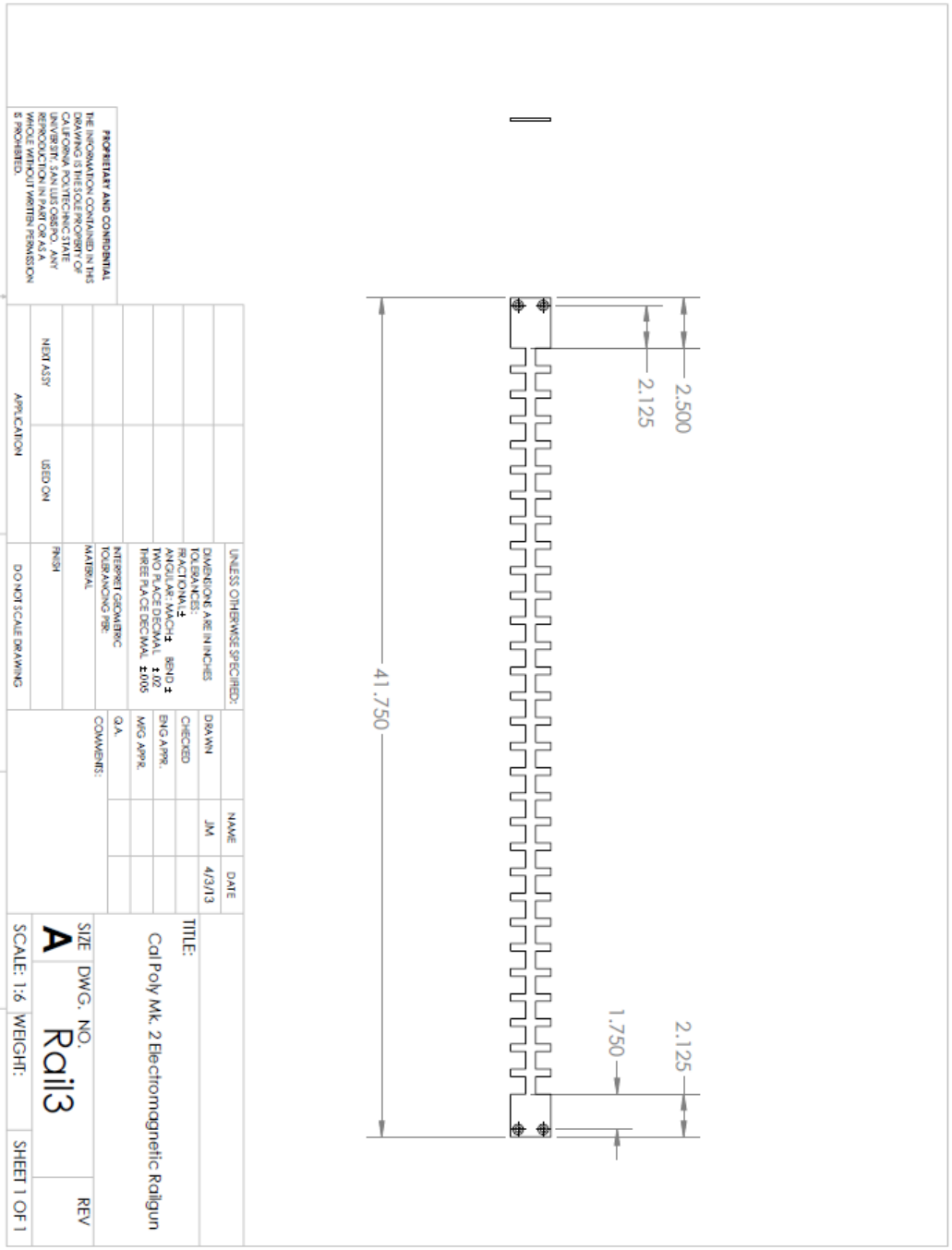

Figure 63 - Rail 3 Part Drawing

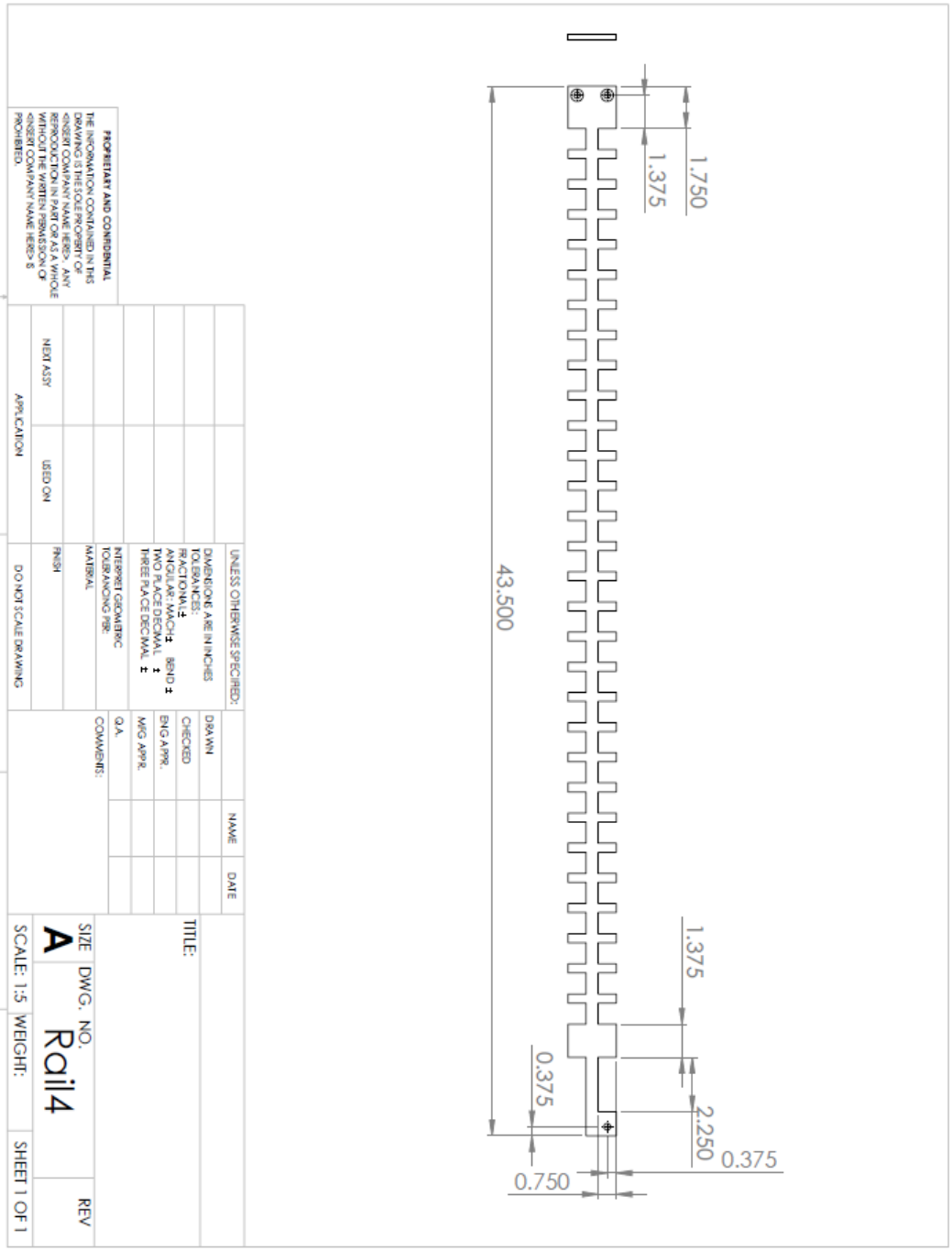

Figure 64 - Rail 4 Part Drawing

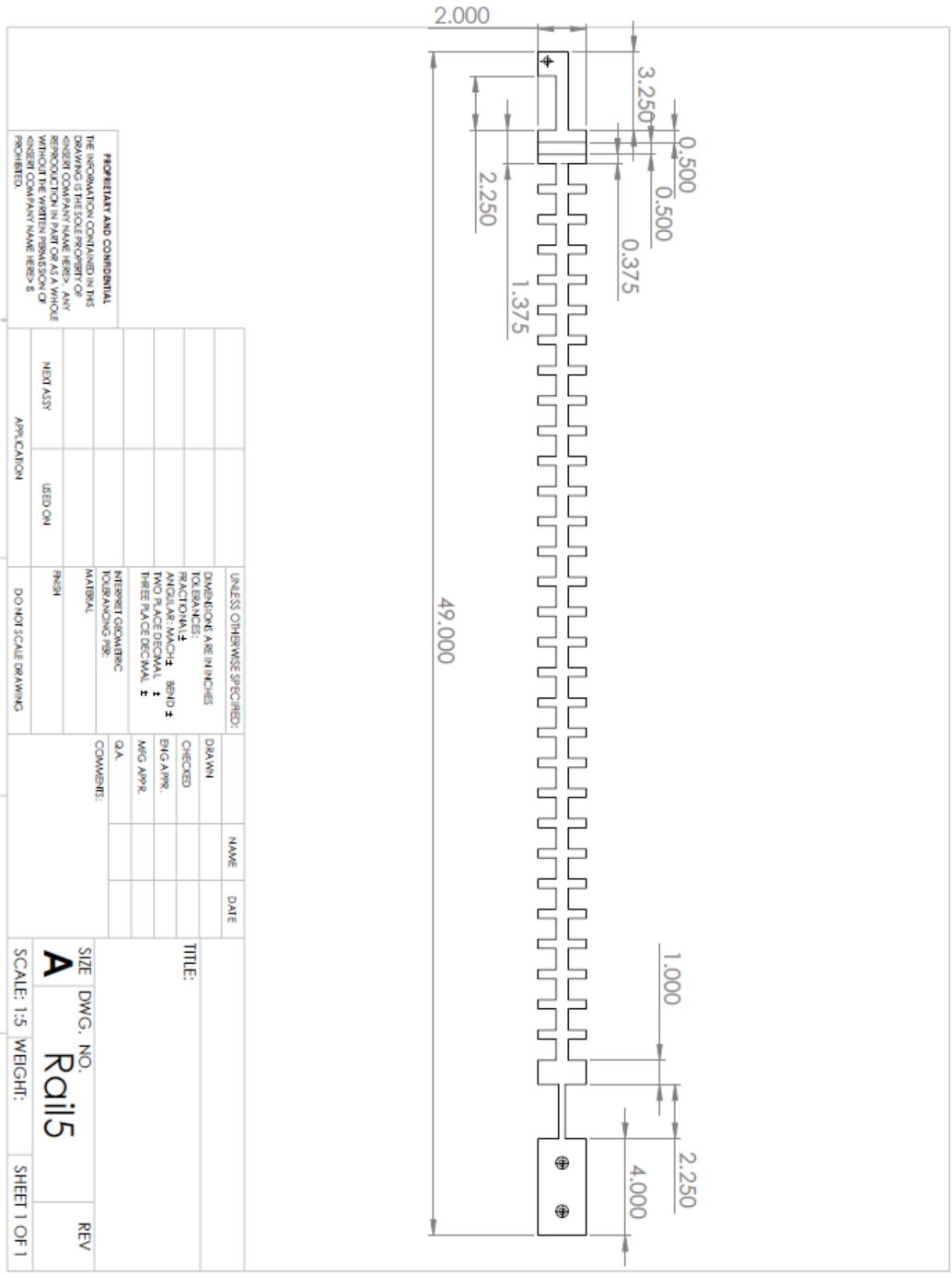

Figure 65 - Rail 5 Part Drawing

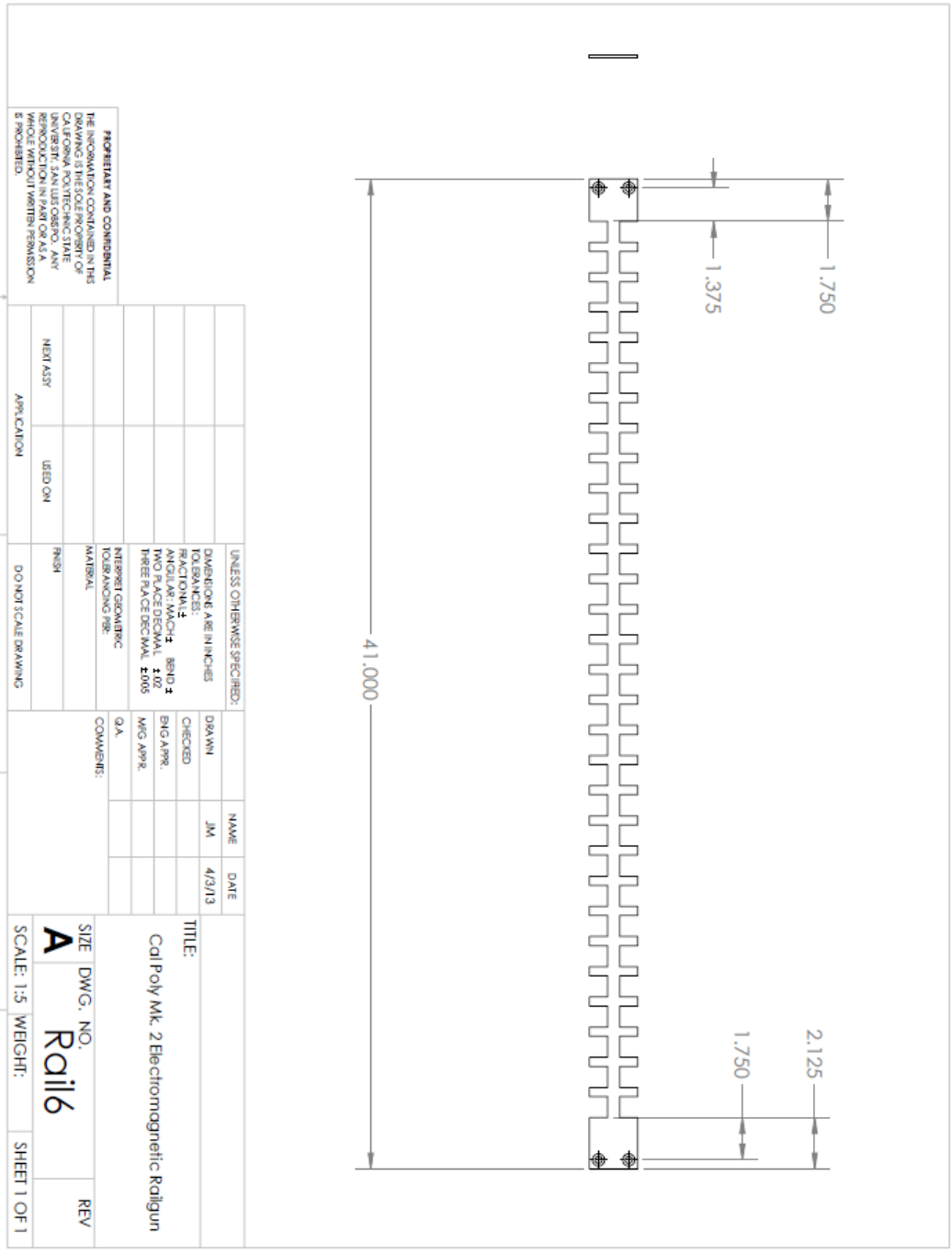

Figure 66 - Rail 6 Part Drawing

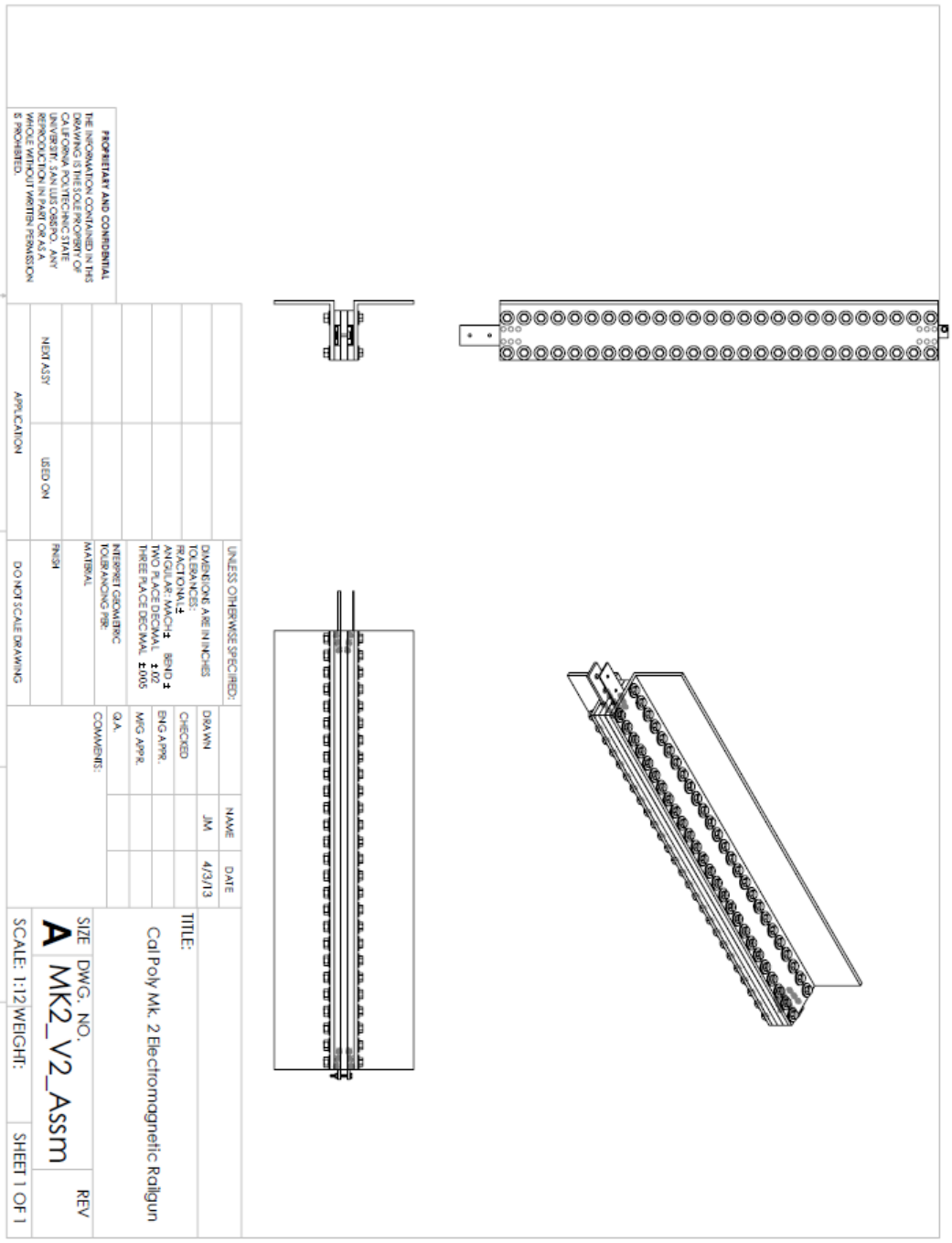

Figure 67 - Mk. 2 Full Assembly Drawing

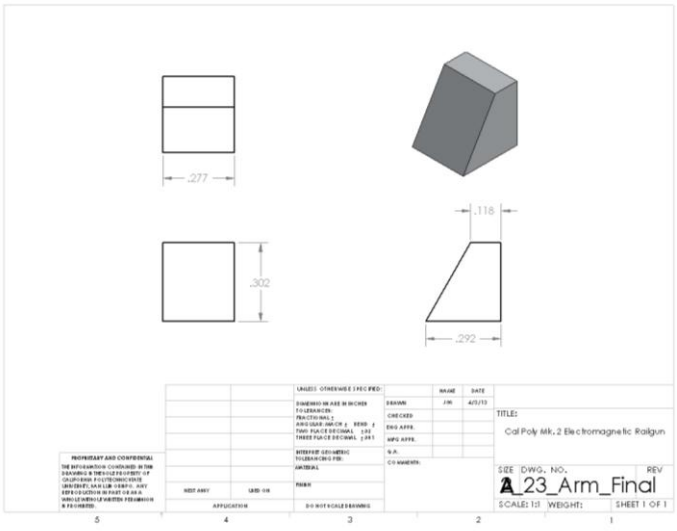

Figure 68 - Armature Part Drawing

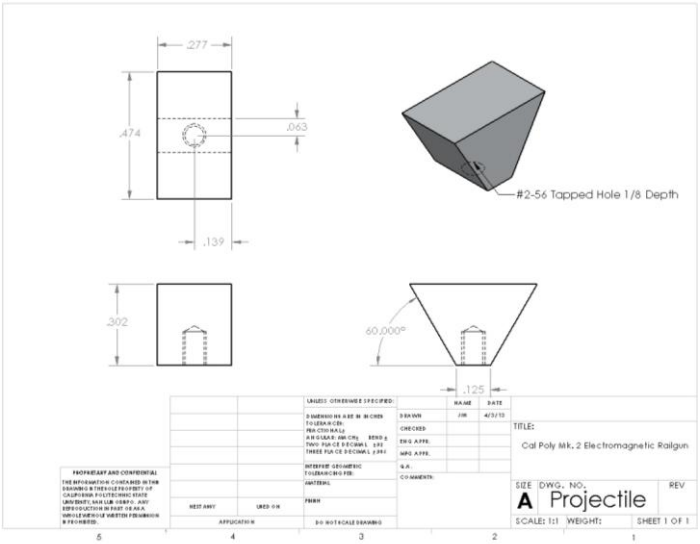

Figure 69 - Projectile Part Drawing

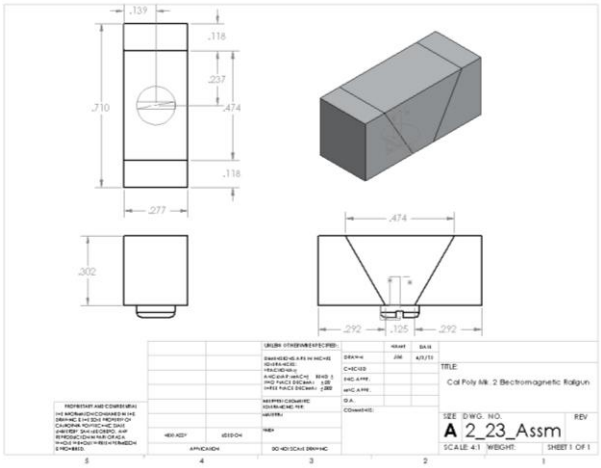

Figure 70 - Projectile Assembly No Attachment

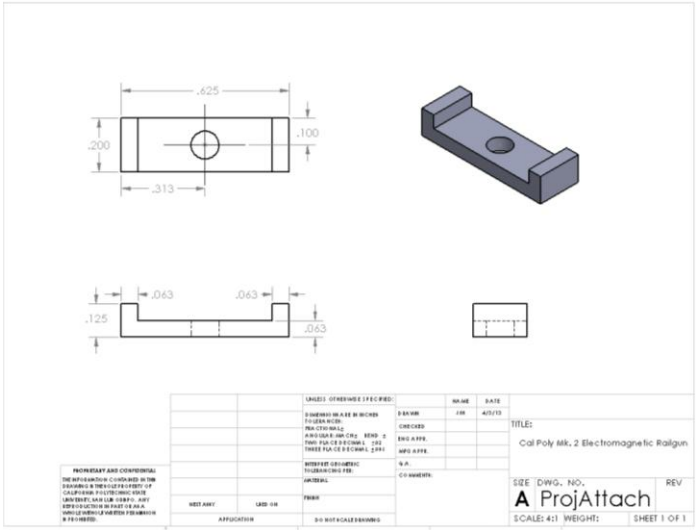

Figure 71 - Projectile Attachment Part Drawing

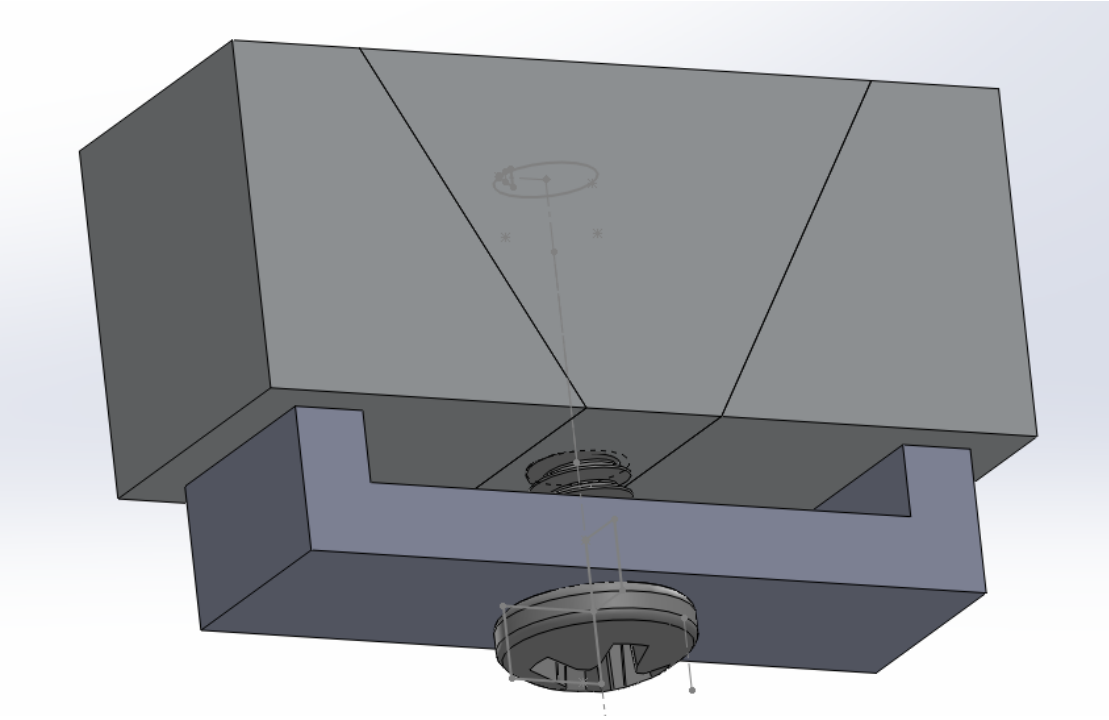

Figure 72 - Projectile with Attachment

7.6 Example Solid Projectile - Reduced Chevron

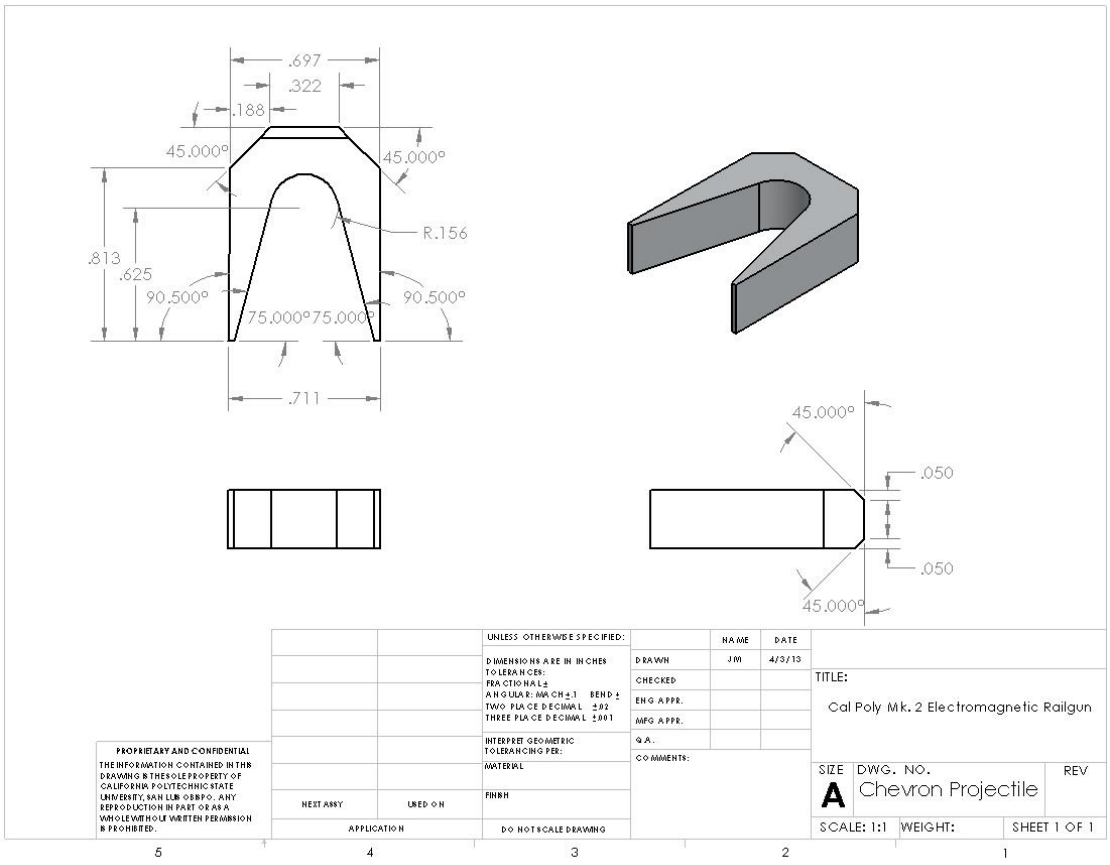

Figure 73 - Modified Chevron Projectile